

**Liquids and molecular solids investigated by
THz time-domain reflection and parallel-plate
waveguide spectroscopy**

Dissertation

zur Erlangung des akademischen Grades
Doctor rerum naturalium (Doktor der Naturwissenschaften)

vorgelegt von

Wenchao Qiao

Mathematisch-Naturwissenschaftliche Sektion
Fachbereich Physik

Contents

Chapter 1 Introduction	1
Chapter 2 Fundamentals of THz time-domain spectroscopy	6
2.1 THz time domain spectrometer	6
2.2 THz generation with femtosecond lasers	9
2.2.1 Photoconductive emitter	9
2.2.2 Photo-Dember emitter	13
2.3 THz Detection	18
2.3.1 Photoconductive detection.....	18
2.3.2 Electro-optic detection.....	19
2.3.3 Femtosecond lasers and conventional time delay setup	21
2.3.4 Asynchronous optical sampling technique	23
2.3.5 Setup of the ASOPS system	25
2.4 Theory of interaction between light and matter	27
Chapter 3 THz time domain reflection spectroscopy of aqueous systems....	31
3.1 General introduction.....	31
3.2 Setup for THz time domain reflection spectroscopy.....	34
3.3 Data analysis	36
3.3.1 Determination of the refractive index of silicon.....	38
3.3.2 Determination of the complex dielectric constant of liquid samples. ...	40
3.4 Properties of water	43
3.4.1 Water molecule reorientations.....	44
3.4.2 Modelling the dielectric function of water	46
3.5 Ions in water	49
3.5.1 Damped, driven harmonic oscillator model	50
3.5.2 Modelling the dielectric function of ionic solutions.....	53
3.6 Experimental results and analysis	54
3.6.1 Liquid water.....	55

3.6.2 Dielectric relaxation of HCl and NaCl water solutions.....	60
3.6.3 Other liquids measured by THz-TDS reflection spectroscopy.....	72
3.7 Conclusion.....	75
Chapter 4 THz time domain parallel-plate waveguide spectrometer	76
4.1 General introduction.....	76
4.2 Electromagnetic waves propagating in a parallel plate waveguide.....	78
4.2.1 TE modes.....	79
4.2.2 TM modes.....	81
4.3 Experimental setup.....	85
4.4 Temperature dependence of the PPWG THz spectrometer	87
4.5 1,2DCB absorption measured in the PPWG	92
4.6 Conclusion.....	95
Summary and Outlook	96
Zusammenfassung und Ausblick.....	98
References.....	101
List of publications.....	111
Acknowledgments	113

Chapter 1 Introduction

Terahertz (THz) radiation, which is also called T-rays or far-infrared or sub-millimeter wave radiation, lies between the infrared and microwave/millimeter regions of the electromagnetic spectrum (see Fig. 1.1.). The spectrum of THz pulses ranges typically from 10^{11} to 10^{13} Hz (0.1 THz to 10 THz). A photon with a frequency of 1 THz has an oscillation period of 1 ps ($1 \text{ ps} = 10^{-12} \text{ s}$) and a related wavelength in vacuum of $300 \mu\text{m}$, an energy of 4.14 meV, a wave number of 33.3 cm^{-1} and a corresponding temperature according to $h\nu = k_B T$ of 48 K.

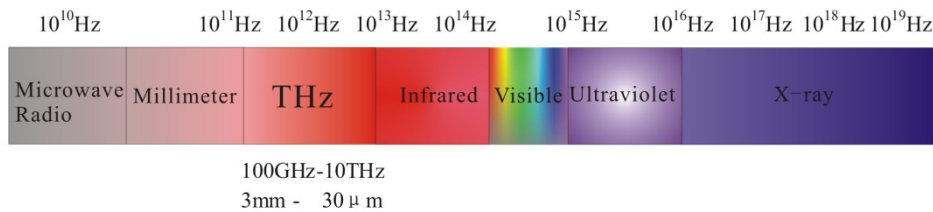


Figure 1.1: THz band in the electromagnetic spectrum.

THz radiation exists widely in our daily life, for example as part of the thermal radiation from most of the objects around us. However, the lack of radiation sources has hampered investigations in this spectral region until the 1990s. The frequency range is denoted as the THz Gap because of the lack of efficient and compact emission sources and detectors. At its low and high frequency ends are available traditional electronic and optical devices, respectively, earlier researchers tried to bridge this gap from either the higher frequency side (optics) or the lower frequency side (electronics).

THz radiation attracted so much interest during the past decades not only because of its mysterious veiling yet wide abundance, the more important reason are its own particular characteristics:

THz radiation easily penetrates many kinds of dielectric materials and non-polar liquids; therefore, it can be used to image many opaque objects [Hu95]. One of the potential applications of THz techniques is to use it as a supplement to X-rays to check manufacturing quality and perform surveillance [Cle02]. As the wavelength of THz radiation is much longer than the size of dust particles in the atmosphere, it undergoes much weaker scattering compared with optical probes; in addition, most materials have higher transparency in the THz than in the optical region

The photon energy of THz radiation is on the order of meV which is much lower than the photon energy of X-rays which is in the keV range. It is almost completely harmless in human security surveillance as well as medical tissue imaging. As water strongly absorbs THz radiation, even strong THz radiation cannot penetrate the skin of the human body, which is important for the use in surveillance.

The early work at THz frequencies has been in the use of THz spectroscopy to investigate the structure of molecules [Pal77]. Many rotational frequencies of molecules fall in this spectral region, especially for light molecules. The vibrational modes of many heavy molecules or molecules consisting of large functional groups are also expected to have broad resonances at THz frequencies [Mar00]. This is also the goal of this thesis, which is to build a high-sensitivity THz spectrometer to study the characteristics of substances in the THz frequency region.

THz waves have much higher frequencies compared with microwaves. Therefore, when used in the telecommunication area, THz waves can carry much more information. As the wavelengths of THz waves are much shorter than that of microwaves, it is much easier to control the propagation direction of THz waves compared with microwaves. THz waves show high application potential mainly in short-distance wireless communication or

outer space communication because of the strong absorption by water in the atmosphere.

As the THz spectral region lies between the ends of the infrared and microwave regions, which have been commonly studied and developed using theoretical and experimental methods, a lot of efforts have been undertaken from these two sides to bridge the THz gap.

One way is to use optical techniques to develop THz lasers; gas lasers [Cha70, Mor92], nonlinear difference-frequency lasers [Agg74, Yan73], semiconductor lasers [Kom82, Brü96], quantum cascade lasers [Fai94] have been built with frequencies in the lower THz frequency range. Another way is to use electrical techniques to increase the working frequency of microwave components, for example the development of microwave tubes [Mcm91], and solid state microwave sources [Fre91].

The advent of ultrafast lasers brought a revolutionary development in THz generation and detection techniques. Employing this technique in 1984, Auston and his colleagues used photoconducting switches that generated and detected electro-magnetic transients on the picosecond timescale in free space propagation [Aus84]. The method they employed has been commonly used and developed until now. It marked the beginning of THz optoelectronics.

Employing ultrafast laser pulses, besides photoconductive switches, several other emitter concepts have been developed such as optical rectification, surface field THz emitters, photo-Dember emitters, and phase-matched difference frequency mixing techniques.

Besides the photoconductive switch detection by Auston mentioned above, free space electro-optic sampling is another commonly used detection technique. In addition, detection methods such as bolometers, Golay cells, pyroelectric devices, and heterodyne detection using mixers have also been used.

Basically, THz detection schemes can be classified into coherent and incoherent techniques. Coherent detection measures both the amplitude and phase of the field, whereas incoherent detection measures only the intensity. A setup capable of broad band THz generation and coherent detection provides the information to determine the dispersion and the absorption of the sample, as it can simultaneously measure both the changes of the amplitude and the phase of the THz pulse induced by the interaction with sample; we call this technique THz time-domain spectroscopy (THz-TDS).

THz-TDS has several distinct advantages among other forms of spectroscopy. In the THz region, its spectral features have innumerable associations with fundamental physical processes such as lattice vibrations in crystals, molecule vibrations in organic compounds, molecule rotations, transitions and vibrations in liquid and gases, and intraband transitions in semiconductors. Therefore, since THz-TDS was realized, it has been developed into a powerful and frequently used tool for investigations in physics, chemistry, biology, materials science, medicine.

THz techniques have made progress in many aspects and have shown wide application potentials so that now, for example, THz imaging can be used in medical imaging, quality controlling in manufacturing and surveillance as security screening. Furthermore, THz radiation also shows a high potential in telecommunications, especially in outer space communication. However, to completely fill the THz gap we still have a long way to go and many difficulties to overcome.

The goal of this thesis is to improve THz-TDS with newly developed THz generation and detection techniques and furthermore, to use THz-TDS to study the physical and chemical characteristics of substances. Water and water based solutions will be studied with a reflection geometry THz-TDS. The Debye model and an extended model based on the Debye model and the harmonic damped oscillator model will be used to analyze the

measurement results of water and water based ionic solutions. We also developed a compact low-temperature THz parallel metal-plate waveguide spectrometer, which we employed for the study of the temperature dependence of photo-Dember emitters as well as the temperature dependence of the absorption lines of 1, 2-dicyanobenzene.

The thesis is organized as follows:

In Chapter 2 we review the fundamentals of THz-TDS. A common setup for THz-TDS is introduced. THz generation and detection methods using ultrafast lasers as well as a special setup for time domain spectroscopy used in this work are reviewed. The theory for interaction between electromagnetic waves and matter is also given.

Chapter 3 gives a detailed description of THz time domain reflection spectroscopy of aqueous systems. Data analysis required for data obtained in this setup will also be given. Using this setup we study the dielectric relaxation of water and water based ionic solutions. Measurement results of water and ionic solutions will be presented and analyzed with the Debye model and an extended model developed by us.

In Chapter 4, we present a compact low-temperature THz parallel metal-plate waveguide spectrometer. The theory of electromagnetic waves propagating in parallel plate waveguides will be given. Measurements of the temperature dependence of photo-Dember emitters and spectra of 1, 2-dicyanobenzene performed with this setup are presented.

Chapter 2 Fundamentals of THz time-domain spectroscopy

In this chapter, we will give a brief overview of the principles and concepts of THz time-domain spectroscopy (THz-TDS). In the following we will discuss the mechanisms of generation and detection of THz radiation used in the course of this thesis, which will focus on THz pulses generated from photoconductive emitters and photo-Dember emitters, as well as on the electro-optic detection of THz radiation. An asynchronous optical sampling (ASOPS) system for time-domain spectroscopy will also be introduced. The basic theory of interaction between electromagnetic waves and matter will also be given in this chapter.

2.1 THz time domain spectrometer

THz time-domain spectroscopy uses pulses of THz radiation to probe the properties of a material, in which the electric field $E_{r,sample}(t)$ is measured as a function of time. The corresponding frequency spectrum of $E_{r,sample}(\omega)$ can be calculated by a Fourier transform of $E_{r,sample}(t)$.

$$\tilde{E}_{r,sample}(\omega) = A(\omega) \exp[-i\phi(\omega)] = \int E_{r,sample}(t) \exp(-i\omega t) dt \quad (2.1.1)$$

From function (2.1.1), the electric field in the frequency domain, $E_{r,sample}(\omega)$, is expressed using a complex function which contains the amplitude and phase information of the THz pulses after interaction with the sample. The information from the THz spectrum of the sample can be obtained by comparison with the frequency spectrum of a reference electric field $E_{r,reference}(\omega)$ of the THz pulses without the sample. As this technique measures the electric field of THz pulses in the time domain during the measurement, it is called THz time domain spectroscopy.

Usually, materials with high absorption coefficients are better suited for reflection geometry and those with low absorption coefficients for transmission geometry. The polarization of THz pulses is determined by the orientation of the emitter (with photoconductive antenna emitters, for example, the polarization of THz emission is perpendicular to the direction of the electrodes).

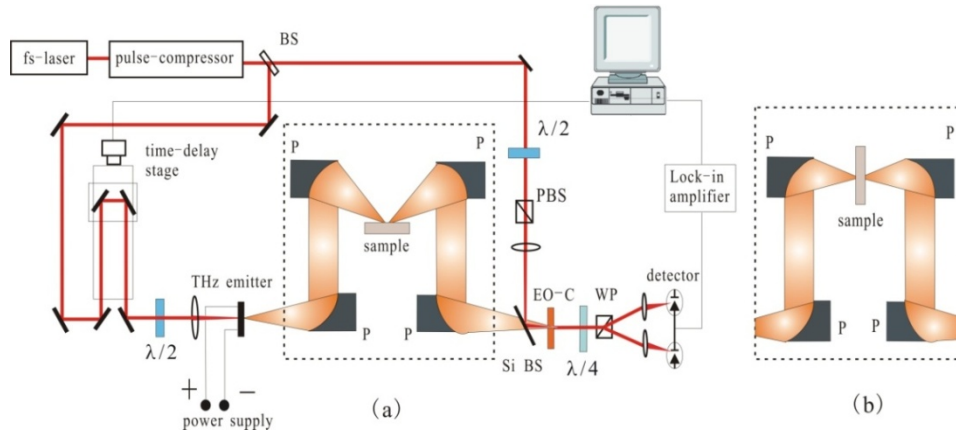


Figure 2.1: The classic layout of a THz-TDS experimental setup with (a) reflection geometry, and (b) transmission geometry (only difference shown).

A typical scheme of a THz-TDS system is shown in Fig. 2.1. The pulses from the femtosecond-laser are split into a pump and probe beam after the compressor. After passing the time delay stage, which provides a variable delay between the pump and probe beam controlled by a computer, the pump pulses are focused onto the THz emitter, exciting THz radiation. The THz pulses have durations from sub-picoseconds to a few picoseconds depending on the emitter corresponding to a bandwidth of a few THz in the frequency domain. The divergent THz pulses emerging from the emitter are collected and collimated by off-axis parabolic mirrors and focused onto the sample in either reflection (Fig. 2.1 (a)) or transmission geometry (Fig. 2.1 (b)). The THz pulses, after interacting with the sample, are collected and collimated by two more off-axis parabolic mirrors and focused onto an electro-optical crystal. The focused THz radiation pulses are brought to overlap with the focus of the probe beam on the EO crystal resulting in an electro-optic effect,

i.e. a polarization change of the probe pulse induced by the electric field of the THz pulse, in the crystal that can be detected by the detector.

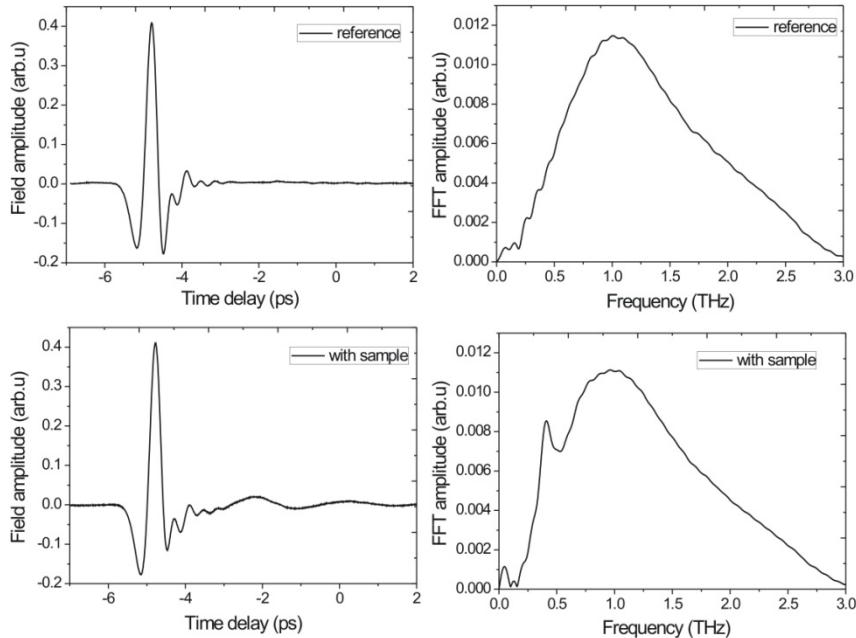


Figure 2.2: Signal (left) and related frequency spectrum (right) measured by THz-TDS system (Top: reference signal, bottom: signal with sample).

The detector provides a current signal proportional to the electric field but not to the intensity, which allows the determination of the absorption coefficient and the refractive index of the sample. Figure 2.2 gives an example of a measurement by THz-TDS, in which time-domain THz transients and the related frequency spectra are shown.

Among the many different THz-TDS geometries available, THz parallel-plate waveguides (PPWG) also attract much attention. The basic idea is to use THz pulses coupled into a parallel-plate waveguide, as the deposition of a sample film on the plate of the waveguide can provide a long interaction path length, leading to higher detection sensitivity [Gal00, Mel06, Mel09, Zha04]. We will discuss this in detail in Chapter 4.

2.2 THz generation with femtosecond lasers

There are several different methods for generating THz pulses at present. Ultrafast lasers, i.e. femtosecond laser, are commonly employed. Among the femtosecond lasers the Ti:sapphire laser is predominant. Ti:sapphire lasers have several outstanding properties, e.g. the broad gain spectrum from 650 nm to 1100 nm, high thermal conductivity, short fluorescence lifetime around 3.2 ns. Since the Kerr-lens modulated Ti:sapphire femtosecond laser was first demonstrated in the 1990s [Spe91], it has proved itself to be an essential tool for the study of ultrafast phenomena on the subpicosecond time scale and boosted the development of THz techniques. Femtosecond lasers have such short pulse durations that they can provide good time resolution and high peak intensities. By interacting with materials the short and intense pulse can induce different kinds of changes of the optical properties of the material, such as transient currents, induced polarizations, and coherent lattice vibrations, etc., which provide the possibility for the generation of THz radiation.

Employing femtosecond lasers, several methods for generating THz emission were developed, such as photoconductive switches, optical rectification, semiconductor surface field acceleration, and the photo-Dember emitter. In this thesis, photoconductive emitters and Photo-Dember emitters have been used. Therefore, we will give a detailed introduction to them.

2.2.1 Photoconductive emitter

The photoconductive emitter is one of the most important THz sources of the past 20 years.

Employing femtosecond lasers in 1984, Auston et al used photoconductive switches (known as Auston switches) that generated and detected the picosecond timescale electromagnetic transients in free space propagation

[Aus84]. Since then the photoconductive switches have been improved continually to several designs and applied for the generation of THz emission.

Common to the designs of the photoconductive switches is that two electrodes are fabricated on a semiconductor substrate providing a biasing electric field. The femtosecond laser excitation pulse is focused onto the gap between the electrodes. As the photon energy of the excitation pulse is larger than the band gap of the semiconductor, carriers will be created and then accelerated by the biasing electric field. The formed photo current leads to a change in polarization and induces electromagnetic radiation in the THz range. To have a high speed of response, semiconductors with high carrier mobility are preferred.

The main difference of the several designs is the size of exciting area where THz radiation takes place. If the separation of the electrodes is much smaller than the wavelength of the THz radiation (300 μm at 1 THz), the electrodes can not only provide the biasing electric field but also work as antennas for the out-coupling into free space (see Fig. 2.3(a)), therefore, in this case photoconductive switches with this kind of structure are also called photoconductive antennas. The separation of the electrodes in antenna structures is typically a few micrometers; therefore, a high biased field can be easily obtained with a relatively low voltage. However, the active area where the laser can excite carriers has to be small compared to the geometry of the antenna; therefore, the adjustment is quite sensitive with the spot position of the laser focus. However, this disadvantage will disappear in the case of large-area photoconductive emitters.

For a large area photoconductive emitter, a larger excitation area is possible without exceeding save levels of the optical pump power density and therefore scaling becomes possible (see Fig. 2.3(b)). But since the separation between electrodes is much larger, a much higher bias voltage is necessary.

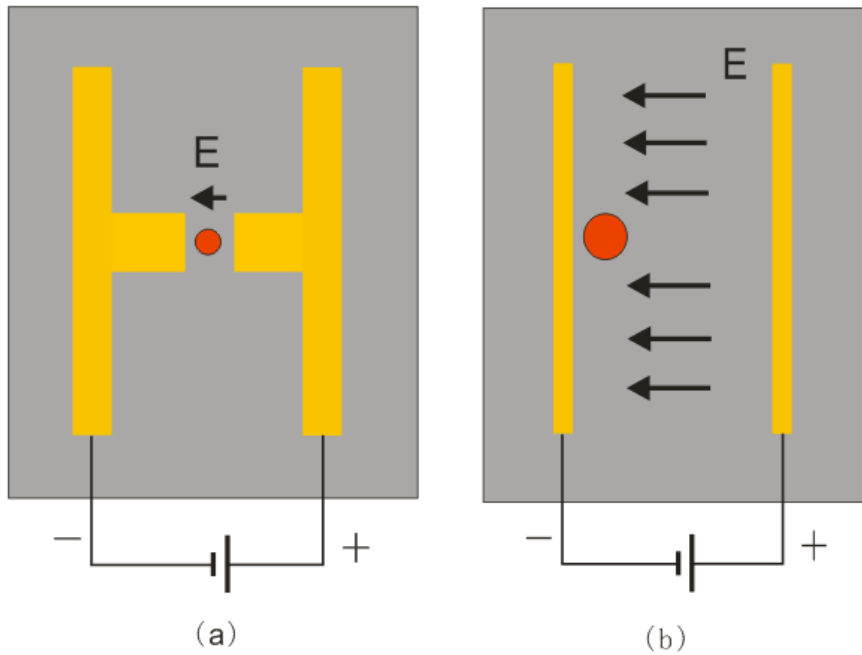


Figure 2.3: Schemes of photoconductive switch (Auston switch) THz emitters. (a) photoconductive antenna structure, (b) large-area photoconductive emitter. The gray area is the semiconductor substrate and red spot indicates the focus of the femtosecond laser.

The THz radiation detected in the far field is proportional to the time derivative of the induced photo current J :

$$E_{THz}(t) \propto \frac{\partial J(t)}{\partial t} \quad (2.2.1)$$

A good photoconductive emitter with short pulse durations requires high carrier mobility, high resistivity and short carrier lifetime. Low-temperature grown Gallium Arsenide is the most commonly used material for fabricating photoconductive emitters due to its sub-picosecond carrier lifetime [Gup92].

The output of a photoconductive emitter depends on the bias voltage and the optical pump power. When the bias voltage is low and the pump power is small, the field amplitude of the THz radiation increases linearly with both parameters [Tan97]. But since the excitation focus is small and the energy

density can easily reach levels which are harmful to the semiconductor, the THz output power saturates at high optical pump powers due to the screening of the bias field by the photocarriers. Therefore, the excitation power is limited.

Based on the structure of dipole antenna emitters, bowtie and spiral shaped antenna have also been developed. Bowtie antennas can emit broadband THz pulses but are not suitable for tuning and scaling, meanwhile, spiral antennas can also emit broadband THz pulse and are tuneable, but every frequency component of the emission has a different polarization.

Based on the photoconductive antennas, Dreyhaupt et al. [Dre05] provided the idea of a microstructured large-area photoconductive emitter which is mainly used in this thesis.

This structure combines the advantages of a large area photoconductive emitter with low voltage operation. The basic scheme is shown in Fig. 2.4. Interdigitated finger electrodes are fabricated on the semi-insulating GaAs substrate with metallization shadowing every second space between electrodes. Applying an external biasing voltage, an electric field is formed in the direction of the arrows shown in the figure. The metallization insulator blocks the electric field in the other direction, which gives the bias field a uniform direction. Upon illumination with a Ti:sapphire laser at 800 nm, carriers are generated and accelerated in the non-shadowed gaps in a uniform direction, such that the THz radiation emitted from each gap will interfere constructively in the far field.

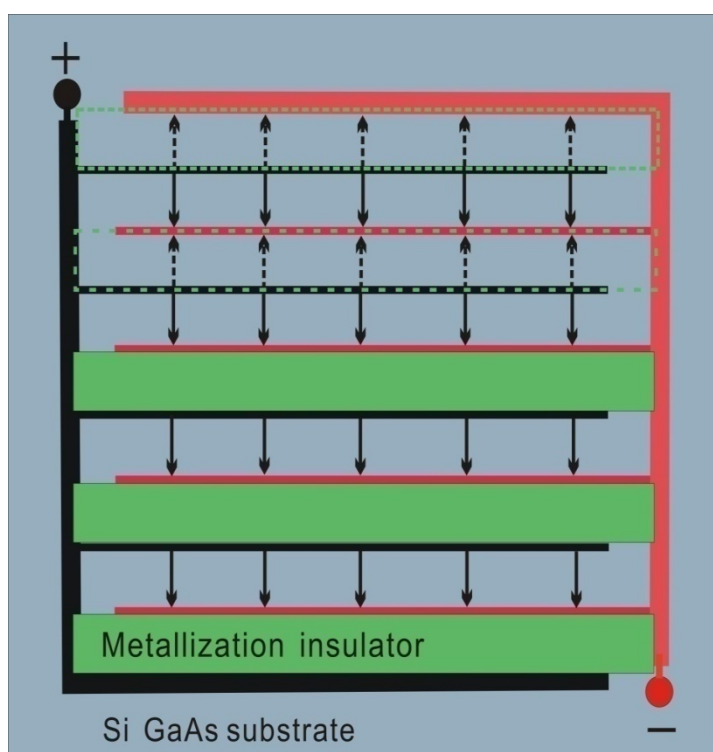


Figure 2.4: Schematic sketch of the THz emitting MSM structure; (1) interdigitated finger electrodes (black/red), Si GaAs substrate (gray colour), and opaque metallization (green) shadowing one electric field direction. The electric field direction is indicated by arrows.

For this kind of structure, the semiconductor substrate requires a high carrier mobility and high efficiency of carrier generation by excitation. The spacing between the individual fingers is $5\ \mu\text{m}$, such that a low bias voltage (around 10 V) is sufficient to provide an adequate electric field. The structure has a scalable active area from $1\ \text{mm}^2$ to $1\ \text{cm}^2$, so tightly focusing the excitation beam is not critical. The polarization of the THz emission is determined by the electrodes of the structure, in the case of that shown in Fig.2.4, the polarization is linear and perpendicular to the electrodes.

2.2.2 Photo-Dember emitter

Compared with photoconductive emitters biased with an external voltage, non-biased THz emitters are attracting more and more attention because they

offer the possibility of much compacter THz emission devices. The study of non-biased THz emitters focuses mainly on two areas: one is the THz emission from the surface currents of semiconductors, and the other is the THz emission by the photo-Dember effect in semiconductors. In the following we will mostly focus on the photo-Dember effect.

When a highly absorbing semiconductor is illuminated by an ultrafast laser, a strong spatial gradient of the generated electron-hole pairs will be formed perpendicular to the semiconductor surface. Electrons and holes diffuse with quite different speeds (the diffusion constant of electrons is much larger than that of holes), leading to a build-up of a space charge field between the diffusing carrier distributions. This charge field is called the photo-Dember field and is the origin of THz emission [Dek96, Gu02]. This phenomenon was named the photo-Dember effect shortly after it was discovered by Harry Dember in 1931 [Dem31].

The photo-Dember field caused by the charge carrier diffusion can work as a Hertzian dipole. The emitted THz radiation E_{THz} is proportional to the time derivative of the charge carrier's diffusion current J :

$$E_{THz}(t) \propto \frac{\partial J(t)}{\partial t}, \quad (2.2.2)$$

As the induced diffusion current is proportional to the carrier gradient $\frac{\partial^2 n}{\partial x^2}$ and the diffusion constant D_i given by the Einstein relation $D_i = \mu_i K_B T_i / e$, where μ_i is the mobility, K_B is the Boltzmann constant, T_i is the temperature of the carrier distribution, and the index i denotes electrons or holes. Therefore, the function (2.2.2) can be expressed as:

$$E_{THz} \propto \frac{\partial}{\partial t} \left(\frac{\partial^2 n}{\partial x^2} (D_+ - D_-) \right) \quad (2.2.3)$$

THz radiation from the photo-Dember effect has been examined in many different strongly absorbing semiconductor materials with an intrinsic absorption length under a given excitation wavelength [Asc05, Asc06, Gu02, Hey03, Has04, Nak04, Que09, Urb05]. Typically this absorption length is below 100 nm. Semiconductors with narrow band gaps and high electron mobility such as InAs (0.36 eV) or $\text{In}_{0.53}\text{Ga}_{0.47}\text{As}$ (0.74 eV) are preferred for the THz radiation from the photo-Dember effect, because this kind of material can provide stronger carrier gradients and higher carrier mobility which enables large THz fields according to function (2.2.3).

During the process of THz radiation through the Dember effect, the time-dependent dipole which gives rise to the THz emission is oriented perpendicular to the excited surface, i.e. parallel to the optically generated carrier gradient, which leads to a low out-coupling efficiency. A relatively efficient output coupling can be achieved when the surface is excited under an angle of 45° , but compared to theoretical calculations with the dipole parallel to the semiconductor surface, the ratio of out-coupling efficiency is only 1/2.

Another disadvantage of normal photo-Dember THz emitters is the low magnitude of the carrier gradient which is given by the intrinsic absorption coefficient of the semiconductor at the excitation wavelength, which leads to a bandwidth of the THz emission typically below 1 THz.

Both of these disadvantages can be solved if the carrier gradient is oriented parallel to the excited surface, as in this case the time-dependent dipole is oriented parallel to the surface. Based on this concept, we have built a large area lateral photo-Dember emitter [Kla10].

The principle of THz pulse generation and the basic structure of such a device are shown in Fig. 2.5. Stripes of metallic gold are deposited onto photoresist bars on the surface of a semiconductor. Metal deposition under an

angle is used to block portions of the pump beam, leading to a strong photo-carrier concentration gradient at the corner of the metal stripes. A parallel carrier gradient and related time-dependent dipole can be formed. The magnitude of this gradient can be significantly higher than that obtainable through the intrinsic absorption coefficient of the material in a conventional geometry, i.e. the carrier density drops within a few nanometres in the semiconductor. This effect increases the amplitude and the bandwidth of the THz emission significantly.

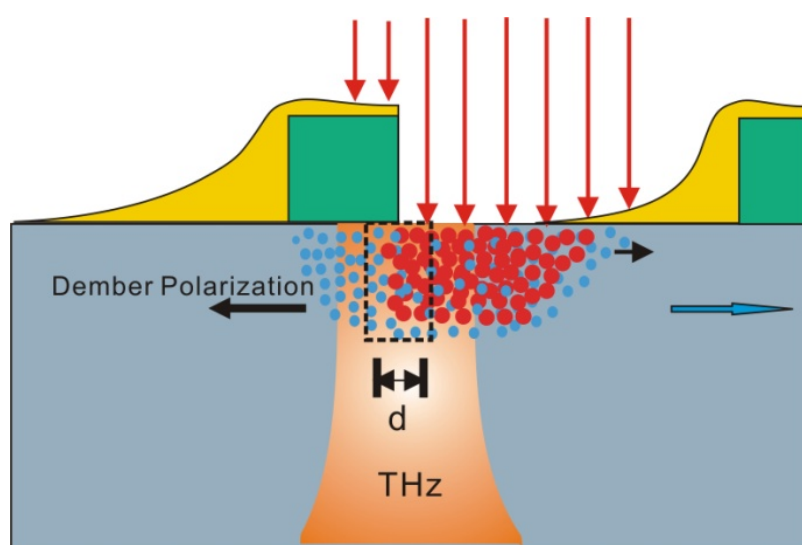


Figure 2.5: Sketch of THz generation from the Dember emitter through lateral diffusion currents. Only two gold stripes (yellow) and photoresist bars (green) are shown. A strong carrier gradient is formed at the edge of the photoresist bars, with electrons (blue spheres) and holes (red spheres) [Kla10]. The faster diffusion of electrons leads to the rapid build-up of a polarization parallel to the surface with preferred THz emission into forward direction.

The different diffusion rates of photocarriers result in a lateral charge separation parallel to the surface. The acceleration of photo-electrons relative to holes leads to the emission of a THz transient in forward direction with a polarization perpendicular to the stripes. The gold layer has a gradually decreasing thickness that substantially weakens the photocarrier gradient in the direction away from the edge. This strongly reduces the

radiation dipole vector in the reverse direction, which is necessary to build up a significant radiation signal in the far-field. The structure depicted in Fig. 2.5 is repeated with a period of $3 \mu\text{m}$ to form a large area emitter. More than 10 of these stripes are covered by the spot of the pump laser.

As analyzed above, a significant difference in diffusion constants for electrons and holes is important for THz generation via the photo-Dember emitter. We built a photo-Dember emitter with high THz generation efficiency based on photoresist bars fabricated on $\text{In}_{0.53}\text{Ga}_{0.47}\text{As}$ grown on InP, as the mobility ratio for electrons and heavy holes in undoped $\text{In}_{0.53}\text{Ga}_{0.47}\text{As}$ at 300 K is about 40 ($12000 \text{ cm}^2/\text{Vs}$ and $300 \text{ cm}^2/\text{Vs}$, respectively) [Kla10], suggesting that the electrons diffuse much faster than the holes. The THz pulse emitted via the photo-Dember emitter in free space and the corresponding spectrum are shown in Fig. 2.6.

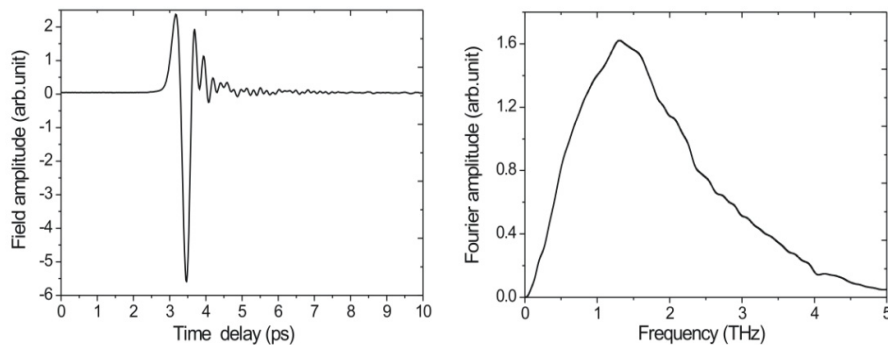


Figure 2.6: Time-domain THz emission from photo-Dember emitter and corresponding Fourier amplitude spectrum.

It is worth noting that THz generation by the photo-Dember effect is different from that of generation by a semiconductor surface current acceleration. In GaAs for instance, there exists a surface state, at which the Fermi level is pinned at a different energy from the inner part causing an energy band bending near the surface and the build up of an electric field.

Because of the existence of this electric field the density of electrons near the surface is much lower than in the inner part (for n-doped GaAs), which is what we call the depletion layer. When GaAs is excited by an ultra-fast laser the generated electron-hole pairs in the depletion layer will separate because of the electric field and form a time dependent polarization. This polarization is the origin of THz radiation.

2.3 THz Detection

The methods of THz detection can basically be classified into two methods, coherent and incoherent detection. The difference is that coherent detection measures both the amplitude and phase of the THz field while incoherent detection measures only the intensity [Lee09]. In this work, only coherent detection for THz-TDS is employed. At present, there are two kinds of coherent THz detecting methods which are commonly used, one is the photoconductive detection and the other one is the so called electro-optic (EO) detection.

2.3.1 Photoconductive detection

The principle of photoconductive detection is almost the reverse of THz generation from photoconductive antennas: A probe pulse generates carriers in the semiconductor substrate of a photoconductive antenna. The carriers are accelerated by the THz field and form a current. In the ideal case of short enough carrier life-times in certain semiconductor substrates the measured current will be proportional to the instantaneous THz field. In order to have a short carrier life-time, low temperature grown GaAs is an ideal material [Gup92]. Compared with EO detection, photoconductive detectors have a relatively small volume.

EO detection is becoming more and more popular because of its high bandwidth and the possibility to quantitatively measure the THz field. The

experimental setups used in this work are based on the EO detection, which is described in the next section.

2.3.2 Electro-optic detection

Electro-optic detection is based on the electro-optic effect (Pockel effect). In electro-optic materials, the optical properties can be changed using a slowly varying (compared with the frequency of light) applied electric field. One phenomenon is the change of the refractive index proportional to the electric field, thereby inducing birefringence. The birefringence will change the polarization of the probe beam, which can then be measured.

In the case of THz EO detection, ZnTe crystals are commonly used as the EO crystal, where the THz pulse supplies the electric field. The principle of operation of EO detection is shown in Fig. 2.7.

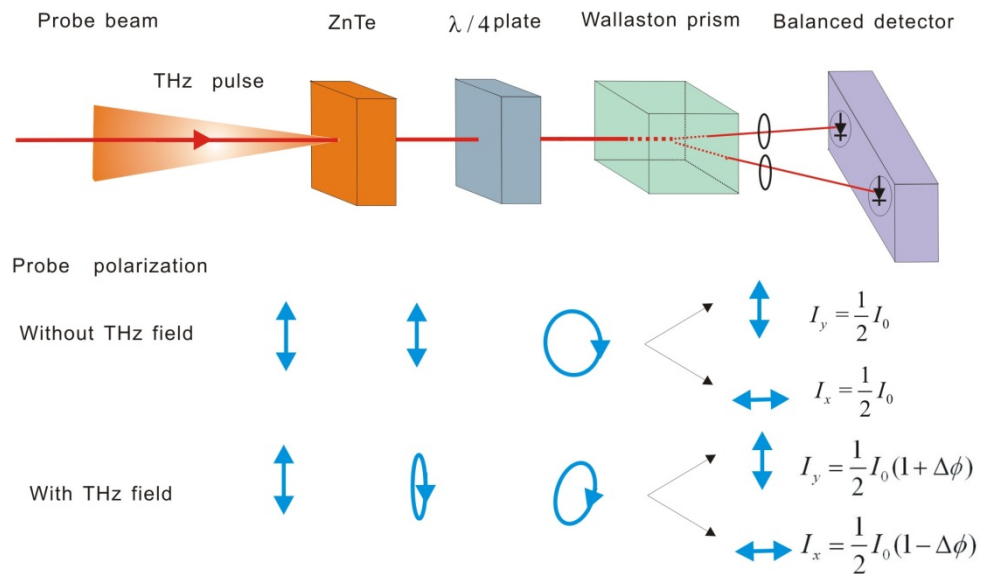


Figure 2.7: Principle of operation of EO detection with a balanced detector, blue symbols show the polarization with and without THz field, I_0 is the intensity of the probe beam after passing through a Wollaston prism, I_x and I_y are the orthogonal components received by the two photodiodes of the balanced detector, $\Delta\Phi$ is the intensity difference [Lee09].

A linear ultrafast laser beam, which functions as the probe beam as well as the generated THz pulse, coincide on the ZnTe crystal as shown in Fig. 2.1. When the linearly polarized probe beam propagates through the ZnTe crystal, the temporarily induced birefringence in the ZnTe crystal will change the linear polarization of the probe beam into a slightly elliptical polarization. After passing through a $\lambda/4$ plate, a nearly circular but slightly elliptical polarization will be achieved. A Wollaston prism (or a polarizing beam splitter) will split the probe beam into linearly s- and p-polarized components (defined by the plane of incidence of the Wollaston prism) which will be received by the two separate photo-diodes of the balanced detector. Comparing the intensities of the two orthogonal components, an intensity difference proportional to the THz field is obtained.

Theoretical and experimental studies have been undertaken to clarify the relation between the intensity difference and the THz field [Lee09, Win97, Nah96]:

$$E_{THz} = \frac{I_s}{I_0} \frac{\lambda}{2\pi n_0^3 r_{41} L} \quad (2.3.1)$$

where E_{THz} is the THz electric field, I_s is the intensity difference measured by the detector, I_0 is the incident probe intensity after the Wollaston prism, λ is the wavelength of the probe beam, n_0 is the refractive index of the EO crystal at the frequency of the probe beam, r_{41} is the electro-optic coefficient and L is the thickness of the EO crystal.

Equation (2.3.1) indicates that a thicker EO crystal leads to a larger intensity difference for the detector (for a certain THz transient, larger L leads to a larger I_s), i.e. to larger measured amplitude of the THz signal. However, this equation does not consider the phase mismatch between the phase velocity of the THz wave inside the crystal and the group velocity of the infrared probe pulse. In an ideal case they should be equal, otherwise the THz pulse and the infrared probe pulse will traverse the EO crystal with different velocities which will reduce the detectable bandwidth [Lei99]. For

thicker EO crystals, absorption induced spectral modulation should also be considered. Therefore the proper thickness of the EO crystal should be considered for an optimization of THz detection.

It should be noted that the balanced photo-detector is not always necessary for the EO detection. In the course of this thesis, measurements were mostly taken with single photo-diode detection, as in the setup based on asynchronous optical sampling (which will be introduced in the following sections), the high scan rates reduce the influence of laser noise leading to a shot-noise limited detection. The details can be found in Ref. [Tho10].

ZnTe crystal is commonly used for EO detection because of its excellent optical properties: The electro-optic coefficient r_{41} of ZnTe crystal is as high as 3.9 pm/V. The phase velocity at 1 THz is close to the group velocity at a wavelength of 800 nm in ZnTe crystal (at 822 nm, they are exactly equal) [Wu96] which is commonly used for THz generation and detection. However, the bandwidth of EO detection is limited by the TO phonon resonance of ZnTe crystal at 5.3 THz [Lee09, Sch01]. If a wider bandwidth is required, GaP could be used which has a TO phonon resonance at 11 THz, but a lower electro-optic coefficient [Ber89].

2.3.3 Femtosecond lasers and conventional time delay setup

As described above, THz radiation from photoconductive emitters or photo-Dember emitters as well as THz detection with electro-optic sampling require ultrafast femtosecond lasers. For this thesis, two different titanium-doped sapphire (Ti:sapphire) lasers were employed to generate ultrafast near-infrared pulses. Both lasers are based on Kerr-lens mode-locking [Spe91, Sut99]. One laser has a pulse repetition rate of 80 MHz (Spectra-Physics Tsunami), working at a central wavelength of 800 nm (wavelength range from 715 nm to 855 nm) and an output pulse length of about 50 fs. The other laser system employed two separate mode-locked Ti: sapphire oscillators (one for pump, another for probe) in one enclosure (Giga Optics Gigajet

TWIN), with repetition rates around 1 GHz and output pulse lengths of about 45 fs. Both lasers were pumped by a diode pumped frequency-doubled Nd:YVO₄ laser (Spectra-Physics Millennia Pro 10) with a wavelength of 532 nm and a power of 10 Watt (in the latter a beam splitter was positioned after the pump laser in order to pump the two oscillators separately).

In Section 2.1 and Figure 2.1, we depicted the commonly used method with a controllable motorized linear translation stage providing a variable time delay between the pump and probe pulses. The time delay is achieved by changing the relative path lengths of pump and probe through the shifting of the linear stage on which a retroreflector is mounted. This method has been employed in a large number of setups and contributed to many excellent measurements. However, the acquisition time for taking a THz transient in this way is very long due to the maximum speed of the translation stage in combination with lock-in detection. This is a disadvantage of conventional THz-TDS systems.

In order to have a shorter acquisition time, we improved this setup by using a retroreflector mounted on a vibrating membrane of a loudspeaker (shaker). This shaker was positioned on the pump or probe paths and was driven with a frequency of around 20 Hz. In this way the time delay is varied continuously and a single scan can be performed in 50 ms. The time resolution was determined by the bandwidth of the detector/amplifier as well as the sampling rate of the oscilloscope measuring the diode signal. Since the acquisition time depends on the frequency of the oscillation of the shaker (not for the shot-noise limited detection), a higher resolution could be achieved by increasing the sampling rate of the oscilloscope without adding to the acquisition time. However, as the velocity of the retroreflector is not constant, one has to calibrate the time axis before taking a measurement. The amplitude of the shaker's oscillations is typically less than 1 cm, therefore the scan window is limited to 12-18 ps in our setup. Additionally, the shaker also tends to cause mechanical vibrations on the optical table as well as

slightly altering the beam cross-section or focus due to the change of path length.

To eliminate the drawbacks mentioned above, we used another technique called ‘asynchronous optical sampling’ (ASOPS). Most of the measurements for this thesis were taken with this system which we will have a detail introduction in the following sections.

2.3.4 Asynchronous optical sampling technique

ASOPS is based on the second laser system mentioned above, i.e. two separate Ti:sapphire oscillators delivering pump and probe, respectively. The repetition rates of the two femtosecond lasers are f_1 and f_2 and both of them have values around 1 GHz with a slight offset, $\Delta f = f_1 - f_2$. In the setup of this work the offset is 2 kHz. The laser with repetition rate f_1 works as pump laser (also called slave laser) for THz generation, while the laser with repetition f_2 works as probe laser (also called master laser) for electro-optical sampling. The frequency offset will automatically produce an increasing time delay between the pump and probe pulses without any mechanical delay line. The pulse trains of the two lasers in the time domain are shown in Fig. 2.8.

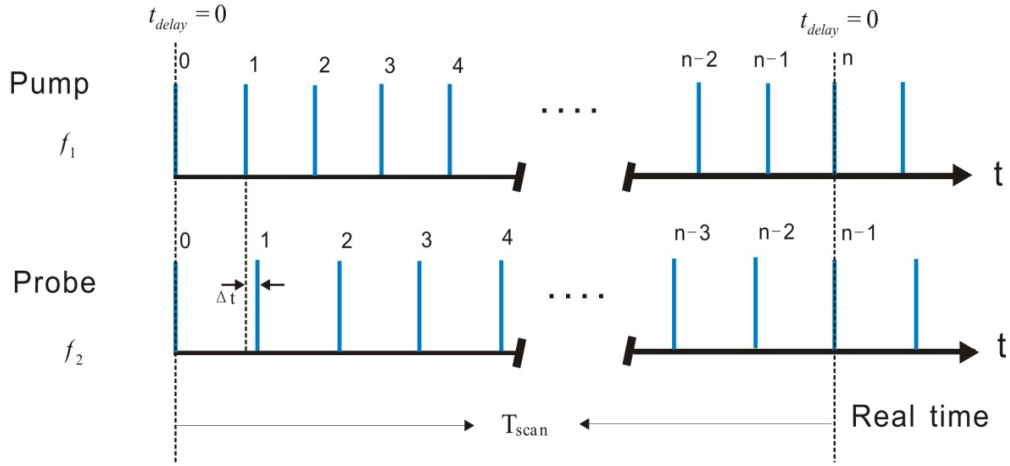


Figure 2.8: Scheme of pump and probe pulse trains in asynchronous optical sampling. Further explanations are given in the text.

The time spacings of the consecutive laser pulses are $1/f_1$ and $1/f_2$, respectively. The pulses of the lasers coincide at some temporal point as marked in Fig. 2.8 with $t_{\text{delay}}=0$. As the repetition rate of the probe laser is lower than that of the pump laser, the following pulse from the probe laser will have a time delay $\Delta t = 1/f_2 - 1/f_1 = \Delta f / f_1 f_2$ compared to the corresponding pulse of the pump laser. The pulses of both lasers will coincide again after n periods of the pump laser and $n-1$ periods of the probe laser, and after that a new measurement window is sampled. The time delay between the consecutive pulse pairs has a linear increase proportional to the real time between the coinciding points with a relation $t_{\text{delay}} = i\Delta t$. The maximum time delay is $t_{\text{delay,max}} = (n-1)\Delta t$. The time between the two coincident pulses is the scan time for a measurement and is determined by $T_{\text{scan}} = 1/\Delta f$. In the case of the ASOPS system used here the time delay unit is $\Delta t = 2$ fs, the maximum time delay is $t_{\text{max-delay}} \approx 1$ ns and the scan time is $T_{\text{scan}} = 500$ μs . The time resolution should be Δt according to the theoretical analysis, however, in practical measurements the real time resolution is limited by many experimental conditions, for instance, the fluctuations of the

lasers repetition rate which result in a varying Δf or the bandwidth of the data acquisition electronics (sampling oscilloscope, photo-detection) [Bar06]. The real time resolution of the ASOPS system used in this course of work is around 50 fs [Geb10].

ASOPS systems have many advantages among other pump and probe methods: First of all, the absence of the mechanical time delay stage, which provides the possibility for high scanning rates and avoids the associated defocusing effects. The high scanning rate provides video rate acquisition of time-domain THz transients hence allowing easy on-line alignment and optimization of the THz signal. Secondly, since both the pump and probe optical paths are not changed during the measurement, undesired variations in the spot size on the THz emitter and the detection crystal can be avoided. Furthermore, individual lasers can be used for pump and probe which provides the possibility for different wavelengths depending on the band gap of the sample under study and choosing an optimum wavelength for EO-detection.

The disadvantages of ASOPS systems are the requirement of relatively complicated components for optical and electronic modulation and additional expenses. However, as this technique continues to develop, the compactness and many other advantages of ASOPS system will draw more and more attention in the future.

2.3.5 Setup of the ASOPS system

The principle of the ASOPS technique has been introduced in the above sections. In the following paragraphs I will introduce the setup of the ASOPS system used for this thesis. This setup has the same specifications as the one described in Ref. [Geb10]. A sketch of this system is shown in Fig. 2.9.

The core part of this system are two mode-locked Ti:sapphire oscillators in an enclosure (Giga Optics Gigajet TWIN). The repetition and pulses features have been mentioned in above sections.

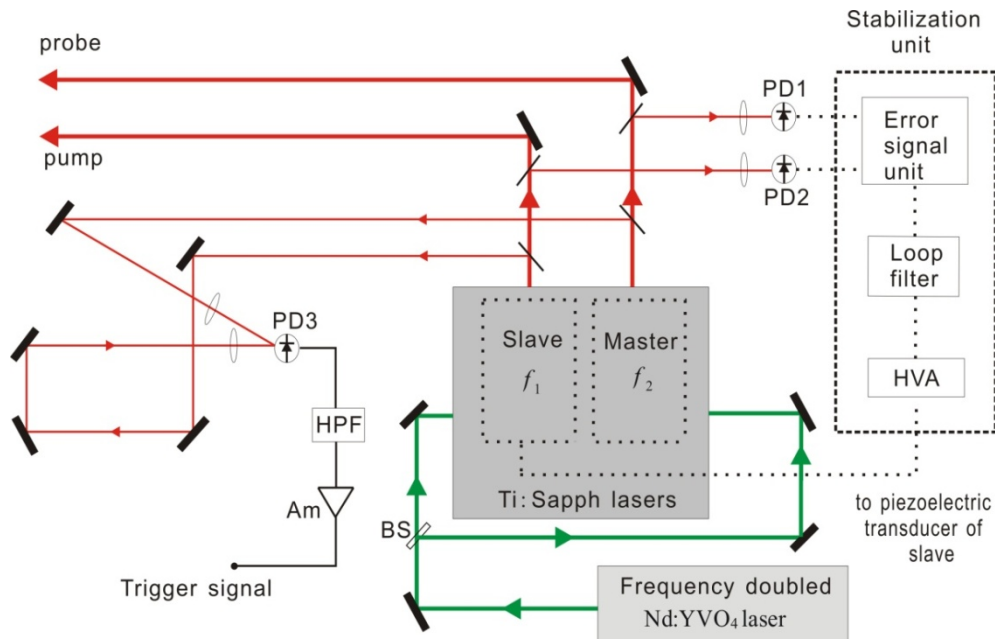


Figure 2.9: Sketch of the ASOPS system used for of this work. Green lines are laser beam from pump laser with wavelength 532 nm, red lines are mode-locked beams from Ti:sapphire lasers with wavelength around 800 nm, dotted lines are electrical wires. PD is short for photo detector, Am is short for amplifier, HPF is short for high-pass filter, BS is short for beam splitter and HVA is short for high-voltage amplifier.

The offset of the repetition rates between the pump and probe femtosecond oscillators is stabilized by an active electronic feedback. The feedback is achieved by mounting two of the mirrors in the cavity on stages controlled by piezoelectric transducers (one for coarse movements and one for fine movements); therefore the cavity length and its related repetition rate can be controlled by driving the mirrors through the transducers. There is a stabilization device to monitor the repetition rates of both oscillators and output voltages to the transducers according to the deviation of the repetition

rates. In this way, a phase-locked loop is formed. The detailed scheme of the stabilization device is described in Ref. [Geb10].

To provide a good signal-to-noise ratio, the ASOPS system requires a large number of signal averages. Therefore, an accurate trigger signal to start the scans at the very same time becomes important. The accurate trigger signal is achieved in this way: Two branches of the pump and probe beams are split off by pellicle beam-splitters and then commonly focused onto a GaP photo-diode. When the pump and probe pulses arrive at the photo-diode at the same time a signal is generated due to two-photon absorption. This signal is first filtered by a high-pass filter and then amplified by an amplifier and finally used to trigger the A/D converter. Therefore the trigger signal can insure that the scan starts only when the pump and probe pulses arrive at the diode simultaneously. A mechanical translation stage is used here to delay the pump pulses in order to shift the trigger signal to an arbitrary time delay as desired.

2.4 Theory of interaction between light and matter

In this thesis we deal with liquid systems and molecular solids that are studied with spectroscopic techniques. In order to understand the effects of the physical properties of the systems under spectroscopic measurement we first need to understand how the THz beams interact with the system. Therefore, we will discuss how electromagnetic waves interact with a medium. This section is largely based on references [Gri99, Mor08, Tie10b, Mit08].

Any physical description of electromagnetic waves is based on Maxwell's equations, the differential forms of which are as follows:

$$\nabla \times \vec{E} = -\frac{\partial \vec{B}}{\partial t} \quad (2.4.1)$$

$$\nabla \cdot \vec{D} = \rho \quad (2.4.2)$$

$$\nabla \cdot \vec{B} = 0 \quad (2.4.3)$$

$$\nabla \times \vec{H} = \vec{j} + \frac{\partial \vec{D}}{\partial t} \quad (2.4.4)$$

where \vec{E} is the electric field, \vec{B} the magnetic field, \vec{D} the dielectric displacement, \vec{H} the magnetic field intensity, ρ the free charge density and \vec{j} the free current density. Furthermore, $\nabla \cdot$ is the divergence operator and $\nabla \times$ the curl operator.

Electromagnetic waves propagate in a medium; therefore it is necessary to consider the characteristics of the medium. Relationships describing the characteristics of the substances in the presence of fields are called material equations. In isotropic materials they give:

$$\vec{D} = \varepsilon \vec{E}, \quad \vec{B} = \mu \vec{H}, \quad \vec{j} = \sigma \vec{E} \quad (2.4.5)$$

Where $\varepsilon = \varepsilon_0 \varepsilon_r$ is the permittivity, ε_0 the vacuum permittivity and ε_r the relative permittivity (also called dielectric constant); $\mu = \mu_0 \mu_r$ is the magnetic permeability, μ_0 the vacuum permeability and μ_r the relative permeability; σ is the conductivity. The dielectric displacement can be further expressed with:

$$\vec{D} = \varepsilon_0 \vec{E} + \vec{P} \quad (2.4.6)$$

where $\vec{P} = \varepsilon_0 (\varepsilon_r - 1) \vec{E} = \varepsilon_0 \chi_e \vec{E}$ is the electric polarization with the electric susceptibility χ_e describing the capability of a dielectric to be polarized. This polarization arises because of positive and negative charges experience a force in opposite directions by an electric field at a given point in space as a function of time. For neutral atoms this force will lead to slight displacements of the charges (the electrons and nuclei) which are called induced dipoles; for molecules with a permanent dipole (water for instance)

this force may induce molecular rotations (for the low frequencies discussed in this thesis, for high frequencies the mechanism will be different) which will align the dipole directions with the electric field.

In a nonmagnetic isotropic medium without free charges, the differential form of the Maxwell equations can be simplified to:

$$\nabla \times \vec{E} = -\frac{\partial \vec{B}}{\partial t} \quad (2.4.7)$$

$$\nabla \cdot \vec{E} = 0 \quad (2.4.8)$$

$$\nabla \cdot \vec{B} = 0 \quad (2.4.9)$$

$$\nabla \times \vec{B} = \mu_0 \varepsilon \frac{\partial \vec{E}}{\partial t} \quad (2.4.10)$$

By taking the curl of Eq. (2.4.7) and substituting the derivative of Eq. (2.4.10) as well as using Eqs. (2.4.8) and (2.4.9), the electric field follows:

$$\nabla^2 \vec{E} = \mu_0 \varepsilon \frac{\partial^2 \vec{E}}{\partial t^2} \quad (2.4.11)$$

which is known as the wave equation, where ∇^2 is the Laplace operator.

Solving Eq. (2.4.11) in the Fourier domain with wave vector \vec{k} and angular frequency ω , a general solution for the electric field is:

$$\vec{E}(\vec{r}, t) = \int_{-\infty}^{\infty} E_0(\omega) e^{i(\omega t - \vec{k}(\omega) \cdot \vec{r})} d\omega \quad (2.4.12)$$

where $\vec{r}(\vec{x}, \vec{y}, \vec{z})$ is the space coordinate and t the time. \vec{k} points in the propagation direction of the electromagnetic waves and has a dispersion relation with angular frequency ω :

$$k = \omega \sqrt{\mu_0 \varepsilon} = \omega \sqrt{\mu_0 \varepsilon_0 \varepsilon_r} \quad (2.4.13)$$

The component $E_0(\omega)$ is determined by $E_0(\omega) = \int_{-\infty}^{\infty} E(\vec{r} = 0, t) e^{i\omega t} dt$.

Considering Eq. (2.4.13), the phase velocity of electromagnetic waves is

$$\frac{\omega}{k} = \frac{1}{\sqrt{\mu_0 \epsilon_0} \sqrt{\epsilon_r}} = \frac{c}{\sqrt{\epsilon_r}} \quad (2.4.14)$$

where the phase velocity of electromagnetic waves in vacuum is $c \equiv \frac{1}{\sqrt{\mu_0 \epsilon_0}}$.

Eq. (2.4.14) means that the travelling speed of electromagnetic waves in such a medium will be reduced by $\sqrt{\epsilon_r}$; therefore, the refractive index $n \equiv \sqrt{\epsilon_r}$ is introduced. In a non-ideal medium (most of the substances in the world), electromagnetic waves will be attenuated (absorption); hence the complex refractive index appears as

$$\hat{n}(\omega) = n(\omega) + i\kappa(\omega) = \sqrt{\hat{\epsilon}_r(\omega)} \quad (2.4.15)$$

Here, $n(\omega)$ is the refractive index and κ is the extinction coefficient. Combing with the complex refractive index, Eq. (2.4.12) can be rewritten as

$$E(z, t) = \int_{-\infty}^{\infty} E_0(\omega) e^{i\omega(t - \hat{n}z/c)} d\omega = \int_{-\infty}^{\infty} E_0(\omega) e^{i\omega(t - nz/c)} \cdot e^{-\omega\kappa z/c} d\omega \quad (2.4.16)$$

The extinction coefficient of the complex refractive index leads to an exponential decay of the amplitude of electromagnetic waves. Substituting with the frequency dependent absorption coefficient $\alpha(\omega) \equiv 2\kappa(\omega)\omega/c$ we can obtain the Lambert-Beer law from Eq. (2.4.16)

$$\frac{I}{I_0} = \frac{E(r, t)E^*(r, t)}{E(0, t)E^*(0, t)} = \int_{-\infty}^{\infty} e^{-\alpha(\omega)r} d\omega \quad (2.4.17)$$

Here I is the intensity of the electromagnetic waves after traversing a medium while I_0 is the incident intensity. Here, scalars were used instead of vectors to simplify the calculation.

So far, the interaction of electromagnetic waves with matter has been explained. Spectroscopic measurements with samples provide information about the influence of the dielectric constant of the samples on the electromagnetic waves, which can be related to the polarizations induced in a sample in a microscopic picture.

Chapter 3 THz time domain reflection spectroscopy of aqueous systems

In this chapter we study the dielectric relaxation of water and water based solutions using our THz time domain reflection spectroscopy (THz-TDS) setup. We will start with a short introduction to the physical background of liquid molecule motions in the THz region, after which we will give a detailed description of the setup for THz time domain reflection spectroscopy used in this thesis. Calculations and analysis based on this setup will also be given. Liquid water and water based ionic solutions will be used as samples in this setup. After an introduction to the water molecule, we will turn to the description of interactions between the electromagnetic waves and water molecules. The orientation polarization of water molecules leading to the relaxation phenomena will be described in detail (Debye model). A model based on a harmonic damping oscillator will be introduced to describe the ions' motions in water solutions. Measurements results of water and water solutions will be performed and analyzed with the Debye model and an extended model developed in this thesis.

3.1 General introduction

Molecular motions in liquids are relatively difficult to study compared with gas and solid state because the well known descriptions of molecular dynamics in gases and solids (crystals) are not truly applicable. The conventional description for gas molecules is that a single molecule travels and rotates freely until interrupted by occasional collision with others. On the other hand, in solids the structural layout of the lattice provides a much stronger electrovalent or covalent bond which binds the molecule to a fixed equilibrium position; in this case it is better to consider a unit cell rather than a single molecule. In the case of the liquid phase, the intermolecular

interactions lie in-between. However, rotational and vibrational motions of many molecules including liquid molecules (which will be described in more detail in the following sections) are often characterized on the picosecond time scale, and therefore can be studied by THz spectroscopy.

When using optical or spectroscopic techniques to study the interaction of matter with electromagnetic waves, the complex refractive index $\tilde{n} = n + ik$ is commonly used to describe the properties of matter, where the real part of the refractive index, n , indicates the phase velocity and the imaginary part, k , indicates the magnitude of absorption losses. The refractive index of matter is determined by the relative permittivity $\tilde{\epsilon}$ (dielectric constant) and relative permeability $\tilde{\mu}$, with $\tilde{n}^2 = \tilde{\epsilon}\tilde{\mu}$. For non-magnetic materials, $\tilde{\mu} \approx 1$ at optical frequencies, therefore the complex refractive index can be determined by $n + ik = \sqrt{\tilde{\epsilon}}$. The dielectric constant can be expressed by $\tilde{\epsilon} = \epsilon_1 + i\epsilon_2$ which has the real and imaginary parts ϵ_1 and ϵ_2 . Therefore, the conversion between the refractive index and the dielectric constant has this relation:

$$\begin{aligned}\epsilon_1 &= n^2 - k^2 \\ \epsilon_2 &= 2nk\end{aligned}\tag{3.1.1}$$

When THz spectroscopy is used to study polar molecules in a liquid, a weak, spatially and periodically varying electric field provided by THz pulses will act on the molecules. A polarization of the molecules will be created according to the electric field, i.e. a dielectric response, which will affect the reorientations, rotations and vibrations of molecules. Since the reorientation and relaxation response associated with intermolecular fluctuations of liquid molecules can be observed with THz spectroscopy, this method provides access to the understanding of the physical and chemical properties of liquids on a molecular level. Therefore, using THz spectroscopy to study the dynamics of liquid molecules has become attractive and important, and could be a nice supplement to cover the frequencies that are

rarely reached by conventional dielectric microwave spectroscopy and FIR spectroscopy.

Since the first THz-TDS measurement was performed to measure rotational lines in water vapour in 1989 [Ext89], THz-TDS was frequently used to investigate liquids and many other materials. There are typically two kinds of geometries in THz-TDS which are widely used, transmission and reflection geometries. Rønne et al. and Jepsen et al. have used THz-TDS in reflection geometry to study the dielectric response of liquid water including the temperature dependence and also some organic solutions [Jep07, Jep10, Møl09, Røn97, Røn99, Røn00, Røn02]. Hirori et al. and Ngai et al. have built an attenuated total reflection THz-TDS system to study water dynamics and biological solutions at THz frequencies [Hir04, Nag06, Yad08, Yad09]. Tielrooij et al. have built a THz-TDS system in transmission geometry to study the THz dynamics of ions in water [Tie09, Tie10a].

In this thesis I used a reflection-geometry THz-TDS system. Compared to the transmission geometry, a reflection setup is especially applicable to highly absorbing liquids, as dipolar molecules have strong absorptions in the THz region. Measuring in reflection geometry from the silicon wafer liquid interface we do not have to consider the thickness of the sample and the reduction of the signal quality by strong absorption. In the THz-TDS system used here, the liquid is enclosed in a reservoir beneath a high resistivity silicon wafer. The spectral response of the Si-liquid interface is measured, which contains the dielectric constant information of the liquid sample.

3.2 Setup for THz time domain reflection spectroscopy

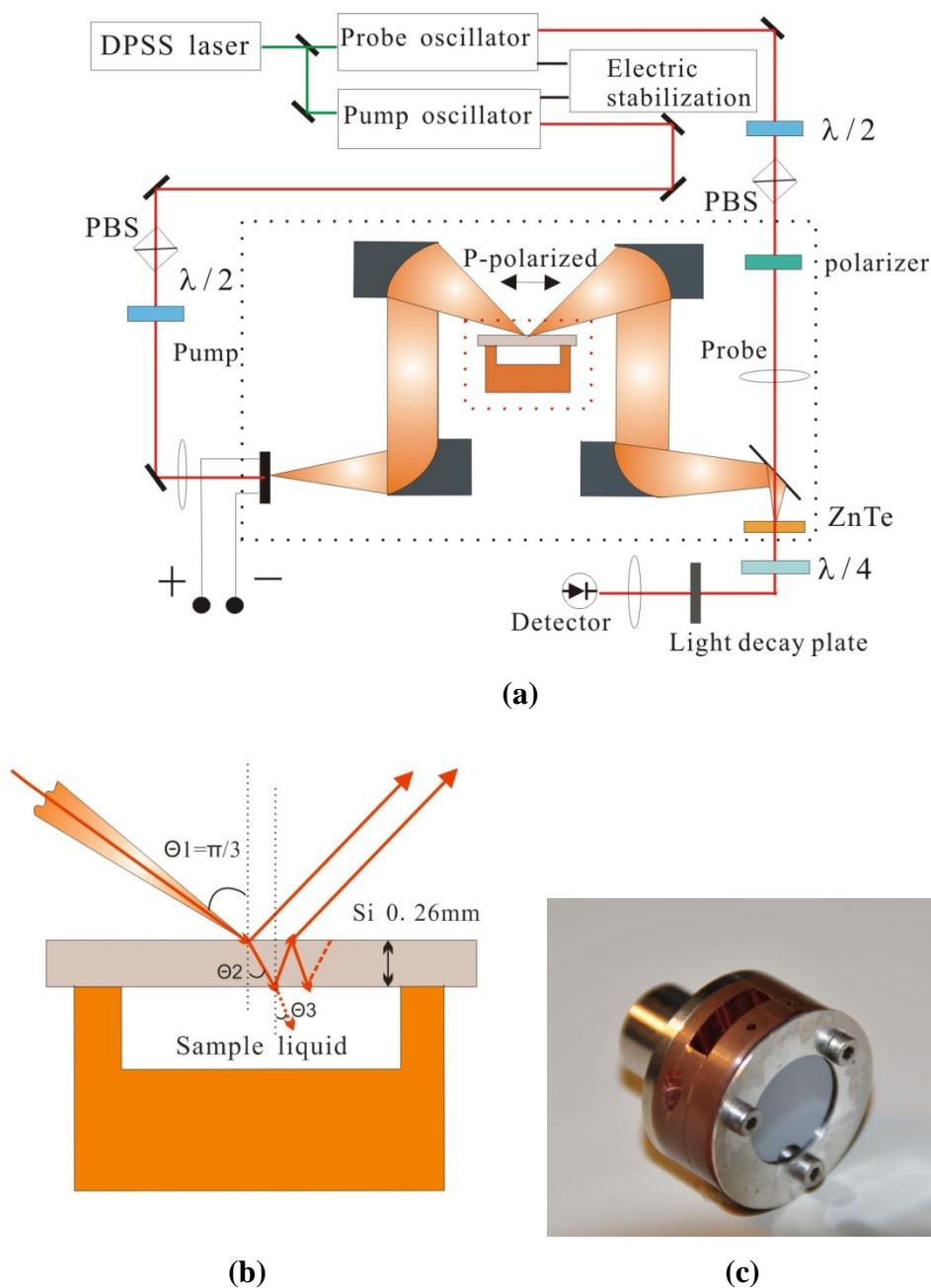


Figure 3.1: (a): Setup based on two separate Ti:sapphire fs lasers (pump and probe laser) pumped by a diode pumped solid state laser (DPSS) and the ASOPS technique. The rectangle area surrounded by black dots is purged with dry air. (b): detailed view (Rectangle area with red dots) of the sample holder and the THz beam path. (c): photo of the copper sample holder.

The experimental setup is depicted in Fig. 3.1. In order to perform experiments with good long-term stability and a high signal-to-noise ratio, our THz-TDS system employs high-speed asynchronous optical sampling (ASOPS). ASOPS uses two mode-locked femtosecond oscillators working at 1 GHz repetition rate with a fixed repetition frequency difference around 2 kHz as sources of pump and probe pulses, generating and detecting the THz pulses, respectively [Geb10], as has been described in detail in Section 2.4.

A copper sample holder was used which was equipped with a front window made of a double polished, highly resistive silicon wafer with a thickness of 260 μm . Two small holes were drilled on the side of the sample holder through which we can inject liquid solutions without any further mechanical changes to the set up. A heater and sensor can be placed in the holes providing controllable temperatures. THz pulses are generated from a large area photoconductive THz emitter [Dre05]. P-polarized THz pulses (this is achieved by positioning the emitter's interdigitated finger structure perpendicular to the optical table, or positioning a polarizer in the THz path) are focused on the silicon window of the sample cell with an incident angle around 60° . The THz pulse is partially reflected at the air-silicon interface, while a second reflection takes part at the silicon-liquid interface with a time delay of 6.2 ps corresponding to the optical thickness of the silicon wafer. All THz pulse paths are placed inside a box purged with dry air to eliminate the absorption by water in air. Both pulses can be clearly separated in time as can be seen in Fig. 3.2, in which the following echoes from the emitter and the silicon wafer have been omitted. The time traces of the THz pulse shown in Fig. 3.2 were taken with 500×1024 averages, each measurement took about 5 minutes. We use the pulse with no liquid filled in as a reference and the pulse measured with the liquid as the signal pulse. The second pulse contains the information about the complex dielectric constant of the liquid. Hence we can determine the complex dielectric constant of the liquid from the Fresnel reflection coefficients [Røn97].

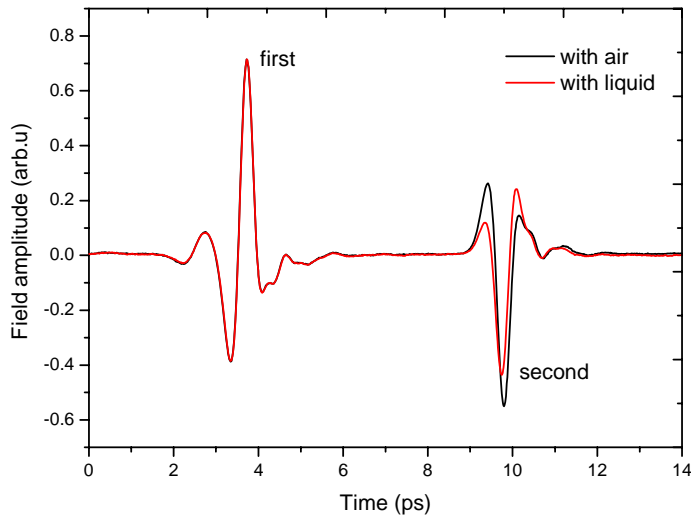


Fig 3.2: THz time traces with the first and second reflection of the THz pulse from the air-Si interface and Si-sample interface, respectively.

3.3 Data analysis

The data analysis in this section was partly based on the procedure described in [Røn97]. As shown in Fig. 3.1(b) for p-polarized THz pulses incident on the silicon wafer with an angle around 60° , suppose the Fourier transform of the THz pulse incident on the silicon wafer is $E_0(\omega)\exp(i\phi_0)$ with amplitude $E_0(\omega)$ and phase ϕ_0 , then the Fourier transform of the first reflection pulse can be expressed by

$$\hat{E}_1(\omega) = E_0(\omega)r_{a-si} \exp\left[i\left(\phi_0 + \frac{\omega}{c}n_a l_1\right)\right] \quad (3.3.1)$$

where r_{a-si} is the Fresnel coefficient for the reflection amplitude at the air-silicon interface, n_a is the refractive index of air for THz pulses and l_1 is the

propagation distance in air. The Fourier transform of the second reflection pulse is

$$\hat{E}_2(\omega) = E_0(\omega)t_{a-si}\hat{r}_{si-l}t_{si-a}\exp[i(\phi_0 + 2n_{si}d_{eff} + \frac{\omega}{c}n_a l_2)] \quad (3.3.2)$$

where t_{a-si} and t_{si-a} are the Fresnel coefficients for the transmission amplitude at the air-silicon and silicon-air interfaces, and \hat{r}_{si-l} for reflection at the silicon-liquid sample interface. n_{si} is the refractive index of the silicon wafer, and $d_{eff} = d_{si}/\cos\theta_2$ is the effective thickness of the silicon wafer (THz propagation distance in the silicon wafer). t_{a-si} , t_{si-a} and r_{a-si} are assumed to be real since the absorption of silicon and air are negligible. Spectra of the first and second reflection pulses are shown in Fig. 3.3.

Since the absolute values of the amplitude $E_0(\omega)$ and the original phase ϕ_0 as well as the additional phase $\frac{\omega}{c}n_a l$ are unknown, we use the ratio between $\hat{E}_1(\omega)$ and $\hat{E}_2(\omega)$ to eliminate these factors

$$\frac{\hat{E}_2(\omega)}{\hat{E}_1(\omega)} = \frac{t_{a-si}\hat{r}_{si-l}t_{si-a}}{r_{a-si}}\exp(i\frac{\omega n_{si} 2d_{eff}}{c}) \quad (3.3.3)$$

This function is known as the transfer function of the reflection THz-TDS system.

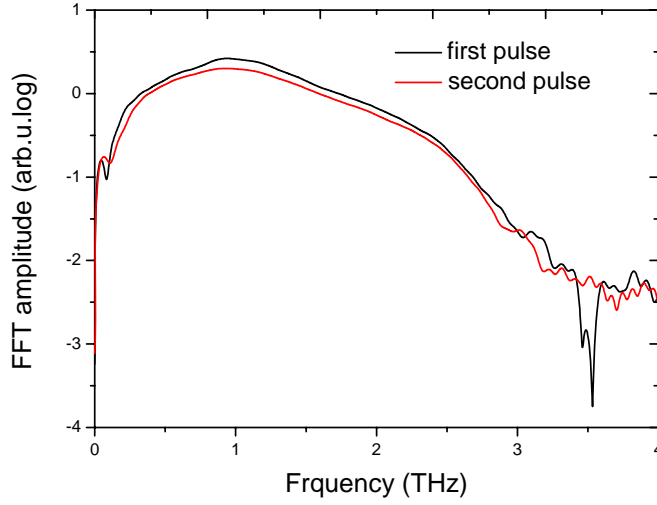


Figure 3.3: Spectra of the first and second pulse $\hat{E}_1(\omega)$, $\hat{E}_2(\omega)$.

3.3.1 Determination of the refractive index of silicon

The refractive index of the silicon wafer can be measured if we take a measurement without filling any liquid in the sample holder, the transfer function of the system in this case is

$$\frac{\hat{E}_2(\omega)}{\hat{E}_1(\omega)} = \frac{t_{a-si} r_{si-a} t_{si-a}}{r_{a-si}} \exp\left(i \frac{\omega n_{si} 2d_{eff}}{c}\right) \quad (3.3.4)$$

Therefore, the ratio between the Fourier transforms of the pulse reflected from the air-silicon interface $\hat{E}_1(\omega)$ and the pulse from the silicon-air interface $\hat{E}_2(\omega)$ can be determined from the Fresnel coefficients for the reflection and transmission amplitudes. In this case all the Fresnel coefficients are real. The Fresnel coefficients for the p-polarized reflection amplitudes are

$$r_{a-si} = \frac{n_{si} \cos \theta_1 - n_a \cos \theta_2}{n_{si} \cos \theta_1 + n_a \cos \theta_2}, \quad r_{si-a} = \frac{n_a \cos \theta_2 - n_{si} \cos \theta_1}{n_a \cos \theta_2 + n_{si} \cos \theta_1}$$

The Fresnel coefficients for the p-polarized transmission amplitudes are

$$t_{a-si} = \frac{2n_a \cos \theta_1}{n_a \cos \theta_2 + n_{si} \cos \theta_1}, \quad t_{si-a} = \frac{2n_{si} \cos \theta_2}{n_{si} \cos \theta_1 + n_a \cos \theta_2} \quad (3.3.5)$$

here θ_1 and θ_2 are as shown in Fig. 3.1 (b). The ratio of Fresnel coefficients

for the reflection amplitudes is $r_{si-a} / r_{a-si} = -1 = e^{i\pi}$. Suppose $\frac{\hat{E}_2(\omega)}{\hat{E}_1(\omega)} = R_E e^{i\theta_E}$,

then we can deduce the refractive index of silicon from the phase part

$$n_{si} = \frac{(\theta_E - \pi)c}{4\pi d_{eff} \nu} \quad (3.3.6)$$

or from the amplitude part

$$n_{si} = \frac{2 - R_E + 2\sqrt{1 - R_E}}{R_E} n_a \frac{\cos \theta_2}{\cos \theta_1} \quad (3.3.7)$$

Combining with Snell's law, $n_a \sin \theta_1 = n_{si} \sin \theta_2$, both the refractive index of silicon and the effective thickness of the silicon wafer can be obtained in a single measurement. Figure 3.4 shows the refractive index of the silicon wafer calculated from the phase part. We obtain a refractive index of $n_{si} = 3.425 \pm 0.02$ between 0.5 THz and 3 THz in good agreement with the literature [Røn97]. This measurement demonstrates the capability of the setup for quantitative and stable measurements.

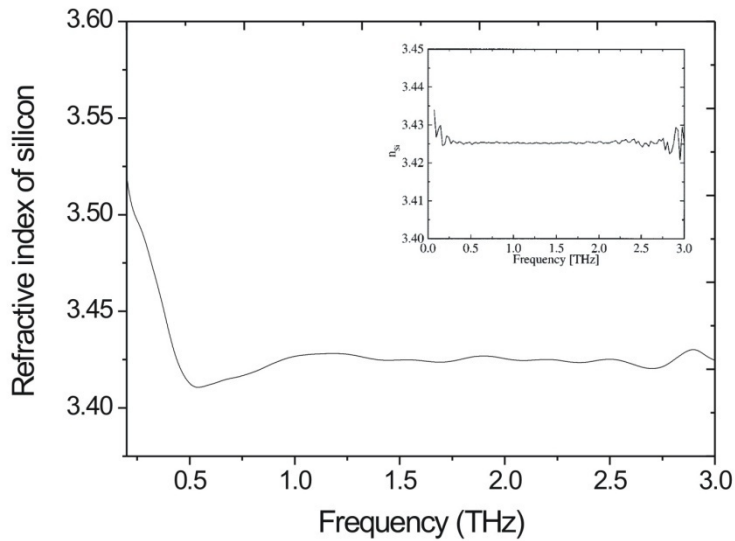


Figure 3.4: Refractive index of silicon wafer calculated from the phase part using a wafer thickness of 260 μm . (For comparison, inset is the result from Ref. [Røn97])

3.3.2 Determination of the complex dielectric constant of liquid samples.

Since we already know the refractive index and the effective thickness of the silicon wafer, in principle, the refractive index of the liquid sample can be determined in a single measurement using the transfer function (3.3.3). However, the calculation from the transfer function requires one to have very detailed knowledge of the phase propagation in the silicon wafer. The reflection pulse from the Si-liquid interface is spatially displaced in regard to the pulse from the air-Si interface as shown in Fig. 3.1 (b). The phase jumps and errors during the calculation for the ratio of the pulses' Fourier transforms make the determination of the refractive index of the liquid difficult. However, this problem can be overcome by taking a calibration measurement before the sample is measured. This calibration measurement was taken without any liquid filling as mentioned in above section. This method is based on the work in Ref. [Mer06].

For the calibration measurement, we rewrite the transfer function (3.3.4) as

$$\frac{\hat{E}_2(\omega)}{\hat{E}_1(\omega)} = A_{cal} \exp(i\phi_{cal}) = \frac{t_{a-si} r_{si-a} t_{si-a}}{r_{a-si}} \exp\left(i \frac{\omega n_{si} 2d_{eff}}{c}\right) A_{cor}(i\phi_{cor}) \quad (3.3.8)$$

Here we use $A_{cal} \exp(i\phi_{cal})$ to represent the amplitude and phase of the ratio of the Fourier transforms of the pulses. We bring in the complex correction factor $A_{cor}(i\phi_{cor})$ which summarizes the errors caused by the displacement of the pulses and the phase propagation. However, this term can be cancelled during the following calculation. Note that all the Fresnel coefficients in Eqs. (3.3.4) and (3.3.8) are real, since the absorption of THz radiation in silicon and air is negligible.

The transfer function for measurements with liquid sample is

$$\frac{\hat{E}_{2-sample}}{\hat{E}_1(\omega)} = A_{sample} \exp i(\phi_{sample}) = \frac{t_{a-si} \hat{r}_{si-l} t_{si-a}}{r_{a-si}} \exp\left(i \frac{\omega n_{si} 2d_{eff}}{c}\right) A_{cor}(i\phi_{cor}) \quad (3.3.9)$$

Here again we use $A_{sample} \exp i(\phi_{sample})$ to represent the amplitude and phase of the ratio of the Fourier transforms of the pulses. The correction factor is the same as in Eq. (3.3.8). The Fresnel reflection coefficient \hat{r}_{si-l} at the Si-liquid interface is complex due to the THz absorption in the liquid sample. Many of the terms in the transfer function can be cancelled if we take the ratio of both sides of the Eqs. (3.3.9) and (3.3.8)

$$\frac{A_{sample}}{A_{cal}} \exp[i(\phi_{sample} - \phi_{cal})] = \frac{\hat{r}_{si-l}}{r_{si-a}} \quad (3.3.10)$$

Therefore the Fresnel reflection coefficient at the interface of Si-liquid can be expressed as

$$\hat{r}_{si-l} = \frac{A_{sample}}{A_{cal}} r_{si-a} \exp[i(\phi_{sample} - \phi_{cal})] \quad (3.3.11)$$

The Fresnel equation for reflection at this interface is given by

$$\hat{r}_{si-l} = \frac{n_{si} \cos \theta_3 - \hat{n}_l \cos \theta_2}{n_{si} \cos \theta_3 + \hat{n}_l \cos \theta_2} \quad (3.3.12)$$

where $\hat{n}_l = n_l + i \frac{\alpha_l c}{4\pi\nu}$ is the complex refractive index of the liquid sample. If

we express the reflection coefficient in the Euler representation $\hat{r}_{si-l} = \text{Re}^{i\theta}$ and solve Eq. (3.3.12) for the unknown refractive index n_l of the liquid, we obtain

$$n_l = \frac{n_{si} \cos \theta_3 (1 - R^2)}{(1 + R^2 + 2R \cos \theta_1) \cos \theta_2} = B \cos \theta_3, \quad \text{with } B = \frac{n_{si} (1 - R^2)}{(1 + R^2 + 2R \cos \theta_1) \cos \theta_2} \quad (3.3.13)$$

Combining with Snell's law, $n_a \sin \theta_1 = n_{si} \sin \theta_2 = n_l \sin \theta_3$, the refractive index can be further expressed as

$$n_l = B * \cos\left(\frac{1}{2} \arcsin(2 \sin \theta_1) / B\right), \quad \text{with } B = \frac{n_{si} (1 - R^2)}{(1 + R^2 + 2R \cos \theta_1) \cos \theta_2} \quad (3.3.14)$$

The power absorption coefficient of the liquid sample can also be obtained by solving Eq. (3.3.12), which is

$$\alpha_l = \frac{2\omega n_{si} \cos \theta_3}{c \cos \theta_2} \frac{-2R \sin \theta}{1 + R^2 + 2R \cos \theta_1} \quad (3.3.15)$$

Furthermore, the complex dielectric constant $\hat{\epsilon} = \epsilon_1 + i\epsilon_2$ can be calculated from the relation $\hat{\epsilon} = \hat{n}^2$. The real and imaginary parts of the complex dielectric constant are

$$\epsilon_1 = n_l^2 - \left(\frac{\alpha_l c}{4\pi\nu}\right)^2 \quad \text{and} \quad \epsilon_2 = \frac{n_l \alpha_l c}{2\pi\nu} \quad (3.3.16)$$

respectively.

3.4 Properties of water

Water molecules are one of the most abundant molecules in the universe. On our planet, more than 70% of the earth's surface is covered by water. Water was important since the formation of our planet. At that time water played a role as coolant as a by-product during the star formation. Water is a liquid at ambient conditions, but also exists in the solid state (ice) and the gaseous state (vapour or steam) on earth. The water cycle continually adjusts the climate, allowing for life on our planet. Today all known forms of life depend on water (for instance, the human body consists to about 70 % of water). It is no wonder people say 'water is the source of life'.

Ancient people have recognized the importance of water: it was considered as one of the main classical elements by the Chinese and many other nations in Europe. However, the knowledge of water was superficial until the development of modern science and technology.

A water molecule consists of one oxygen and two hydrogen atoms connected by covalent bonds, forming a H_2O . As shown in Fig. 3.5, the bonding angle of the two hydrogen atoms is around 104.45 degrees which causes it to be dipolar giving a positive and negative side accounting for its unique properties. Commonly, the hybridization of the oxygen atom in water is described as sp^3 (tetrahedral electron geometry) in which two OH bonds take up two of the hybridized electron pairs leaving two lone pairs that can take part in the formation of hydrogen bonds with adjacent molecules [Pet02]. The formation and breakup of hydrogen bonds between water molecules occurs very rapidly, which leads to continuous rearrangements of the molecules. These rearrangements are associated with water molecule reorientations, which occur on the picosecond (ps) time scale corresponding to the THz frequency region [Luz96, Sta99].

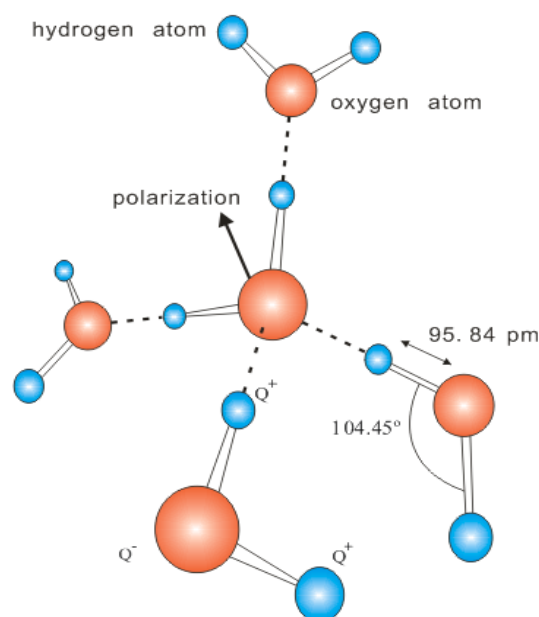


Figure 3.5: A water molecule surrounded by four hydrogen bonded water molecules. The angle of H-O-H bonds in a water molecule is about 104.5 degrees. The dipole moment and hydrogen bonds (dashed line) are due to the different partial charges Q^- and Q^+ on the oxygen atoms and hydrogen atoms.

From the viewpoint of a single water molecule, on very short time scales it will rotate freely [Bal94] similarly with the motion of gas molecule before collision with others. On a little longer time scales it will interact with adjacent molecules via formation of hydrogen bonds which is known as hindered translations or rotations. After the breakup of the hydrogen bonds, relaxation and diffusion of the molecule will occur [Bal94, Røn00].

We will discuss this in the following section, how water molecules will act under a temporally varying electric field.

3.4.1 Water molecule reorientations

As described in the last section, the water molecule has a dipole moment. When a weak static electric field is applied to water, the water molecules will

be aligned due to the field's force on the dipole moments of the water molecules; therefore, a polarization proportional to the electric field will be created. This procedure is known as molecular reorientation. This polarization has a dielectric contribution to the material equations according to the descriptions in Section 2.5. Replacing the static electric field with a weak, temporally varying electric field, a time dependent polarization will be created. Roughly speaking, if the electric field oscillates very slowly the dipoles of the water molecules are able to follow the electric field at all times, in this case the dielectric function of water is real and constant. If the electric field oscillates faster the dipoles are not able to keep up with the electric field and the lag between the polarization and the electric field will induce retardation and absorption, i.e. the dielectric function will be complex. If the electric field oscillates too fast (in the high frequency limit) to be followed by the dipoles, there will be no absorption again, i.e. the dielectric function will be real and constant [Bal94]. In addition, this assumption neglects the rotational motions of the dipoles, inter- and intramolecular hydrogen-bond stretching vibrations, etc.

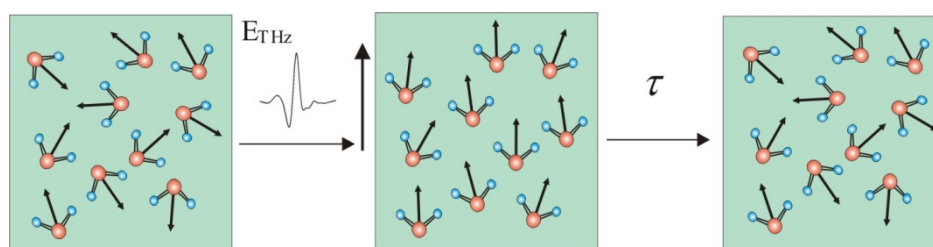


Figure 3.6: Water molecules under a temporally varying electric field.

Since the polarization is proportional to the electric field and has a dielectric response, it can be measured directly by changing the electric field amplitude. This is done by replacing the electric field with temporally varied THz pulses i.e. by terahertz time domain spectroscopy (THz-TDS). The water molecules' motions during THz-TDS are shown in Fig. 3.6. The water molecules 'dance' randomly before a THz pulse is applied to them. When the

THz pulse reaches them they are aligned due to the interaction between the field and their dipoles. When the THz pulse has passed over, after a period of time τ (around 8 ps) the molecules recover to the randomly ‘dancing’ state. The time τ needed for molecules to go from alignment to the original ‘dancing’ state (or from the randomly dancing state to the alignment state) is called relaxation time.

It is worthy to note that the polarization of the water molecule dipoles is wave vector k dependent, what we measured in this work is the component perpendicular to the wave vector (transverse). For probing the longitudinal component, other probing methods will be needed [Røn00]. Therefore, the dielectric function we depict in this thesis of work is the transverse dielectric function. However, we will use the name dielectric function for short in the following.

3.4.2 Modelling the dielectric function of water

Although the water molecules’ motions are rather complicated, only the molecular motions described above give rise to the time dependent polarization and will contribute to the dielectric function.

The most widely accepted model to describe the complex frequency-dependent dielectric function $\hat{\epsilon}$ of polar liquids is the Debye model and extensions of the Debye model [Jep07, Jep10, Kin96, Koe07, Mer06, Møl09, Nag06, Røn97, Røn99, Røn00, Røn02, Tie09, Yad08, Yad09]. Here I will give a derivation of the Debye model of dielectric relaxation. This derivation is largely based on references [Hil69, Hil85, Møl09].

Considering the dielectric displacement $\vec{D} = \epsilon_0 \epsilon_r \vec{E}$ of the dielectric material, if an electric field $\vec{E}(u)$ is applied to the dielectric material in the time interval from u to $u + du$, the total displacement \vec{D} will comprise two

contributions: the nearly instantaneous electronic response $\vec{D}_1(u) = \varepsilon_0 \varepsilon_r(\infty) \vec{E}(u)$ where $\varepsilon_r(\infty)$ is the high frequency limit of the real dielectric constant and the slower dipolar response \vec{D}_2 which will still exist at $t > u + du$ due to the inertia of the dipoles. If several pulsed electric fields are applied to the material at different times the total dipolar response will be the superposition of the field-induced displacements with a decay $\alpha(t-u)$. Suppose the applied electric field is a continuously varying field from the time $u = 0$, the total dielectric displacement will be the sum:

$$\vec{D}(t) = \varepsilon_0 \varepsilon_r(\infty) \vec{E}(t) + \varepsilon_0 \int_0^t \vec{E}(u) \alpha(t-u) du \quad (3.4.1)$$

where the decay function $\alpha(t-u)$ depicts the displacement decay with time after the electric field is removed. Obviously $\alpha(t-u)$ will tend to 0 if the time t tends to infinite.

Suppose the applied electric field is periodic, $\vec{E}(t) = E_0 \exp(i\omega t)$, and lasts long enough to insure the decay function $\alpha(t-u) \rightarrow 0$, then the total displacement will also vary periodically,

$$\vec{D}(t) = D_0 \exp(i\omega t) = \varepsilon_0 E_0 (\varepsilon_{r1} \cos \omega t + \varepsilon_{r2} \sin \omega t) \quad (3.4.2)$$

By changing the variable quantity u to $x = t - u$, Eq. (3.4.1) can be rewritten as

$$\vec{D}(t) = \varepsilon_0 E_0 \cos(\omega t) [\varepsilon_r(\infty) + \int_0^\infty \alpha(x) \cos \omega x dx] + \varepsilon_0 E_0 \sin(\omega t) \int_0^\infty \alpha(x) \sin \omega x dx \quad (3.4.3)$$

Therefore we can obtain the relative dielectric constant with

$$\varepsilon_{r1} = \varepsilon_r(\infty) + \int_0^\infty \alpha(x) \cos \omega x dx, \text{ and } \varepsilon_{r2} = \int_0^\infty \alpha(x) \sin \omega x dx \quad (3.4.4)$$

respectively. Furthermore the dielectric constant can be rewritten as

$$\varepsilon_r(\omega) = \varepsilon_r(\infty) + \int_0^\infty \alpha(x) \exp(-i\omega x) dx \quad (3.4.5)$$

For dipole molecules, the relaxation process from alignment to the unordered state can be depicted with $\exp(-t/\tau)$ where τ is the relaxation time. Therefore, the decay function can be rewritten as

$$\alpha(t) = \frac{\varepsilon_r(0) - \varepsilon_r(\infty)}{\tau} \exp(-t/\tau) \quad (3.4.6)$$

where $\varepsilon_r(0)$ is the low-frequency limit of the dielectric constant describing the response of a medium to static electric fields. Substituting Eq. (3.4.6) into Eq. (3.4.5) we can obtain

$$\varepsilon_r(\omega) = \varepsilon_{r1} + i\varepsilon_{r2} = \varepsilon_r(\infty) + \frac{\varepsilon_r(0) - \varepsilon_r(\infty)}{1 + i\omega\tau} \quad (3.4.7)$$

This is the basic Debye dielectric relaxation model. From the derivation of this equation it can be seen that, if several relaxation processes take place in parallel with different relaxation times, the total dielectric function will be a sum of the individual contributions from each process.

For water molecules, the reorientation of molecular dipoles exhibits two relaxation processes and hence the dielectric function can be given by

$$\tilde{\varepsilon}(\omega) = \varepsilon_\infty + \frac{\varepsilon_s - \varepsilon_1}{1 + i\omega\tau_D} + \frac{\varepsilon_1 - \varepsilon_\infty}{1 + i\omega\tau_2} \quad (3.4.8)$$

Here we substitute ε_r by ε , $\varepsilon_r(0)$ by ε_s and $\varepsilon_r(\infty)$ by ε_∞ . Summarizing the description of this model: ε_∞ is the high-frequency limit of the complex permittivity, ε_s is also called the static permittivity in the low-frequency limit of permittivity describing the response of a medium to static electric fields, τ_D and $\varepsilon_s - \varepsilon_1$ are the relaxation time and the strength of the rotational Debye relaxator, respectively, and τ_2 and $\varepsilon_1 - \varepsilon_\infty$ are those of the second

Debye relaxator. Furthermore, vibrational modes (intermolecular and intramolecular) will also give contributions to the dielectric function at higher frequencies [Møl09, Nag06], and many researchers have extended the Debye model to more than two relaxators. However, in this thesis the high frequency range relaxations can be neglected. The Debye model with two relaxation processes is based on the assumption that these relaxation processes are independent of each other and take place in parallel.

3.5 Ions in water

Water is an excellent solvent due to its polar character. Many kinds of acids, alkalis, and salts can be dissolved in water forming electrolytes which typically contain free ions. The most abundant electrolyte on our planet is seawater, which contains many kinds of solutes, such as Na^+ , K^+ , Ca^{2+} , Mg^{2+} , Sr^+ and so on for cations, and Cl^- , SO_4^- , Br^- , HCO_3^- (CO_3^{2-}), F^- and so on for anions. Besides this, there are many more systems where ions interact with water and play a role, for example, biological fluids which can transmit signals and control the cell volume. However, the understanding of ionic solutions on a molecular level is still incomplete.

Compared to pure water, ions in water solution can provide electrical conductivity and cause a rearrangement in the hydrogen bond network which makes intermolecular interactions much more complicated. Charged ions can induce electric fields which will reorient the dipoles of the surrounding water molecules, hence the charge will be screened and the long-range interaction between cations and anions is reduced [Swa07].

Protons (H^+) play different roles compared to regular positive ions, since water contains protons itself. A proton can form a covalent bond with a water molecule, forming a hydronium ion H_3O^+ , while the regular positive ions do not (only negative ions can form a hydrogen bond with a surrounding water molecule). It was revealed by de Grotthuss in 1806 that hydronium (H_3O^+)

can also form covalent and hydrogen bonds (H-bonds) with adjacent molecules, through which protonic charge can be transferred via a rearrangement of the covalent and hydrogen bonds [Gro1806]. This is the reason why the conductivity of protons in water is much larger than through other ions under similar conditions [Swa07, Tie10a].

In dilute solutions cations and anions are relatively isolated in a “cage” formed by surrounding water molecules [Sch09]. However, at high concentrations, hydronium and chloride ions can also be connected by interaction via hydrogen bonds [Bot04, Lee96, Tri75].

3.5.1 Damped, driven harmonic oscillator model

Compared with pure water, the dielectric function of ionic solutions is much more complicated. As shown in Fig. 3.7, in dilute solutions, electric fields induced by charged ions will reorient the dipoles of the surrounding water molecules, i.e. depolarization takes place, hence the charge will be screened. However, adjacent anions and cations which share the same hydration shell will also contribute to a dipole (which is not shown in Fig. 3.7 as limited by the picture size). The ions combining with surrounding water molecules can also form dipoles under an electric field. Therefore, to analyse the dielectric function of ionic solutions we have to consider three respective contributions from bulk water, solutes (anions and cations) and water molecules in the dynamic hydration shell which share distinct fast network dynamics. The third component was added because of the observation of a nonlinear response when increasing the concentration [Hey08].

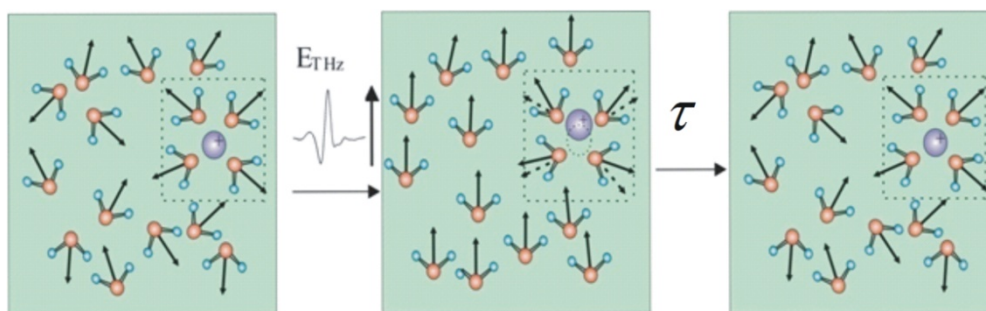


Figure 3.7: Water based solution under a temporally varying electric field (only one cation is shown).

Previous measurements in Ref. [Sch09] showed a linear dependence of the THz absorption on salt when increasing the concentration, which indicates that the THz absorption coefficients of the solvation shells are approximately equal to those of bulk water, and/or that the dynamic hydration shell is very small, suggesting that the ions can be treated as simple defects in an H-bond network. Schmidt et al. explained the salt concentration-dependent THz absorption with a model of ionic rattling motions, i.e., oscillations of the anions and cations, which are driven by the THz field in “cages” provided by the surrounding water molecules [Sch09]. We will use this model to analyse our measurement results, therefore I will give a detailed introduction to this model in the following pages.

In this model a single ion is described as a damped driven harmonic oscillator with a function [Dod95]

$$m \frac{\partial^2 x}{\partial t^2} + m\gamma \frac{\partial x}{\partial t} + kx = eE(t) \exp(-i\omega t) \quad (3.4.9)$$

where x is the displacement of the ion, while m is the mass of ion, and k is the force constant describing the strength of confinement of the ion due to the interaction with the surrounding water molecules. γ is the damping constant of the ion oscillation in the potential well which is formed by the water molecules interacting with the radiation field [Fox01], and ω is the angular frequency of the incident radiation field $E(t)$. This model is based

on the assumption that at the sub-ps timescale the network of water molecules surrounding each ion is essentially unchanged and therefore can be treated as a potential-well confining the oscillatory motions of ions. This assumption is reasonable since the breakup and reformation of hydrogen bond occurs on a timescale of picoseconds.

By solving Eq. (3.4.9) we obtain a solution describing the oscillator with

$$x(t) = \frac{e}{m} \frac{1}{\omega_0^2 - \omega^2 - i\omega\gamma} E(t) \quad \text{where } \omega_0^2 = \frac{k}{m} . \quad (3.4.10)$$

The polarization contribution of the ions is $P_i(t) = eNx(t)$, where e and N are the electric charge and density of ions, respectively. The dielectric contribution of ions can be easily calculated with

$$\varepsilon_i(\omega) = \frac{P_i(t)}{\varepsilon_0 E(t)} = \frac{Ne^2}{\varepsilon_0 m} \frac{1}{\omega_0^2 - \omega^2 - i\omega\gamma} \quad (3.4.11)$$

To study the concentration dependence of the dielectric function of the ionic solutions, we convert the density N to the concentration C_s together with Avogadro's number N_A . We also convert the mass of ion to a reduced mass $\mu_i = (m_i * s_i)/(m_i + s_i)$ with a reduced-mass fitting parameter s_i as did in Ref. [Sch09]. Therefore, the concentration dependent contribution to the dielectric constant of the ions is

$$\varepsilon_i(\omega) = \left[\frac{10^3 N_A e^2}{\varepsilon_0} \frac{\mu_i \omega^2 - k_i + i\mu_i \omega \gamma_i}{(\mu_i \omega^2 - k_i)^2 + \mu_i^2 \omega^2 \gamma_i^2} \right] \times C_s \quad (3.4.12)$$

Here again k_i is the force constant (in kg/s^2) describing the strength of confinement of the ions due to the interaction with the surrounding water molecules, and γ_i is the damping constant of the oscillations in the solvation cavity, C_s is the salt concentration (in mol/l). The term in square brackets on the right hand side of Eq. (3.4.12) gives the molar dielectric constant contribution σ_{ei} of the ions.

3.5.2 Modelling the dielectric function of ionic solutions

As described in the last section, the total dielectric constant of the solution should be composed of contributions from bulk water (water molecules in the dynamical hydration shell are also included as their contributions are approximately equal to those of bulk water) and solute (ions of anions and cations). Therefore in our model the linear superposition of the dielectric contributions from bulk water, the anions and cations are:

$$\varepsilon(\omega, C_s) = \sigma_{water}(\omega)C_{water}(C_s) + \sigma_c(\omega)C_s + \sigma_a(\omega)C_s + \frac{\sigma_{ic}C_s}{i\omega\varepsilon_0} \quad (3.4.13)$$

where $\sigma_{water}(\omega)$ is the molar dielectric constant cross section of pure water at a given temperature and $\sigma_{c,a}(\omega)$ are the molar dielectric constant cross sections of cations and anions, respectively. σ_{ic} is the ion induced electric conductivity. C_{water} is the concentration of water which is correlated with C_s and defined in terms of partial molar volumes [Hor72]. In order to calculate the water concentration in solution we use the Masson equation $\phi_V = \phi_{v,s}^0 + \sqrt{C_s}S_{v,s}^*$ given in Ref. [Hor72] which describes the concentration dependent partial molar volume ϕ_V of a salt in solution. Here $\phi_{v,s}^0$ is the ions' apparent molar volume at infinite dilution, and $S_{v,s}^*$ is the experimental slope of the Masson equation. The water concentration in solution is given by

$$C_{water} = (W_{mc} - \frac{(\phi_{v,s}^0 + \sqrt{C_s}S_{v,s}^*)}{V_{w0}}C_s) \quad (3.4.14)$$

where W_{mc} is the water concentration in pure water at room temperature and V_{w0} is the molar volume of pure water. Therefore combined with the Debye model the dielectric contributions from bulk water can be described by

$$\varepsilon_{water} = \left(1 - \frac{C_s}{W_{mc}} \frac{(\phi_{v,s}^0 + \sqrt{C_s} S_{v,s}^*)}{V_{w0}}\right) \left(\varepsilon_\infty + \frac{\varepsilon_s - \varepsilon_1}{1 + i\omega\tau_D} + \frac{\varepsilon_1 - \varepsilon_\infty}{1 + i\omega\tau_2}\right) \quad (3.4.15)$$

The total dielectric constant of the solution therefore can be written as

$$\begin{aligned} \tilde{\varepsilon}(\omega) = & \left(1 - \frac{C_s}{W_{mc}} \frac{(\phi_{v,s}^0 + \sqrt{C_s} S_{v,s}^*)}{V_{w0}}\right) \left(\varepsilon_\infty + \frac{\varepsilon_s - \varepsilon_1}{1 + i\omega\tau_D} + \frac{\varepsilon_1 - \varepsilon_\infty}{1 + i\omega\tau_2}\right) + \frac{\sigma_{ic} C_s}{i\omega\varepsilon_0} + \sigma_{ec}(\omega) C_s \\ & + \sigma_{ea}(\omega) C_s \end{aligned} \quad (3.4.16)$$

with $\sigma_{ei} = \frac{10^3 N_A e^2}{\varepsilon_0} \frac{\mu_i \omega^2 - k_i + i\mu_i \omega \gamma_i}{(\mu_i \omega^2 - k_i)^2 + \mu_i^2 \omega^2 \gamma_i^2}$, the molar dielectric constant contribution from the ions given in Eq. (3.4.12).

We will use Eq. (3.4.16) to explain the measurement results of solutions in this thesis.

3.6 Experimental results and analysis

Using the THz-TDS setup described in Section 3.2, we measured bulk water at different temperatures. Using HCl and NaCl solutions with different concentrations we studied the changes of the dielectric response introduced by the ions. We found a linear increase of the real and imaginary part of the dielectric function compared with pure water with increasing ion concentrations. The concentration dependence of the dielectric function and corresponding differences between each other can be explained by our extended model. As a supplement, some organic liquids were also measured for comparison.

3.6.1 Liquid water

Employing the setup described in Section 3.2, we measured the complex dielectric function of H₂O as a function of temperature in the frequency range from 0.15 THz to 2.5 THz. These measurements were performed with 60° incidence with distilled liquid water at three different temperatures between 297 K and 357 K with a step of 30 K. Each measurement was performed with 512000 averages.

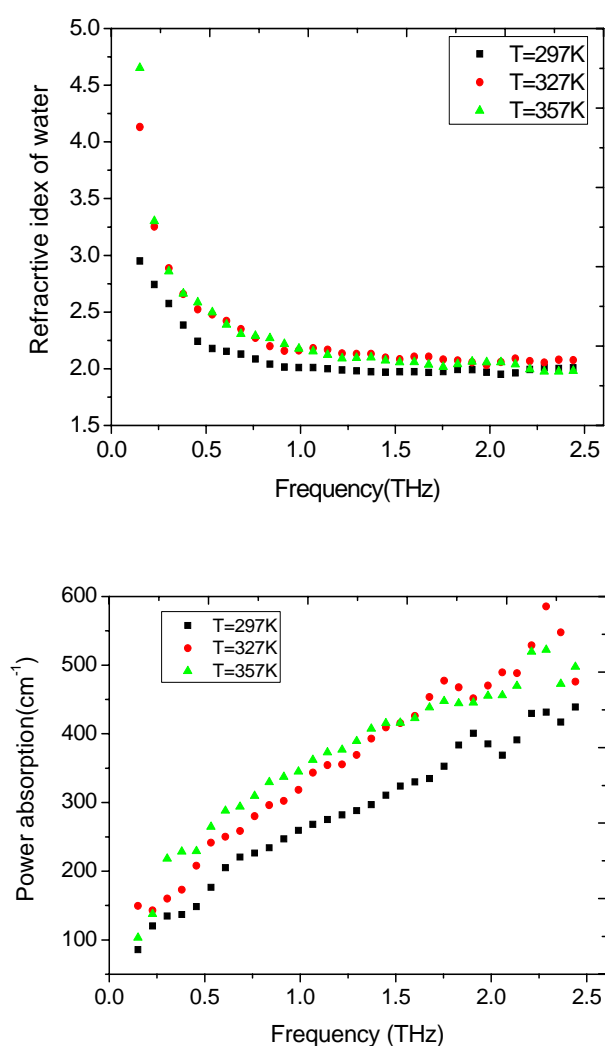


Figure 3.8: The refractive index and power absorption of H₂O shown as a frequency dependent function at three different temperatures.

Figure 3.8 shows the frequency dependent refractive index and power absorption of H₂O obtained at three different temperatures. For the measurement results at different temperatures, the general tendency is that the refractive index increases with increasing temperature but decreases with increasing frequency. The absorption also increases with increasing temperature but increases with increasing frequency as well. At low frequencies (around 0.7 THz) the refractive index increases with increasing temperature much stronger than at high frequencies (around 2 THz). The highest absorption coefficient obtained is around 500 cm⁻¹, which corresponds to a penetration depth of about 20 μm, insuring that the results observed are those of bulk water rather than surface effects.

The complex dielectric function was calculated for data analysis. The real and imaginary parts of the dielectric function at different temperatures are shown in Fig. 3.9. As the temperature increases from 297 K to 327 K, we can see an apparent increase of the dielectric constant from Fig. 3.9 and also that of the refractive index and power absorption from Fig. 3.8. However, at the higher temperature of 357 K, we cannot see the apparent increase of the dielectric constant; as previous studies show [Røn97, Røn00], this is because of the thermal expansion of the copper holder, which changes the position of the focused THz beam path on the silicon wafer at higher temperatures and influences the results in complicated ways. Therefore, we will concentrate on room temperature measurements in the following.

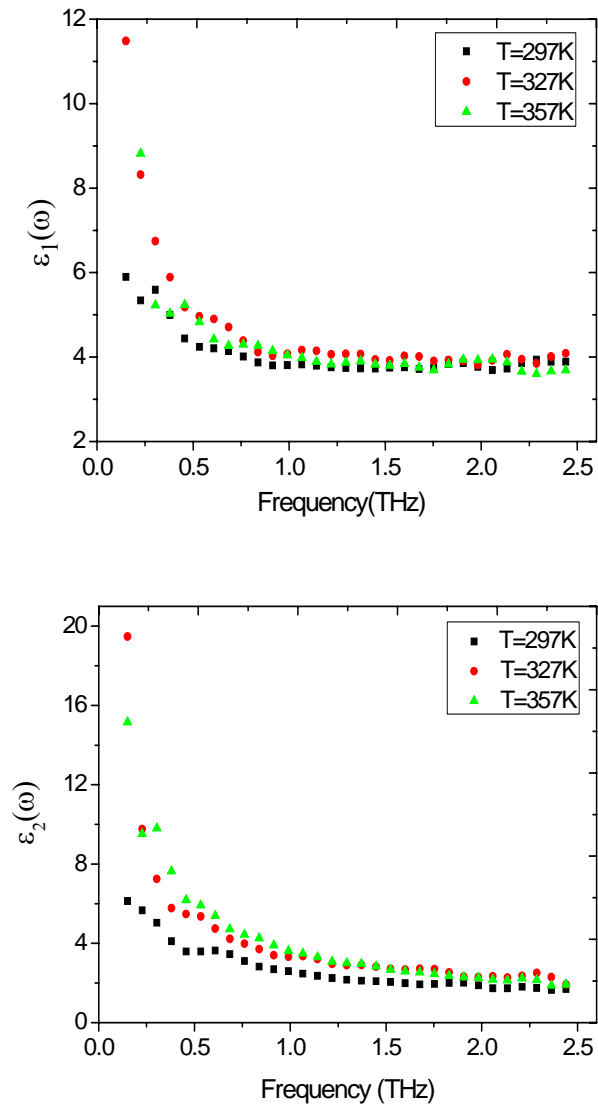


Figure 3.9: Complex dielectric constant of H₂O at different temperatures; $\epsilon_1(\omega)$ is the real part of the dielectric function while $\epsilon_2(\omega)$ is the imaginary part.

The commonly used model to fit and analyze the dielectric function of water is the Debye model as described in Section 3.4.2, which is comprised of two relaxation processes [Jep10, Møl09, Røn97, Røn99, Røn00, Røn02, Tie09]

$$\tilde{\varepsilon}(\omega) = \varepsilon_{\infty} + \frac{\varepsilon_s - \varepsilon_1}{1 + i\omega\tau_D} + \frac{\varepsilon_1 - \varepsilon_{\infty}}{1 + i\omega\tau_2} \quad (3.6.1)$$

where ε_{∞} is the high-frequency limit of the complex permittivity, ε_s is the low-frequency limit of the permittivity describing the response of a medium to static electric fields, τ_D and $\varepsilon_s - \varepsilon_1$ are the relaxation time and the strength of the rotational Debye relaxator, respectively, and τ_2 and $\varepsilon_1 - \varepsilon_{\infty}$ are those of the second Debye relaxator.

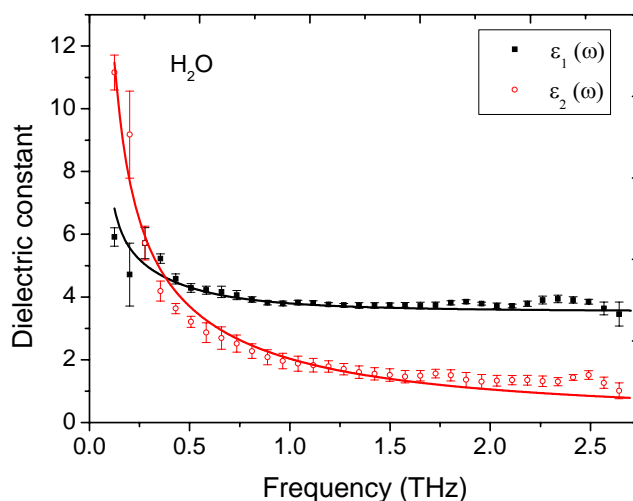


Figure 3.10: Complex dielectric constant of H₂O with error bars at room temperature fitted with Debye model (the full line); $\varepsilon_1(\omega)$ is the real part of dielectric constant while $\varepsilon_2(\omega)$ is the imaginary part.

The measured complex constant together with the fitted Debye model is shown in Fig. 3.10. To clarify the stability of our system we also show the error bars. These error bars are the standard deviations. The uncertainty of the measurements was caused by the fluctuations of the laser power and the temperature variation. The fitted parameters for the Debye model are shown in table 1. The dielectric constants of bulk water in our measurements are 10% smaller than the results from Rønne et al. [Røn97], but are in quite good

agreement with results from Masaya et al. [Nag06] and even much earlier results from Afsar et al. [Afs77]. Using this model to fit the dielectric constant of our results, the slow and fast relaxation times τ_D and τ_2 are 8.2 ps and 0.39 ps, respectively, which are slightly different from Masaya's work, in which their parameters are 9.36 ps and 0.30 ps. The high-frequency limit ϵ_∞ in our simulation is 3.53 which is higher than their value of 2.5 [Nag06] but consistent with Jepsen et al. [Jep07].

Table 1: Fit parameters for Debye model, errors are given in brackets.

Fitting parameters	
ϵ_∞	3.53 (0.2)
ϵ_s	80.3 (2)
ϵ_1	5.2 (0.1)
τ_D (ps)	8.2 (0.3)
τ_2 (ps)	0.39 (0.05)

The goal of studying the dielectric function of water is to obtain a microscopic understanding of the mechanisms behind the observed dielectric response. Using the double Debye model to analyze the dielectric relaxation of water, the relaxation times obtained describe the relaxations of the macroscopic polarizations of the water molecules. Rønne et al. have studied the temperature dependence and the isotope shift of relaxation times in the Debye model to investigate the local structure and microscopic dynamics of water molecules [Røn97, Røn99, Røn00]. Computer simulations of molecular dynamics (MD) for water molecules also found a correlation time of longer than 2 ps which is qualitatively in agreement with the slow relaxation time in the Debye model, additionally a fast process was also observed in the simulations [Neu86].

Concerning the two relaxation processes, the time scale of the fast process is in agreement with single molecule rotation, for which a rotation time of about 100 fs was calculated [Røn00, Bar72]. For slow Debye relaxation, previous studies indicate that a structural rearrangement of water molecules is involved. Agmon suggested that the elementary mechanism behind the Debye relaxation time relies on a ‘tetrahedral displacement’, the translation of a water molecule from an occupied to an unoccupied corner of the cube bounding the $(\text{H}_2\text{O})_5$ tetrahedron [Agm96]. Bakker et al. suggested that water molecules with weaker hydrogen bonds having small activation energies lead to a larger freedom to change their orientations (giving a fast relaxation time), while molecules with stronger hydrogen bonds having high activation energy can only change orientations if the hydrogen bonds are temporarily stretched (giving a slow relaxation time) [Nie00].

However, the true story of the complex interactions in liquid water is still vague as there are an incomprehensibly large number of microscopic degrees of freedom. To fully understand the microscopic dynamics of liquid water more experimental and theoretical studies are needed, but there is no doubt that THz-TDS can be an attractive and important method to increase the knowledge of water.

3.6.2 Dielectric relaxation of HCl and NaCl water solutions

We have used Terahertz time-domain spectroscopy (THz-TDS) to investigate the complex dielectric function of water solutions containing different ions. Using HCl and NaCl solutions with different concentrations we study the changes of the dielectric response introduced by the ions. We find a linear increase of the real and imaginary part of the dielectric function compared with pure water with increasing ion concentrations. We use an expanded model for fitting the dielectric function based on a combination of a Debye relation and damped harmonic oscillators for the anions and cations. A good agreement between the model and the experimental results is obtained. Parts

of the results are published in Ref. [Qia12].

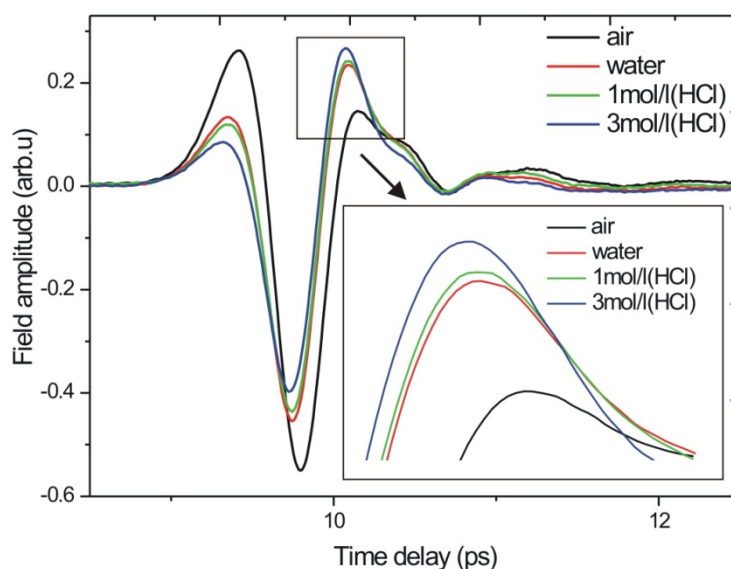


Figure.3.11: Terahertz pulses (second pulse) reflected by an empty vessel and by vessel filled with pure water as well as 1 mol/l, 3 mol/l HCl water solutions.

We performed a series of measurements of solutions with different concentrations varying from pure water to 3 mol/l at room temperature. Each measurement was repeated four times with 512000 averages. The results shown in the following are the average values of the four measurements. As a typical measurement, we show in Fig. 3.11 the reflected THz pulses from an empty vessel and from vessels filled with pure water as well as 1 mol/l and 3 mol/l HCl solutions. We can clearly see the pulse shape changing with concentration in the time domain. The refractive index and the absorption coefficient in the range from 0.2 THz to 2.7 THz are obtained quantitatively from these measurements. In Fig. 3.12 (a) and (b) the refractive index and the absorption for different concentrations of the HCl-water solutions are shown. The concentration was increased in steps of 0.5 mol/l. Clearly both the refractive index and the absorption coefficient of the HCl solutions have a

gradual and monotonic increase with higher concentrations in the whole THz region.

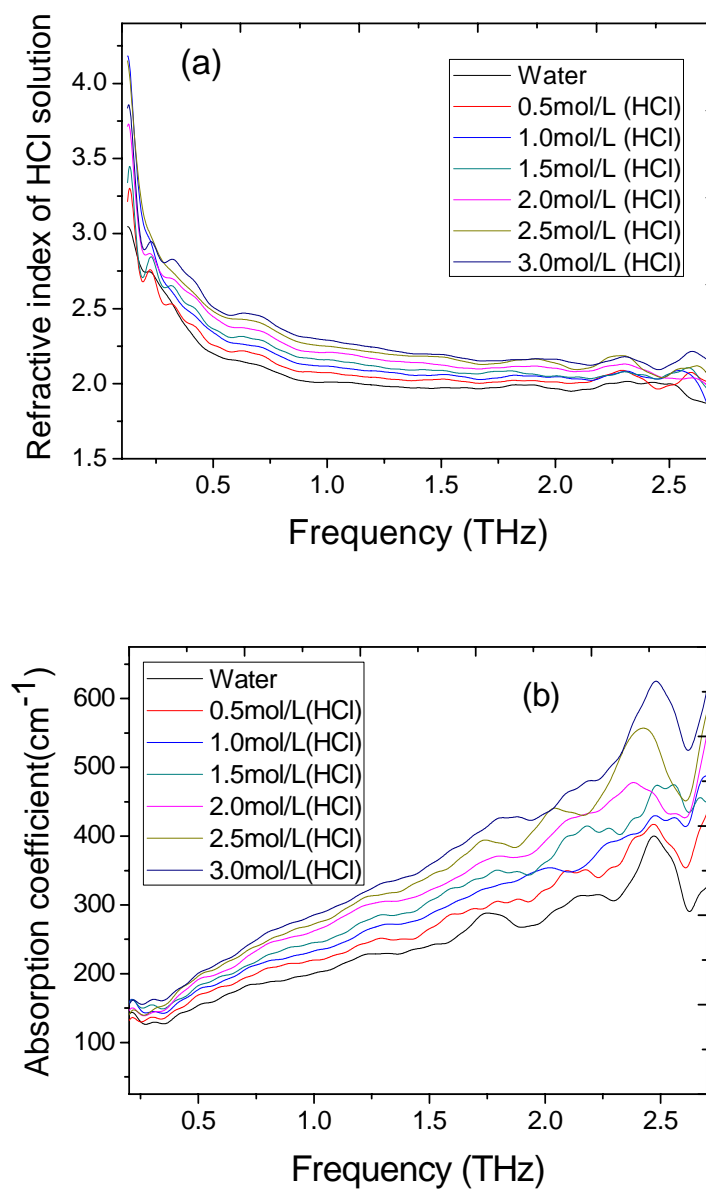


Figure.3.12: (a) Refractive index of HCl solutions with different concentrations from 0.5 to 3 mol/l. (b) Absorption coefficient of HCl solutions with different concentrations from 0.5 to 3mol/l.

The complex dielectric function $\varepsilon(\omega,c)=\varepsilon_1(\omega,c)+i\varepsilon_2(\omega,c)$ of HCl solutions as a function of concentration and frequency are shown in Fig. 3.13. Similar to pure water, the real and imaginary parts of the dielectric function decrease

with frequency. For increasing ion concentrations they both increase. There are several oscillatory structures and dips on the spectra shown in Fig. 3.12 and Fig. 3.13 as deviations from a smooth curve. These stem primarily from the Fourier transforms in the data evaluation and an increased noise level at low (< 500 GHz) and high (> 2 THz) frequencies. However, these deviations from a smooth curve do not have a physical origin and do not influence the trends of the main spectral features.

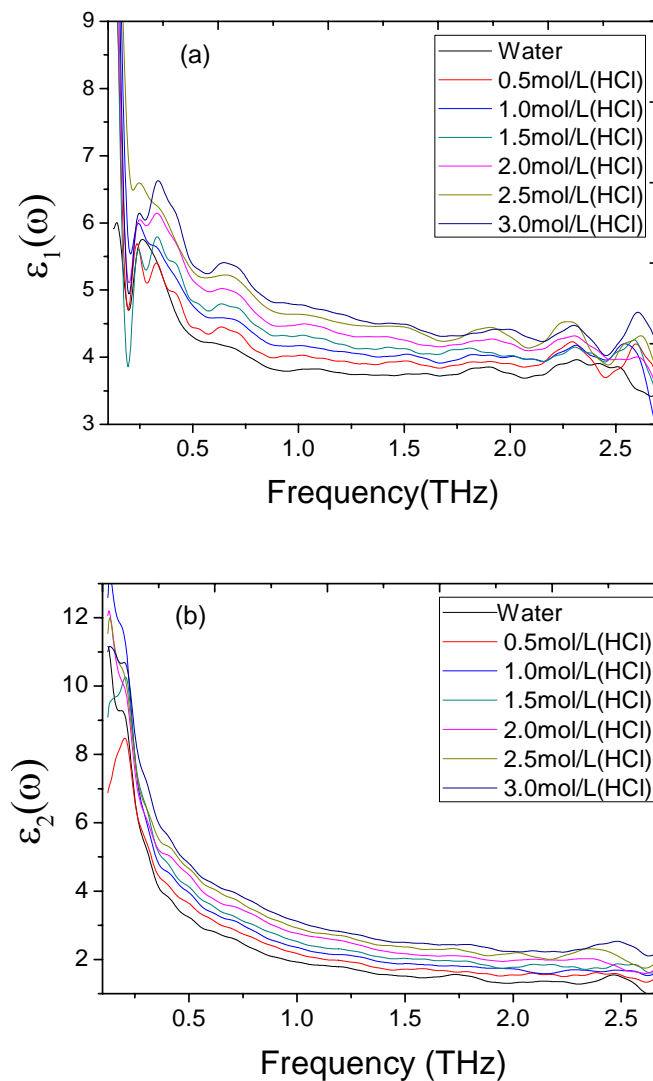


Figure.3.13: (a) The real part of the complex dielectric function $\epsilon_1(\omega, c)$ shown as a function of frequency for different concentrations of HCl. (b) The imaginary part of the complex dielectric function $\epsilon_2(\omega, c)$ for different concentrations.

The complex dielectric function of NaCl solutions shows a gradual increase similar to the HCl solutions concerning the dependence on concentration. As the tendency of the dielectric constant with concentration is almost consistent in the whole frequency range, we choose the data at 1 THz in order to compare the results. Fig. 3.14 shows the real and imaginary part of the dielectric function at the frequency of 1 THz. Both the HCl and NaCl solutions show a linear increase with increasing concentrations. This behaviour is consistent with the results from Tielrooij et al. [Tie09].

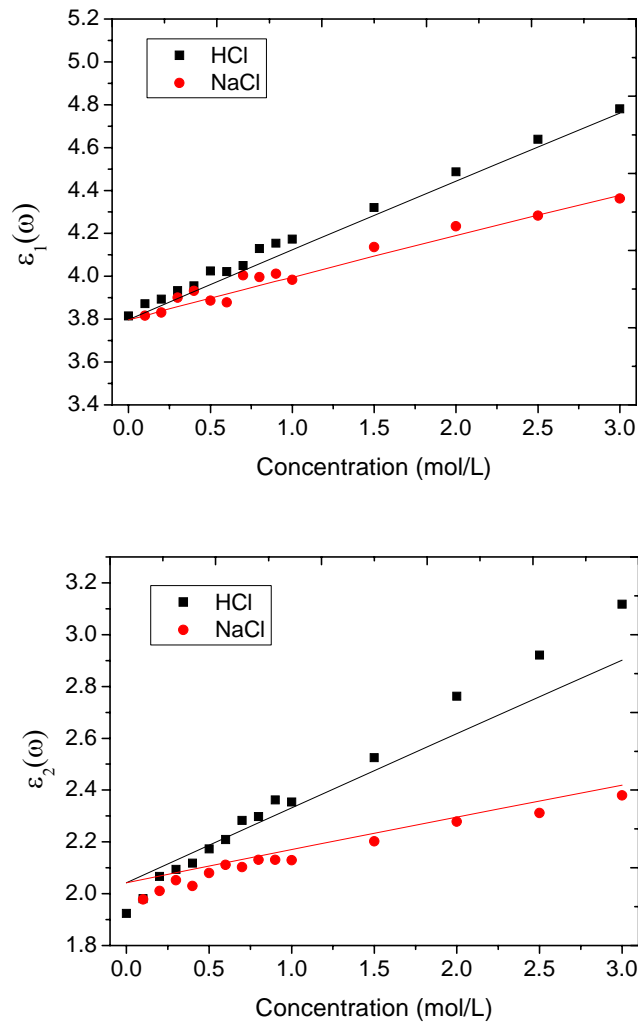


Figure.3.14: (a), (b) Dependence of real and imaginary part of dielectric constant of HCl and NaCl solutions, respectively, with concentration at 1 THz, with data measured (points) and theoretical fits (solid lines).

The experimental data reveal that the dielectric function of solutions shows the same frequency dependence as bulk water and a gradual and monotonic increase for increasing concentrations as seen in Fig. 3.13 and Fig. 3.14. We assume that the dielectric response of the water molecules is independent of the ion concentrations in dilute solution. To simulate the experimental data, we used a model based on the following assumptions: the frequency dependent molar dielectric function cross sections σ_{ec} and σ_{ea} of cations and anions, respectively, are described by a reduced-mass resonance which describes the anions and cations as damped harmonic oscillators (for details see Section 3.5.2). Therefore the obtained total dielectric function is a linear superposition of the individual contributions

$$\begin{aligned} \tilde{\varepsilon}(\omega) = & \left(1 - \frac{C_s}{W_{mc}} \frac{(\phi_{v,s}^0 + \sqrt{C_s} S_{v,s}^*)}{V_{w0}}\right) \left(\varepsilon_\infty + \frac{\varepsilon_s - \varepsilon_1}{1 + i\omega\tau_D} + \frac{\varepsilon_1 - \varepsilon_\infty}{1 + i\omega\tau_2}\right) + \frac{\sigma_{ic} C_s}{i\omega\varepsilon_0} + \sigma_{ec}(\omega) C_s \\ & + \sigma_{ea}(\omega) C_s \end{aligned} \quad (3.6.2)$$

The first term of Eq. (3.6.2) is the dielectric contribution of bulk water to the solutions while the second term is the ion induced electric conductivity and the third and fourth terms are contributions from cations and anions, respectively.

Besides the double Debye model included in this model, we used five adjustable parameters to fit the frequency dependent molar dielectric constant cross section which are all shown in Table 2. We are aware of the fact that this large number of fitting parameters opens a large parameter space for fitting the experimental data. However, we believe that the model as a combination of two known description reflects well the complex dynamics.

Table 2: Fit parameters for reduced-mass resonance and the dielectric function of ionic solutions.

Fitting parameters	HCl	NaCl
W_{mc} (mole/liter)	55.51	55.51
m_a (amu)	35.45	35.45
m_c (amu)	19.02	22.99
$\phi_{v,s}^0$ (cm ³ /mole)	17.8	16.62
$S_{v,s}^*$ (cm ³ liter ^{1/2} mole ^{-3/2})	1.884	1.884
V_{w0} (cm ³ /mole)	18.02	18.02
σ_{ic} (literHz/mole)	19.4±0.3	4.3
γ_A (THz)	15.46	15.46 [Sch09]
k_A (kg/s ²)	7.3	7.3
γ_C (THz)	10.62	10.62 [Sch09]
k_C (kg/s ²)	10.6±0.2	63.08 [Sch09]
s_c (g/mol)	40.12	40.12 [Sch09]

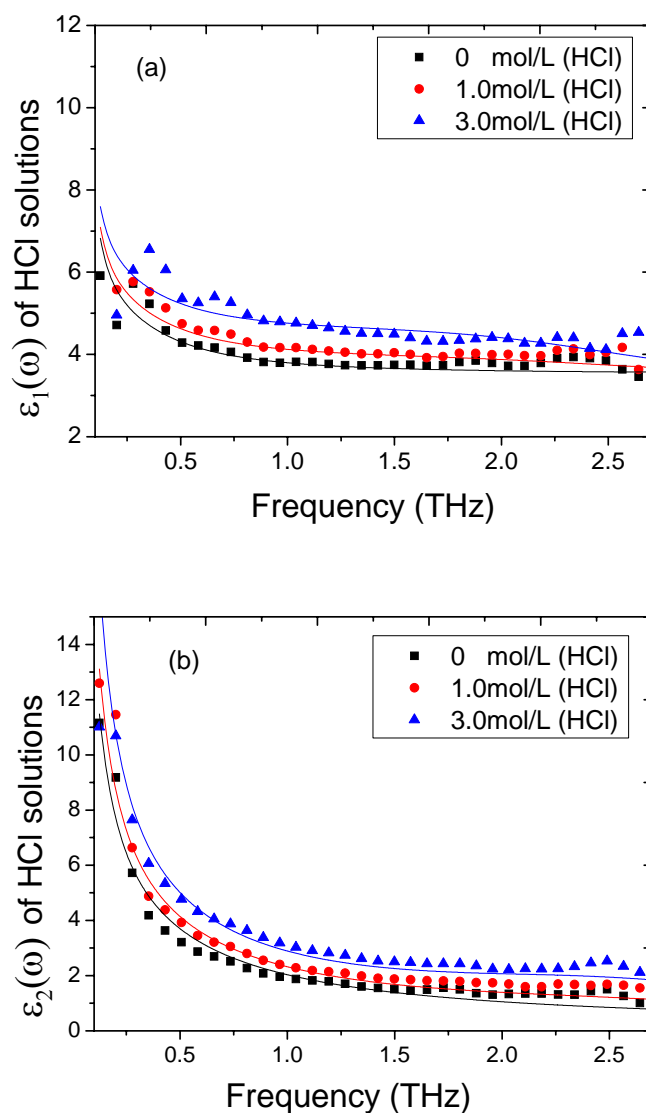


Figure.3.15: (a), (b) real and imaginary part of dielectric constant of HCl solutions with different concentrations, with data measured (points) and theoretical fits (solid lines).

Figure.3.15 and Fig.3.16 show the theoretical calculations together with the measured complex dielectric functions of HCl and NaCl solutions. Both figures show a good agreement between the measured results and the model.

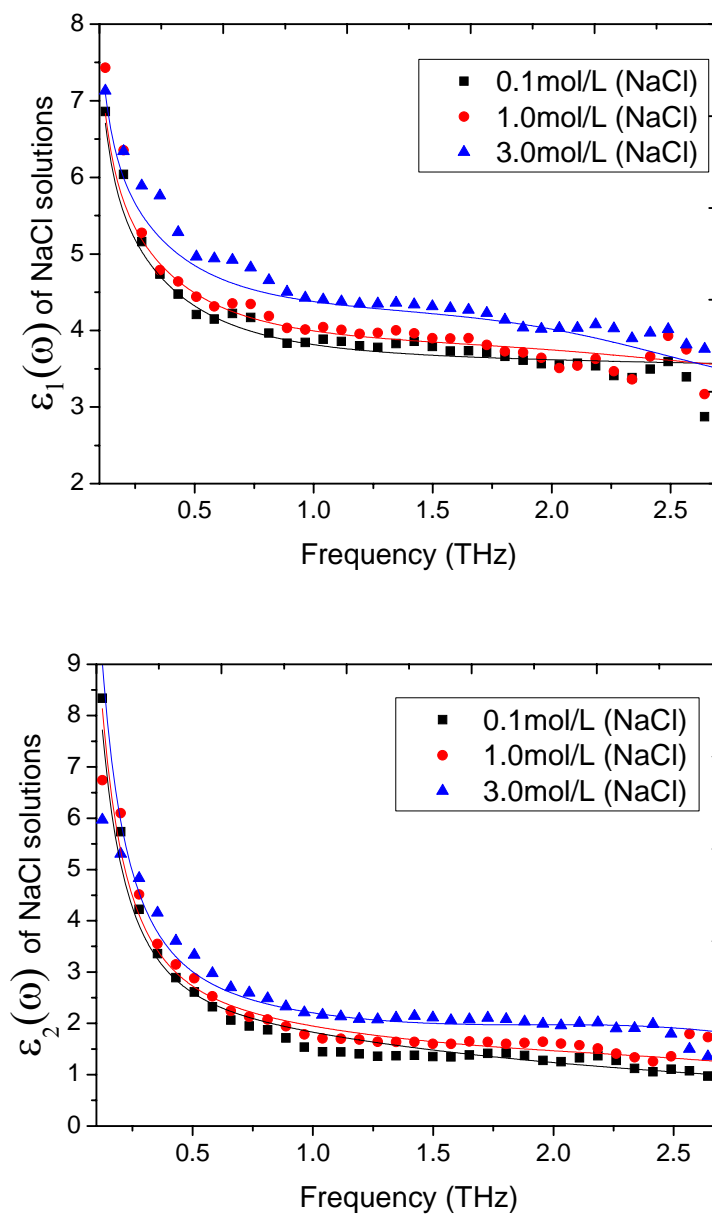


Figure.3.16: (a), (b) real and imaginary part of dielectric constant of NaCl solutions with differing concentrations, with data measured (points) and theoretical fits (solid lines).

Jepsen et al. and Tielrooij et al. have used the double Debye model to analyze the complex dielectric relaxations of ion solutions [Jep10, Tie09, Tie10b]. In their analysis, they determine the ions' effects to be a change in

the relaxation strength $\varepsilon_s - \varepsilon_1$ and the relaxation time τ_D . They suggested that although the dynamics of water molecules are predominantly unaffected by the presence of ions (bulk-like water), water molecules in hydration shells are affected. The presence of ions leads to a lowering of relaxation strength and change of relaxation time τ_D because: 1. the water concentration in solution is lower than in pure water. 2. The electric field induced by charged ions keeps the water molecules in the vicinity from participating in the relaxation process with τ_D . 3. The ions' motions in the water network lead to reorientation of molecules in a direction opposite to the driving field. These explanations are very reasonable; however, it is an improper generalization to conclude that all these effects influence only two parameters. Using the double Debye model to fit the dielectric function of solutions by changing the parameters seems like a mathematical trick. In addition, the double Debye model neglects the effects of dipoles induced by ions in the surrounding molecules under an external driving field.

Therefore, our expanded model which is based on the combination of the double Debye model and damped harmonic oscillators seems reasonable and attractive, since the lowering of the bulk water concentration by ions (including the solvation shell's water molecules [Sch09]) and ion (cation and anion) induced dielectric contributions are all included, respectively [Qia12].

In order to study the contributions of the different parts of Eq. (3.6.2) to the complex dielectric constant of the solution, we plot the different contributions in Fig. 3.17. Comparing each contribution to the complex dielectric function by the chloride, hydronium and sodium ions, the chloride ions have a 10 times higher contribution than the sodium ions to the real part of the dielectric function, and 100 times higher for the imaginary part, respectively. This means that in NaCl solution the increase of the dielectric constant is mainly caused by the contributions from chloride ions. The

contribution of hydroniums is on the same scale as the contribution from the chloride ions. This is expected because of the much stronger interactions with surrounding water molecules.

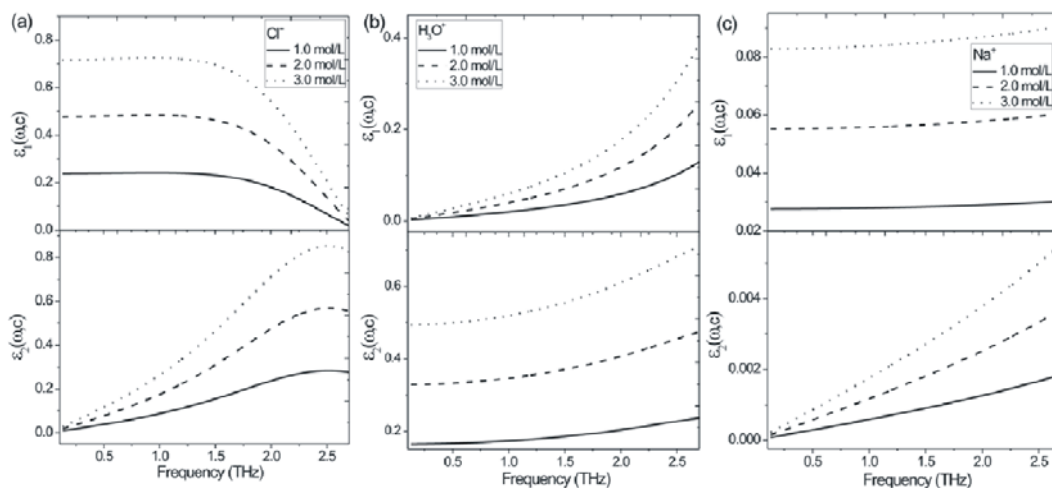


Figure.3.17: (a), (b) and (c) are contributions to the complex dielectric function from chloride ions, hydroniums, and sodium ions in corresponding solutions, respectively.

In the NaCl solution, anions and cations can certainly be described as damped harmonic oscillators in the cage, as they do affect the dynamics of the hydrogen bonds of surrounding water molecules to a lesser extent [Sch09]. However, circumstances are different in the HCl solutions. As we see from Fig. 3.14 for the same concentration of NaCl and HCl solutions, the dielectric constants of NaCl are apparently smaller than those of HCl; this is partly because the volume of Na⁺ in solution is much larger than that of H⁺, which lowers its own bulk water concentration in solution. Another reason is that the proton (H⁺) can form a covalent bond with a water molecule, forming hydronium (H₃O⁺), which can also form hydrogen bonds with surrounding water molecules and reorient the dipoles of water molecules further due to the induced electric field. Hydronium ions can directly behave as dipoles and also contribute in the same way as ions like Na⁺ do. These affect the relaxation of water molecules much more strongly and also

contribute to the higher value of the dielectric function of HCl solution than that of NaCl with the same concentration. It is assumed that the protonic charge is transferred from the hydronium to the surrounding molecules by rearrangement of covalent and hydrogen bonds, thus resulting in an σ_{ic} of HCl solutions much higher than the σ_{ic} of NaCl solution for the same concentration [Tie09, Swa07].

Although the hydronium changes the hydrogen bond network, it is assumed that the effect on the surrounding water molecules gets weaker at increased distance. Hydrogen bonds are formed and broken on picosecond time scales in the water network, hence the configuration of water molecules around the hydronium is assumed to remain constant. Therefore we can still treat the system as damped harmonic oscillators. The relevant arrangement of protons in water solution is still under debate: It has been proposed that the most relevant configuration is either as hydronium (H_3O^+) as Zundel cation ($H_5O_2^+$) or Eigen cation ($H_9O_4^+$) or even larger clusters [Tie09, Swa07]. In our model of damped harmonic oscillators we used the hydronium configuration. The force constant k_C of hydronium due to the interaction with surrounding water molecules is quite different from that of sodium ions due to the difference of the covalent and hydrogen bonds. The main parameters for fitting the model to the experimental data are the mass, the force constant k_C and the electrical conductivity σ_{ic} . Best results are obtained by setting the hydronium mass $m_c=19.02$, and force constant $k_C=10.6$, and the electrical conductivity $\sigma_{ic}=19.4$ for HCl.

Summarizing our experimental results in this section and the theoretic analysis, we conclude that for acid and salt water solutions, the THz complex dielectric constant can be described as a linear superposition of contributions of bulk water and ionic oscillations in a water cage defined by the solvating water as well as induced electrical conductivity. A linear increase of the

dielectric function compared with pure water with increasing ion concentrations is verified by both the experimental and theoretical analysis. Within this model hydroniums can also be described as damped harmonic oscillators with compensated fitting parameters although they are associated with more complex dynamics compared to other positive ions.

3.6.3 Other liquids measured by THz-TDS reflection spectroscopy

In this section, I will show some results from some organic liquids measured by using our THz-TDS setup. The samples of organic liquids are propanol, glycerol, and triethylene glycol, respectively. The structures of each single molecule are shown in Fig. 3.18 in which the water molecule structure is also included for comparison.

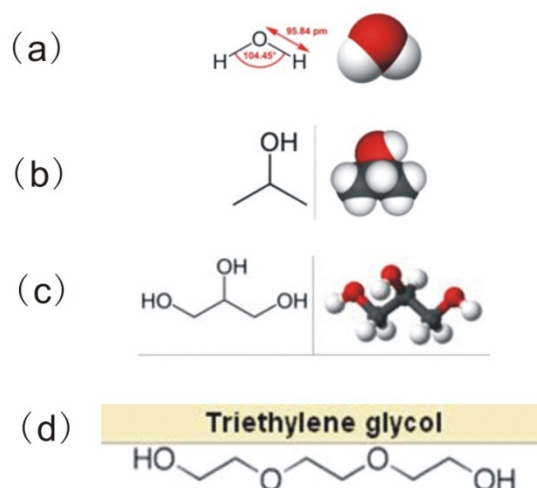


Figure.3.18: Molecular structures of water (a), propanol (b), glycerol (c), and triethylene glycol (d), respectively.

From the molecular structures of the molecules we can see that the volumes of the sample molecules have the relation: water < propanol < glycerol < triethylene glycol. Both water and triethylene glycol molecules have two hydroxyls, while propanol molecule has only one hydroxyl and glycerol molecule has three hydroxyls, respectively.

Figure 3.19 shows the refractive index and power absorption of the samples; water has the highest refractive index and power absorption while

propanol has the lowest among the four samples. For the refractive index, glycerol has a decreasing tendency upon increasing frequency as water but with a weaker behaviour, while propanol and triethylene glycol apparently do not show any frequency dependence. For the power absorption, all samples have increasing tendencies upon increasing frequency, however in the low frequency from 0.2 THz to 0.7 THz, the values of organic liquids are almost the same.

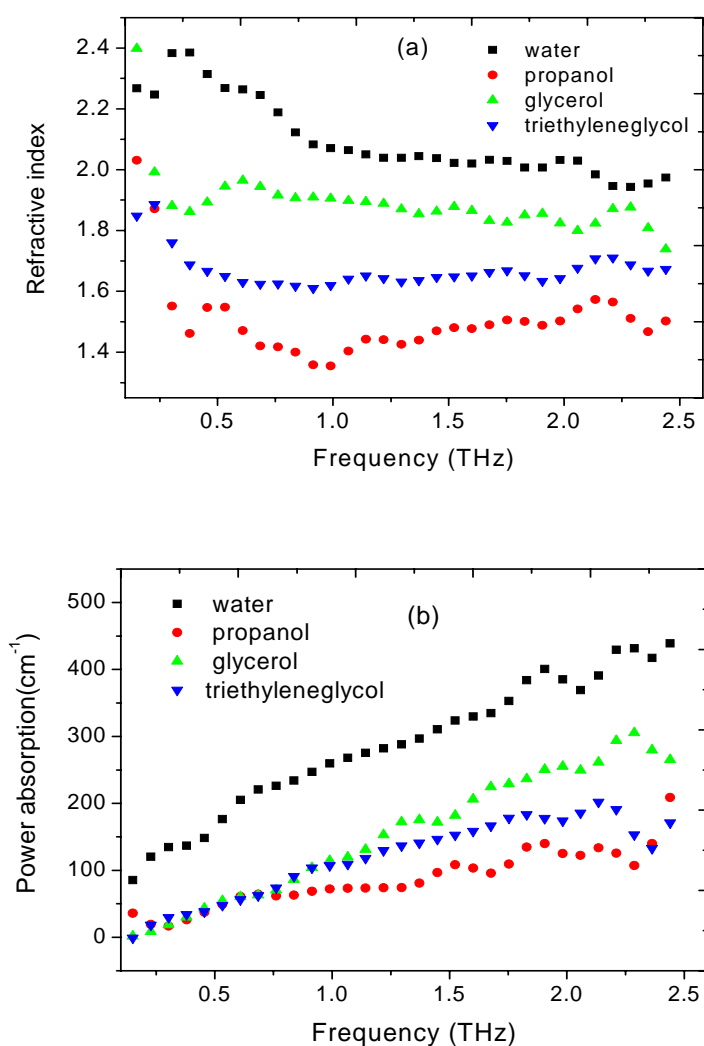


Figure 3.19: (a) Refractive index of water, propanol, glycerol, and triethylene glycol. (b) Absorption coefficient of water, propanol, glycerol, and triethylene glycol.

Figure 3.20 shows the real and imaginary parts of the complex dielectric function of the four samples.

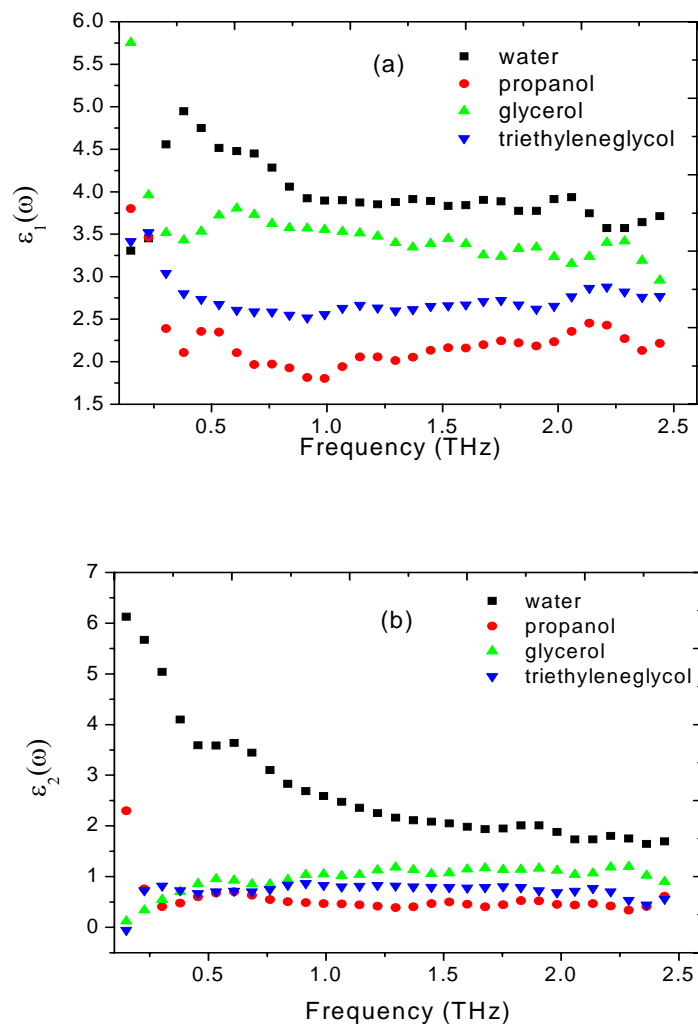


Figure.3.20: (a), (b) real and imaginary part of dielectric constant of water, propanol, glycerol, and triethylene glycol.

The differences in the experimental data reveals that the dielectric functions of the organic liquids are strongly dependent on the concentration of hydroxyls. If we consider the molecular structure of the samples, water has the highest hydroxyl concentration, that of glycerol is also high but lower than that of water. If only considering the molecular formulas of propanol and triethylene glycol, propanol seems to have a little higher hydroxyl

concentration than the latter, however, as the volume of the propanol molecule is much smaller than the latter, the intermolecular forces will provide a distance between molecules, which will lower the concentration of hydroxyls and furthermore result in an inverse result (see Fig. 3.20). In the low frequency domain (from 0.2 THz to 0.7 THz) the absorptions are predominantly caused by the torsion, bending, and stretching of the molecules, therefore the three organic samples show no apparent difference. However, in the higher frequency area, the absorption are predominantly caused by the hydrogen bond motions, therefore the hydroxyl concentration becomes important.

I found that the Debye model cannot precisely fit the measured complex dielectric function. To fit these functions other extra models or a refined Debye model will be needed, however we will not discuss this in this work.

3.7 Conclusion

In this chapter we presented THz time domain reflection spectroscopy of aqueous system. Data analysis based on this setup was also given. The Debye model and damped harmonic oscillator model were carefully introduced and applied for the analysis of the dielectric relaxation of water and water based solutions. We have performed measurements of water and water based HCl and NaCl solutions with different concentrations at room temperature in the range from 0.1 THz to 2.7 THz using this setup. The theoretical analysis using the Debye model and the extended model are in good agreement with the complex dielectric constant of water and water based ions solutions. A linear increase of the dielectric function compared with pure water with increasing ionic concentrations was verified by both the experimental and theoretical analysis. As a supplement, we showed some organic liquids measured with this setup. We found that the dielectric functions of the organic liquids are strongly dependent on the concentration of hydroxyls (see above).

Chapter 4 THz time domain parallel-plate waveguide spectrometer

In this chapter, a compact high-resolution THz time-domain waveguide spectrometer that is operated inside a cryostat is demonstrated. Theory of electromagnetic waves propagating in a parallel plate waveguide will be also introduced. In the setup a THz photo-Dember emitter and a ZnTe electro-optic detection crystal are directly attached to a parallel copper-plate waveguide. This allows the THz beam to be excited and detected entirely inside the cryostat, obviating the need for THz-transparent windows or external THz mirrors. Since no external bias for the emitter is required, no electric feed-through into the cryostat is necessary. Using asynchronous optical sampling, high resolution THz spectra are obtained in the frequency range from 0.2 to 2.0 THz. The THz emission from the photo-Dember emitter and the absorption spectrum of 1, 2-dicyanobenzene film are measured as a function of temperature. An absorption peak around 750 GHz of 1, 2-dicyanobenzene displays a blue shift with increasing temperature.

4.1 General introduction

A waveguide is a device used to guide waves (such as electromagnetic waves or sound waves) from one region to another without significant loss in intensity by confining them to propagate in one dimension. There are many different types of waveguide structures for each type of waves. The most common type for radio waves and microwaves (low frequency) is a hollow conductive metal pipe while for light (high frequency) it is an optical fibre. Basically, different waveguides are needed for different frequencies, because the width of the waveguide has the same order of magnitude as the wavelength of the guided wave. Therefore, in the THz region, the width of a waveguide is of the order of one hundred micrometers. Comprehensive studies of THz waveguides have been carried out on rectangular and circular

metallic waveguides [Gal00], dielectric fibres [Jam00], parallel metal plates [Mel06, Mel09, Zha04], and metal wires [Wan04].

Since time-domain THz spectroscopy has stimulated research in a wide range of disciplines and has proven to be a valuable technique for the study of vibrational excitations in materials, employing waveguide structures in THz spectroscopy has become attractive and prevalent because deposition of an analyte film provides a long interaction path length resulting in highly sensitive absorption measurements. Of the many different geometries available, THz parallel copper-plate waveguides (PPWG) have become important because this geometry is easily manipulated for opening and closing as well as changing samples. High sensitivity and resolution are necessary for performing precision absorption measurements at cryogenic temperatures in order to elucidate the physics of low lying inter- and intramolecular vibrations. Narrower line widths at low temperature allow the identification and quantification of spectral features that may not be resolved at room temperature. The Grischkowsky group pioneered THz absorption studies of molecular films at cryogenic temperatures with PPWG [Mel06, Mel09]. In their experimental setup, high resistivity silicon lenses and parabolic mirrors are used for collimating and coupling the THz signal into and out of the PPWG. The THz radiation is generated and detected by photoconductive antennas [Mel06, Mel09, Zha04].

Direct guided THz wave excitation in parallel plate waveguides has been demonstrated by Cao et al. [Cao04]. In that work, a dielectric slab-waveguide embedded within a PPWG was used and the guided wave was excited by optical rectification in a nonlinear optical polymer. Coleman et al. developed a parallel plate THz transmitter which excited a guided wave in a dielectric filled PPWG via a photoconductive switch and/or optical rectification [Col04]. However, THz radiation via unbiased optical rectification generated much weaker field amplitudes compared to the photoconductive switch. Mirrors for in and out-coupling of THz radiation are not always necessary,

e.g. Knab et al. has attached the detection crystal directly to the PPWG for the near-field detection of the THz radiation [Kna10].

In this section we describe an improved and compact THz spectroscopy scheme in which a photo-Dember emitter and ZnTe crystal detector are directly attached to the PPWG. We make use of a recently developed large area photo-Dember emitter based on lateral diffusion currents [Kla10, Kla11a]. These emitters have efficiency close to biased photo-conductive emitters [Dre05]. Since these emitters do not require external bias, the need for an electrical feed-through into the cryostat is eliminated. The large active area of the emitter simplifies positioning the pump laser at the emitter in comparison to single dipole antennas. The THz signals are generated and detected via high-speed asynchronous optical sampling (ASOPS). ASOPS provides video rate acquisition of time-domain THz transients without a mechanical delay stage hence allowing easy on-line alignment and optimization of the THz signal [Bar06, Bar07, Kla09]. In order to characterize the setup we first measure the temperature dependence of the THz emission transmitted through the PPWG. We then discuss the temperature dependence of each component in the cryostat to find the real reason for the temperature dependence of the THz emission. Finally we measure a thin film of 1, 2-dicyanobenzene (1,2DCB) deposited on one side of the copper plate waveguide to characterize the performance of our system by comparing it with published results [Mel06].

4.2 Electromagnetic waves propagating in a parallel plate waveguide

We first discuss the wave propagation in a parallel plate waveguide, as sketched in Fig.1. Two parallel metal plates are placed with a discrete gap a . The plate surfaces are parallel to the $y-z$ plane of the coordinate system, while the electromagnetic waves propagate in the positive direction of the z -

axis. The metal (copper was used in this thesis) plates can be treated as perfect conductors and infinite in the y -extent, therefore, the boundary conditions are $\vec{E}_y(x=0) = \vec{E}_y(x=a) = 0$, $\vec{E}_z(x=0) = \vec{E}_z(x=a) = 0$, and $\vec{H}_x(x=0) = \vec{H}_x(x=a) = 0$.

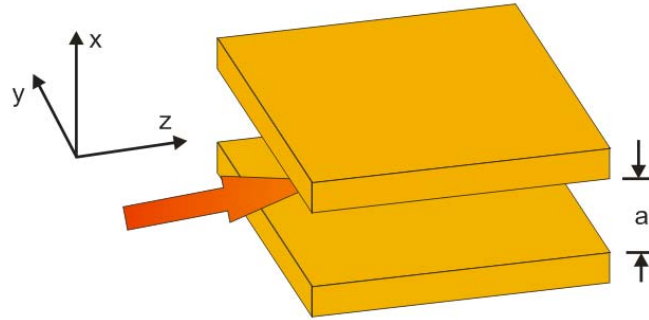


Figure 4.1: sketch of a parallel metal plates waveguide.

The electric field in a waveguide structure always satisfies the complex wave equation:

$$\nabla \times \vec{E}(\vec{r}) = -i\omega\mu_0\vec{H}(\vec{r}) \quad (4.1)$$

$$\nabla \times \vec{H}(\vec{r}) = i\omega\varepsilon\vec{E}(\vec{r}) \quad (4.2)$$

By taking the curl of Eq. (4.1) and substituting the derivative of Eq. (4.2), as well as using Eq. (2.4.8) the electric field follows:

$$\nabla^2 \vec{E}(\vec{r}) = -\omega^2 \mu_0 \varepsilon \vec{E}(\vec{r}) \quad (4.3)$$

Similarly we can also get $\nabla^2 \vec{H}(\vec{r}) = -\omega^2 \mu_0 \varepsilon \vec{H}(\vec{r})$ (4.4)

4.2.1 TE modes

The abbreviation TE stands for *transverse electric* which means that the electric fields are always perpendicular to the propagation direction of the

guided waves (here positive z -direction). Therefore for TE modes, the electric fields can be presumed pointing in the y -direction and expressed by:

$$\vec{E}(\vec{r}) = \hat{y}f(x)e^{-ik_z z} \quad (4.5)$$

By plugging the assumed solution Eq. (4.5) into Eq. (4.3), we can get:

$$-\frac{\partial^2 f(x)}{\partial x^2} = (\omega^2 \mu_0 \varepsilon - k_z^2)f(x) \quad (4.6)$$

Combing the Eq. (4.6) and the boundary conditions, the solution of Eq. (4.6) gives:

$$f(x) = E_0 \sin(k_x x) \quad \text{with } k_x = \frac{m\pi}{a}, \quad m = 1, 2, 3, \dots \quad (4.7)$$

Furthermore, the electric field can be expressed by:

$$\vec{E}(\vec{r}) = \hat{y}E_0 \sin\left(\frac{m\pi}{a}x\right)e^{-ik_z z}, \quad m = 1, 2, 3, \dots \quad (4.8)$$

The different values of m correspond to different TE modes. Eq. (4.8) implies $\left(\frac{m\pi}{a}\right)^2 + k_z^2 = \omega^2 \mu_0 \varepsilon$ according to the requirement of Eq. (4.6), which gives the dispersion relation of the TE _{m} guided modes:

$$k_z = \sqrt{\omega^2 \mu_0 \varepsilon - \left(\frac{m\pi}{a}\right)^2} \quad (4.9)$$

For Eq. (4.9), if the angular frequency ω is less than $\omega_c = \frac{1}{\sqrt{\mu_0 \varepsilon}} \left(\frac{m\pi}{a}\right)$, k_z will become entirely imaginary and the mode does not propagate in the waveguide (decays exponentially with distance). Therefore, ω_c is called the *cut-off frequency*. Since the temporal behaviour of the guided waves is

expected to resemble that of waves in a vacuum condition, the *cut-off frequency* ω_c can be rewritten as $\omega_c = \frac{m\pi c}{a}$. Apparently, if $m = 0$, all field components will vanish, therefore, m starts from 1.

Since we have got the solution of electric field, the remaining magnetic field can also be calculated. Plugging the electric field solution Eq. (4.8) into Eq. (4.1) the magnetic field gives:

$$\vec{H}(\vec{r}) = \frac{iE_0}{\omega\mu_0} \left[\hat{z} \frac{m\pi}{a} \cos\left(\frac{m\pi}{a}x\right) + \hat{x}ik_z \sin\left(\frac{m\pi}{a}x\right) \right] e^{-ik_z z} \quad (4.10)$$

Clearly, $\vec{H}(x)$ satisfies the boundary condition. So far, the three field components are given and can form an electromagnetic wave to propagate in the positive z -direction in the waveguide. In contrast, the magnetic field is not perpendicular to the propagation direction due to $\vec{H}(z) \neq 0$, which is different from electromagnetic waves propagating in free space.

4.2.2 TM modes

The abbreviation TM stands for *transverse magnetic*, which means that the magnetic field instead of the electric field is always perpendicular to the propagation direction. The theoretical approach is analogue to that of TE modes.

We solve Eq. (4.4) by assuming the solution form:

$$\vec{H}(\vec{r}) = \hat{y}g(x)e^{-ik_z z} \quad (4.11)$$

Plugging the assumed solution Eq. (4.11) into Eq. (4.4), we get:

$$-\frac{\partial^2 g(x)}{\partial x^2} = (\omega^2 \mu_0 \varepsilon - k_z^2)g(x) \quad (4.12)$$

Then combining Eq. (4.12) and the boundary conditions, the solution gives:

$$g(x) = H_0 \cos(k_x x) \quad \text{with } k_x = \frac{m\pi}{a}, \quad m = 0, 1, 2, \dots \quad (4.13)$$

Therefore, the solution for the magnetic field becomes:

$$\vec{H}(\vec{r}) = \hat{y} H_0 \cos\left(\frac{m\pi}{a} x\right) e^{-ik_z z} \quad (4.14)$$

The different m values again mean different TM modes. The *dispersion relation* can also be obtained as:

$$k_z = \sqrt{\omega^2 \mu_0 \varepsilon - \left(\frac{m\pi}{a}\right)^2} \quad (4.16)$$

which is identical with that of TE modes, while the *cut-off frequency* ω_c can also be given with the identical form $\omega_c = \frac{m\pi c}{a}$.

The remaining electric field can be obtained by substituting Eq. (4.14) into Eq. (4.2):

$$\vec{E}(\vec{r}) = \frac{iH_0}{\omega \varepsilon} \left[\hat{z} \frac{m\pi}{a} \sin\left(\frac{m\pi}{a} x\right) + \hat{x} i k_z \cos\left(\frac{m\pi}{a} x\right) \right] e^{-ik_z z}, \quad (4.15)$$

where the boundary condition for the electric field $\vec{E}_z(x=0) = \vec{E}_z(x=a) = 0$ is again automatically satisfied. Eq. (4.15) implies that the magnetic field is always perpendicular to the propagation direction for TM modes.

For the special case of $m = 0$, it can be seen from Eq. (4.15) that only \vec{E}_z vanishes while \vec{E}_x remains, this is different from TE modes in which all components vanished. However in this case, the electric and magnetic fields are all not a function of x anymore, and both of the fields are perpendicular

to the propagation direction, therefore this mode is referred to as TEM mode. In this case the dispersion relation will be $k_z = \sqrt{\omega^2 \mu_0 \epsilon}$, which is identical to that in free space and means that the group and the phase velocities are equal to the speed of light. The *cut-off frequency* will be $\omega_c = 0$, which means that the electromagnetic waves can always propagate in the TEM mode in the waveguide, regardless of plate separation and frequency. Therefore, by choosing a suitable separation a , the waveguide can allow waves only below a given frequency (*cut-off frequency* for $m = 1$) to propagate in the waveguide with TEM mode. For instance, for a separation of $a = 100 \mu\text{m}$, the *cut-off frequency* for $m = 1$ is:

$$\nu_c = \frac{\omega}{2\pi} = \frac{c}{2a} = 1.5 \text{ THz} \quad (4.16)$$

which means that for frequencies below 1.5 THz, only the TEM mode waves are available, all higher TM modes and all TE modes are forbidden.

Experimental study on TEM mode propagation in parallel metal waveguides has been carried out by Mendis et al. in Ref. [Men01]. In their work, two copper parallel-plate waveguides with the same separation of $108 \mu\text{m}$ but different lengths of 12.6 mm and 24.4 mm were used, giving a corresponding *cut-off frequency* of 1.39 THz ($m=1$). Figure 4.2 shows the THz pulses transmitted through the two different length waveguides, the power loss is relatively low compared with metal tubes and dielectric fibres [Lee09], and the absorption coefficient is less than 0.2 cm^{-1} in the whole spectral range transmitted.

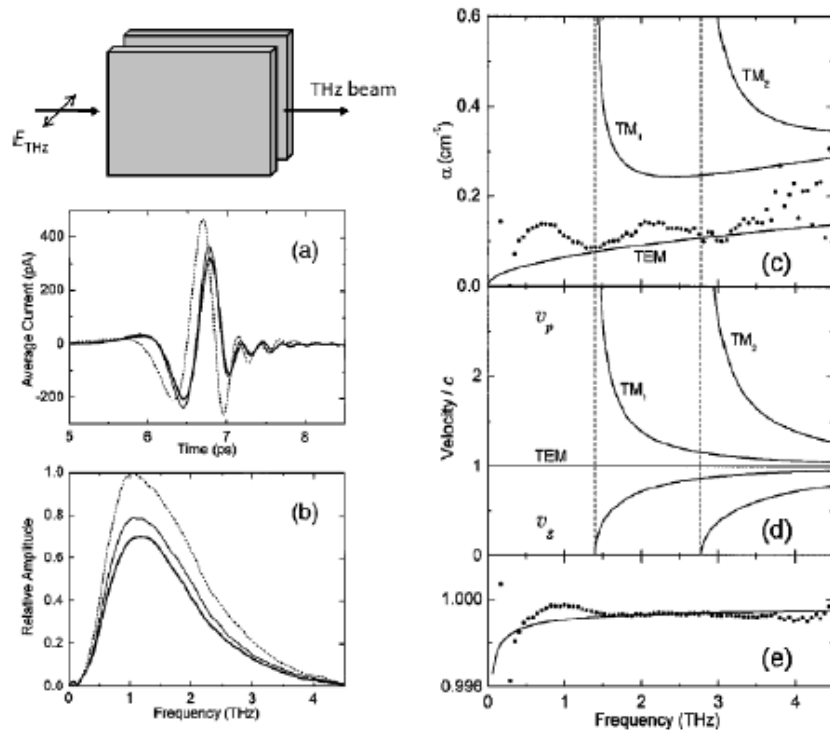


Figure 4.2: (a) Waveforms and (b) spectra of broadband THz pulses transmitted through a 12.6- and a 24.4- mm long copper parallel-plate waveguides with a 108 μm gap. The dashed lines represent the reference pulses. The thin and thick solid curves correspond to the output of short and long waveguides, respectively. (c) Amplitude absorption constant, (d) phase and group velocity of the first three modes scaling with the speed of light, and (e) the scaled velocity of the TEM mode in the vicinity of unity. Solid lines are the calculations for the first three modes, and the filled circles indicate experimental values. (Reprinted from Ref. [Men01])

4.3 Experimental setup

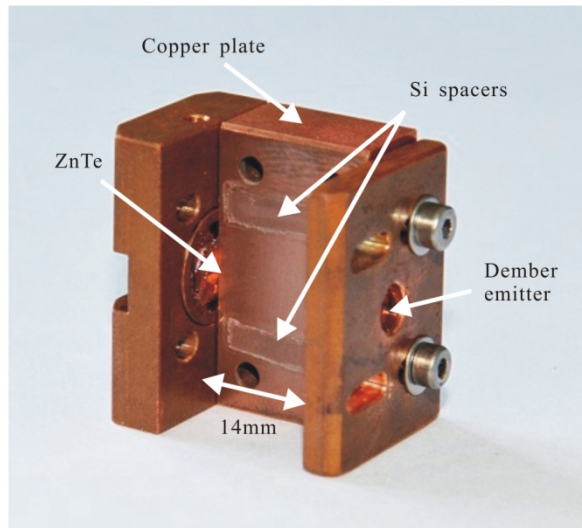
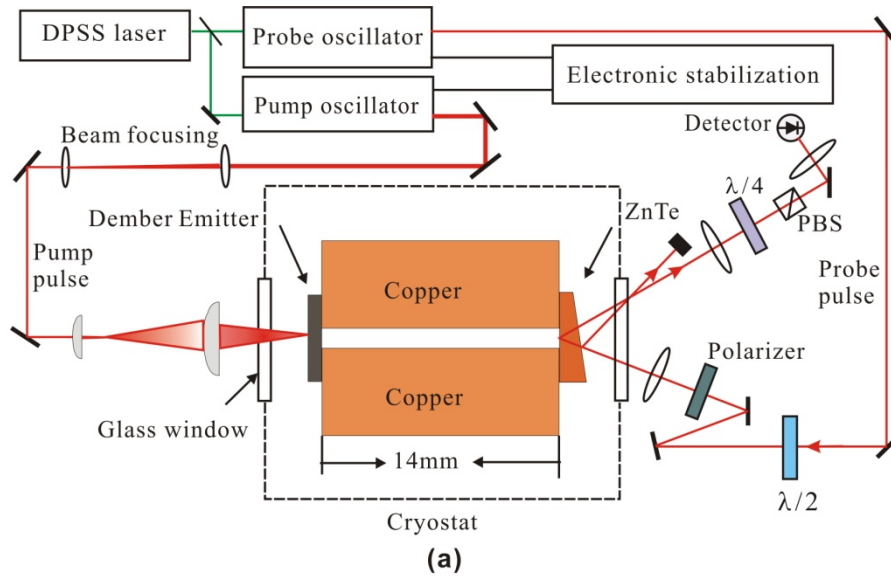


Figure 4.3: (a) Sketch of the THz waveguide setup (top view). (b) Photograph of the PPWG with one of the polished copper plates removed.

ASOPS provides a platform for ultrafast spectroscopy having excellent long-term stability and sensitivity near the shot noise limit. We implement ASOPS with two mode-locked Ti:sapphire laser oscillators working at a nominal repetition rate of approximately 1 GHz. A frequency offset between the two lasers is precisely maintained at a frequency of close to 2 kHz. One laser serves as a pump for the photo-Dember emitter and the second beam probes

THz-induced reflectivity changes in a ZnTe electro-optic (EO) crystal [Kla10, Kla11a, Dre05]. A time-delay between pump and probe beam of 1 ns is scanned at the offset frequency of 2 kHz with a time resolution of 50 fs [Geb10].

The THz waveguide consists of two polished parallel copper plates (Fig. 4.3). Two Si-strips with the dimensions $125\ \mu\text{m} \times 10\ \text{mm} \times 2\ \text{mm}$ provide a separation of the waveguide of $125\ \mu\text{m}$. Since the Si spacers are prepared from a Si wafer with homogeneous thickness, the waveguide plate separation is expected to be homogeneous with deviations smaller than $1\ \mu\text{m}$. Screws provide pressure on the waveguide plates and the Si spacers. The temperature dependence of the waveguide plate separation is hence determined by the temperature dependence of the thickness of the Si spacers (linear expansion coefficient of Si along (100) directions is $\alpha=2.6 \times 10^{-6}/\text{K}$ [Oka84]).

The assembly is attached to the temperature-controlled cold finger of a helium flow cryostat. Near-infrared ultra short pump pulses are focused with a cylindrical lens onto the photo-Dember emitter located directly on the PPWG entrance aperture slit. The generated THz pulses propagate through the PPWG and are detected with an EO sampling scheme [Wu95]. The THz field induces small polarization changes in the reflected probe beam from a wedged ZnTe crystal. We carefully isolated the probe beam reflected from the inner surface of the crystal (i.e. the laser light reflected from the front surface is blocked) and focused it onto a single detector after passing through a $\lambda/4$ wave plate and polarizing beam splitter. The Dember structure of our emitter is fabricated on a $1\ \mu\text{m}$ thick film of $\text{In}_{0.53}\text{Ga}_{0.47}\text{As}$ grown on a $514\ \mu\text{m}$ thick InP wafer with an active area of $1\ \text{mm} \times 1\ \text{mm}$ [Kla10]. Thin films of 1,2DCB are made by dropping $\sim 30\ \text{ml}$ of $20\ \text{mg/ml}$ solution of 1, 2DCB in toluene on one plate of the PPWG. The mass of the film is estimated to be $25\text{-}30\ \mu\text{g}$ on an area of $10 \times 13\ \text{mm}$.

Figure 4.4 shows the measured THz transient from the bare PPWG in vacuum conditions at 300 K. Several multiple reflections show up behind the primary pulse. The first reflection has a time delay around 8.3 ps behind the

primary pulse, which is caused by the multiple reflections in our wedged ZnTe crystal which has a thickness of 300-400 μm . The second reflection has a time delay around 12.2 ps and is caused by the Dember emitter which has a thickness of 515 μm . These echoes limit the time windows used for the Fourier transformation.

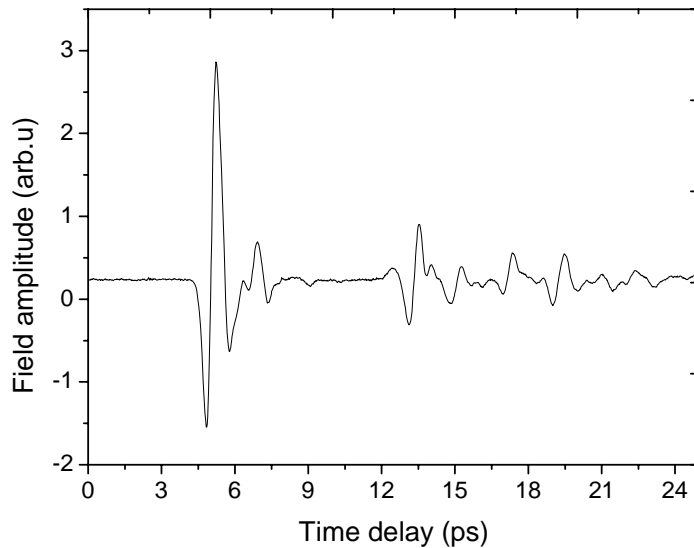


Figure 4.4: THz pulse transmitted from bare PPWG at 300 K. Time zero is arbitrary.

4.4 Temperature dependence of the PPWG THz spectrometer

Since the THz emitter and THz detection crystal as well as the copper waveguide are all placed inside the cryostat, it is necessary to characterize the temperature-dependent response of each component in the cryostat. The THz emission from the PD emitter after passing through the bare copper PPWG is shown for different temperatures in Fig. 4.5. The spectra in Fig. 4.5(b) are obtained by Fourier transformation of the time-domain wave forms in Fig. 4.5(a). Compared with a Dember emitter in a conventional free-space set-up with 4 paraboloids [Kla10] the detected spectrum at 300 K is strongly reduced in bandwidth in the waveguide. We attribute this effect to the less efficient coupling, transmission and detection of higher frequencies in the PPWG [Gal00]. As the temperature decreases from 300 K to 5 K, the peak-

to-peak amplitudes of THz pulses show an apparent increase by more than a factor of 2. The useful frequency range of the detected THz spectra extends from 0.1 THz to almost 3 THz.

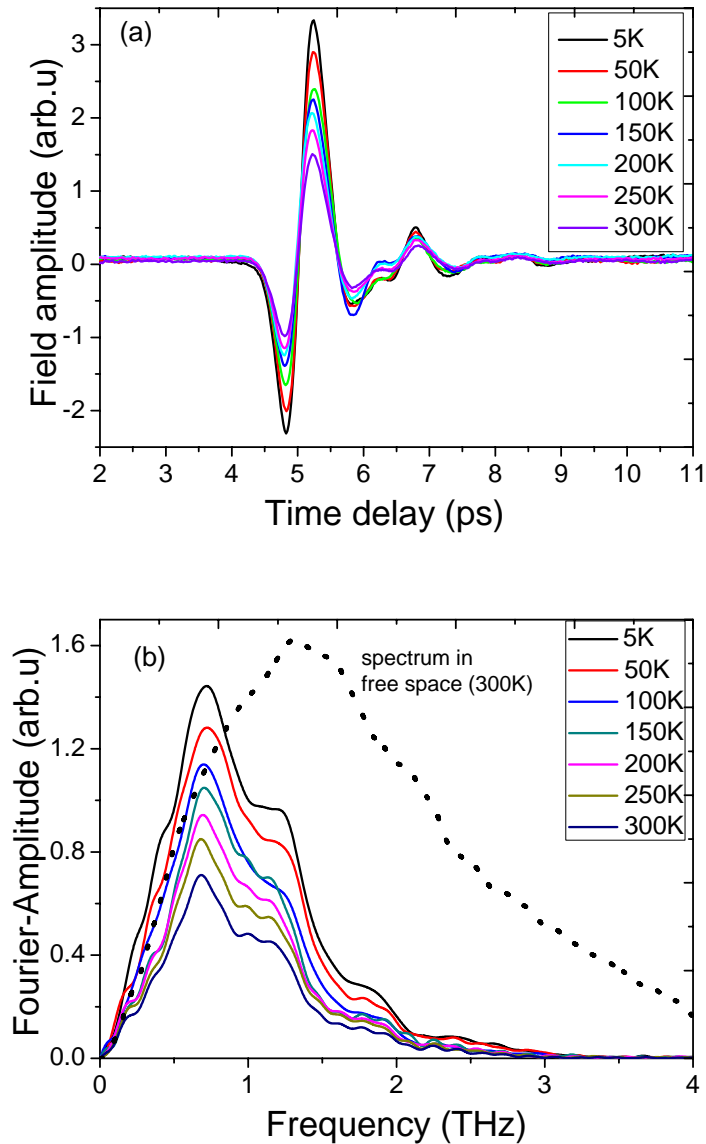


Figure 4.5: (a) THz transients for the uncoated PPWG measured from 5 K to 300 K at intervals of 50 K. (b) Corresponding Fourier transform spectra (For comparison, the dotted line is the spectrum of the Dember emitter THz pulse in a free space set-up at room temperature).

First we consider the thermal effects on the copper waveguide: for a given

waveguide separation and a free-space wavelength the absorption coefficient of an air-spaced PPWG is determined by the conductivity of the waveguide plates [Mar93]. Previous studies on the PPWGs constructed of bulk copper have shown that the conductivity did not show an increase upon reducing the temperature [Lam07]. Therefore, the temperature dependence of the amplitudes of THz pulses resulting from thermal effects of the copper waveguide can be neglected.

EO detection is a nonlinear $\chi_{(2)}$ mixing process where the temperature-dependence of the refractive index and the EO-coefficient r_{41} have to be considered. The measured polarization change of the probe pulse is proportional to the anisotropic change of refractive index induced by the THz field E_{THz} in the ZnTe crystal [Lee09], i.e. it is proportional to $n_0^3 r_{41} E_{\text{THz}}$, where n_0 is the refractive index at the frequency of the probe pulse. Since the energy of the probe pulse (1.55 eV) is well below the band gap of ZnTe (2.26 eV at 300 K) n_0 is expected to decrease as the band gap increases at low temperature (2.38 eV, 10 K) [Yu01]. In addition, the frequency of the THz radiation is well below the TO phonon resonance in ZnTe (5.32 THz) [Lee09, Sch01], so we also expect a weak influence of temperature on the dispersion of the THz wave. The EO coefficient r_{41} is also assumed to be weakly temperature-dependent away from electronic resonances [Och07]. From the dispersion of r_{41} measured at room temperature [Sli66], we expect that r_{41} will decrease when the band gap shifts toward higher energy at lower temperatures. All these factors lead to an anticipated decrease of the detected polarization changes when the temperature drops from 300 K to 5 K, yet we observe an increase by more than a factor of 2.

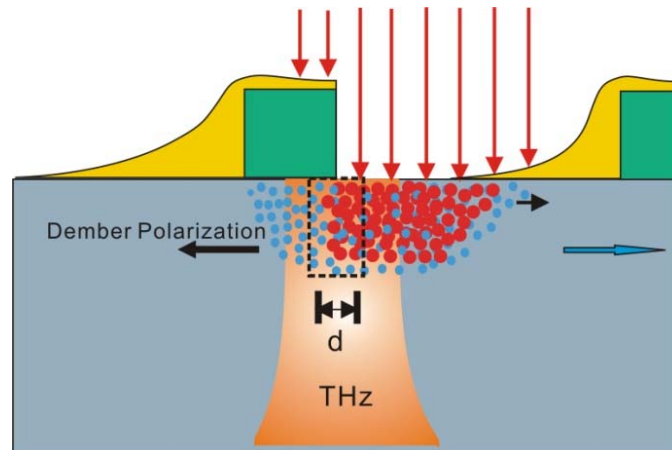


Figure 4.6: Sketch of Dember emitter generating THz through lateral diffusion currents. Two gold stripes (yellow) and photoresist bars (green) are shown. The excitation spot covers more than 10 of these gold stripes. A strong carrier gradient is formed at the edge of the photoresist bars due to the ambipolar diffusion of electrons (blue dots) and holes (red dots) [Kla10]. The faster diffusion of electrons leads to the rapid build-up of a polarization parallel to the surface with preferred THz emission into forward direction.

Photo-Dember emitters are based on ultrafast lateral diffusion currents in a semiconductor [Dek96], hence the temperature dependence of carrier transport has to be considered. The principle of THz pulse generation in such a device is shown in Fig. 4.6. A metalized Au stripe blocks a portion of the absorbed pump beam, producing a steep photo-carrier concentration gradient immediately beneath the stripes. The diffusion rate of electrons is much higher than that of holes, resulting in a lateral charge separation parallel to the surface. The acceleration of photo-electrons relative to holes leads to the emission of a THz pulse transient in forward direction. The gold layer has a gradually decreasing thickness that substantially weakens the photocarrier gradient in the direction away from the edge. This strongly reduces the radiation dipole vector in the reverse direction, which is necessary to build up a significant radiation signal in the far-field. The structure depicted in Fig. 4.6 is repeated with a period of $5\ \mu\text{m}$ to form a large area emitter. More than 10 of these stripes are covered by the spot of the pump laser.

A significant difference in diffusion constants for electrons and holes is important for the THz generation via the photo-Dember effect. The diffusion constant of charge carriers is given by the Einstein relation $D_i = \mu_i K_B T_i / e$, where μ_i is the mobility, K_B is the Boltzmann constant, T_i is the temperature of the carrier distribution, and the index i denotes electrons or holes. The mobility ratio for electrons and heavy holes in undoped $\text{In}_{0.53}\text{Ga}_{0.47}\text{As}$ at 300K is about 40 (12000 cm^2/Vs and 300 cm^2/Vs , respectively) [Kla10], suggesting that electrons have a 40 times higher diffusion constant compared to holes. Since the diffusion length l is proportional to $\sqrt{D_i t}$, it is a factor of 6 larger for electrons compared to holes in a given time t . The application of the Einstein relation has to be considered carefully, since the photo-carriers are described by two different temperatures in the first picoseconds after excitation [Dek93]. The effective temperature of the electrons will be higher than that of the holes because of the dispersion of the valance and conduction band. The higher electron temperature will further increase the transient diffusivity of electrons compared to the holes.

The most important temperature-dependent carrier scattering process in polar semiconductors is the interaction with LO phonons described by the Fröhlich potential. The population of LO phonons decreases as the temperature drops from 300 K to 70 K, leading to a concomitant increase of the mobility and diffusivity. This explains the temperature trend of the THz peak signal that is clearly visible in Fig. 4.7: from 300 K down to 5 K the THz peak amplitude increases by a factor of 2.2. One would also expect an increase in bandwidth of the detected spectrum at lower temperature when the mobility increases. However, since the detected bandwidth is limited by the PPWG set-up and not by the Dember emitter, this effect is strongly suppressed. The full description of the diffusion dynamics including non-equilibrium effects requires a Monte-Carlo simulation from which the THz radiation can be calculated [Joh02, Kla11b].

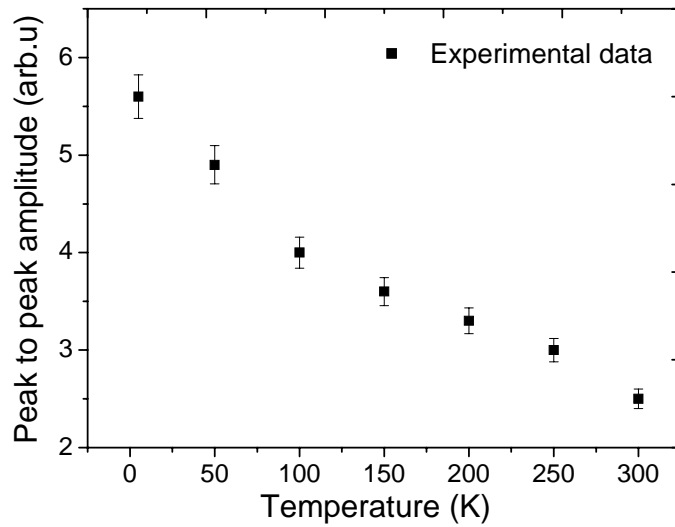


Figure 4.7: THz emission (peak to peak amplitude) from Dember emitter at different temperatures with error bars.

4.5 1,2DCB absorption measured in the PPWG

We made absorption measurements of 1, 2DCB film at different temperatures to characterize the capabilities of our waveguide THz-TDS. To eliminate distortion from the PPWG, we recorded signals with and without the film present. Fig. 4.8(a) shows room temperature THz transients upon propagation through the bare PPWG (blue curve) and after coating one plate with 1, 2DCB film (red curve). Compared with the bare PPWG, the field amplitude of THz pulse with the 1, 2DCB film is strongly reduced. The 1, 2DCB film also induces a time delay of ~ 0.4 ps and additional ringing after the main pulse. The corresponding Fourier spectra are presented in Fig. 4.8(b). An absorption line at 750 GHz is in close proximity to a previously reported absorption feature at 760 GHz [Mel06]. At frequencies above 1 THz the THz amplitude is strongly decreased due to a higher lying absorption line at 1.4 THz that is much stronger than the one at 750 GHz [Mel06].

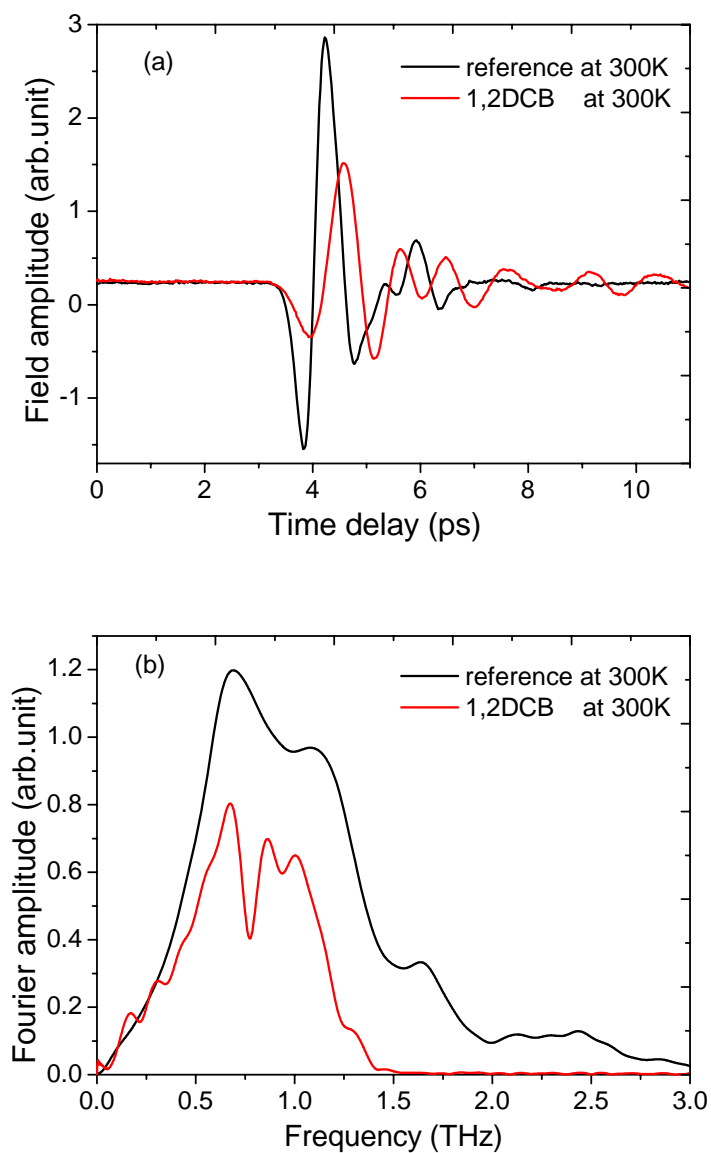


Figure 4.8: (a) THz transients for the uncoated PPWG (blue curve) and one plate coated with 1, 2 DCB (red curve) at 300 K. (b) Corresponding Fourier transmission spectra.

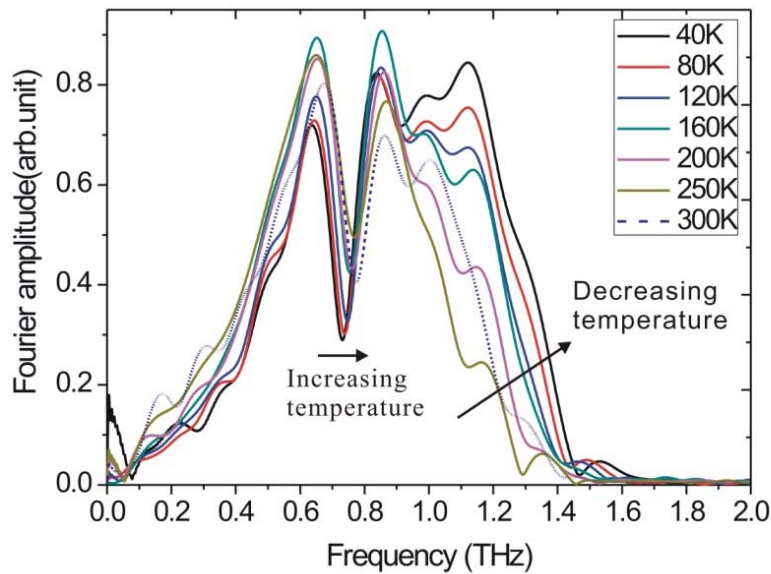


Figure 4.9: THz spectra of the 1, 2 DCB polycrystalline film on the inner surface of the PPWG for different temperature from 40 K to 300 K.

Figure 4.9 shows THz transmission spectra of 1,2DCB measured over the temperature range from 40 K to 300 K. Two trends are evident as the temperature increases: i) the high frequency cut-off of the spectra moves to lower frequencies (from around 1.4 THz at 40 K to 1.2 THz at 300 K). This is explained by the narrowing of the strong absorption peak at 1.4 THz at low temperatures as reported in [Mel06]; ii) a blue-shift of the absorption peak near 750 GHz. The line width (90 GHz FWHM) of this peak is mainly limited by the time window used for the Fourier transform of the data. Therefore, we cannot clearly see the narrower effect of the peak toward decreasing temperatures as reported from Ref. [Mel06]. The shift of the peak around 750 GHz as a function of temperature is plotted in Fig. 4.10. We can rule out temperature-induced changes to the EO-detection [Val05]. We attribute this shift to the anharmonicity of inter-molecular vibrations resulting from a steeper inter-molecular potential at higher temperatures. The observed blue shift at increased temperatures is inconsistent with Ref. [Mel06], where a temperature-dependent red-shift of the same absorption

peak is reported. We like to note that the observed shift is consistent with experiments on 4INBP [Mel09]. However, this discrepancy requires further studies and underscores the importance of calculating and assigning the low energy modes.

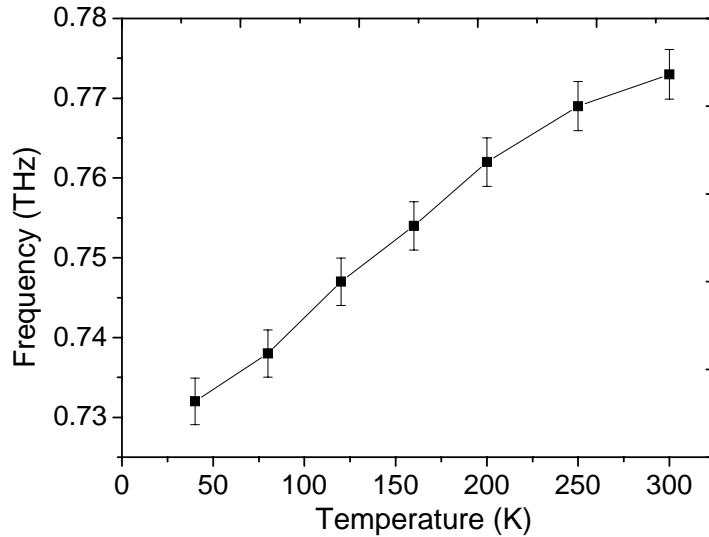


Figure 4.10: Temperature dependence of the frequency of the absorption peak around 750 GHz with error bars.

4.6 Conclusion

We built and tested a compact temperature-tuneable THz time domain waveguide spectrometer based on an unbiased photo-Dember emitter, electro-optic detection, and asynchronous optical sampling. We analyzed the theory of electromagnetic wave propagation inside such a waveguide. At last we measured the far-infrared transmission of a 1, 2-dicyanobenzene film in the temperature range 40-300 K and found subtle changes in the absorption spectra.

Summary and Outlook

In this thesis, two THz-TDS systems were presented. The first one was the reflection THz-TDS system for the study of liquids. By using this system we measured liquid water as well as water based HCl and NaCl solutions. The Debye model and an extend model based on the Debye model and harmonic dampened oscillators were used to analyze the measurement results of liquid water and water based solutions. The second one was a compact low-temperature parallel metal-plate waveguide THz-TDS system. Using this system we studied the temperature dependence of newly developed photo-Dember emitter as well as the temperature dependence of an absorption line of 1, 2-dicyanobenzene below 1 THz.

In Chapter 2, the experimental basics were described. THz time domain spectroscopy using ultra short laser pulses was reviewed. THz generation from a large area microstructured photoconductive switch and from a photo-Dember emitter as well as THz detection using an electro-optic crystal were carefully introduced. The principle and setup of the time-domain technique used in this work (ASOPS) was described. The fundamentals of interaction between electromagnetic waves and matter were also given in this chapter.

In Chapter 3, we presented THz time domain reflection spectroscopy of aqueous systems. The data analysis required for data obtained in this setup was also given. The Debye model and dampened harmonic oscillator model were carefully introduced and applied for the analysis of the dielectric relaxation of water and water based solutions. A linear increase of the dielectric function compared with pure water with increasing ion concentrations was verified by both experiment and theoretic analysis.

In Chapter 4, we presented a compact low-temperature THz parallel plate waveguide spectrometer. The temperature dependence of the system

including the photo-Dember emitter, the copper plate, and the electro-optic crystal was discussed. Using this setup we measured the absorption of 1,2-dicyanobenzene at different temperatures. We found that the absorption peak around 750 GHz of 1, 2-dicyanobenzene displays a blue shift with increasing temperature.

Outlook

For the reflection THz-TDS aqueous system: the strong thermal expansion of the copper holder makes it difficult to study the temperature dependence of the dielectric relaxation of liquids. To solve this problem, one can change the 60° angle of incidence of the THz pulse onto the silicon wafer to normal incidence, or replace the copper holder with a holder with weak thermal effects but good heat conductance, or optimize the alignment for each temperature and take both reference signal and the sample signal every time, however the last solution will take much longer and will bring in some uncontrollable influences to the results.

The extended ion solutions model indicates that the molar volume of anions and cations can strongly affect the dielectric function by reducing the concentration of bulk water in ion solutions; one can verify this prediction by performing measurements of NaCl, NaBr and NaI solutions with the same concentration. Further experimental and theoretical study will be needed to fully understand the dynamics in ionic solutions.

For the waveguide spectrometer, the temperature dependence of a photo-Dember emitter can be more precisely studied by using a free space setup. The time window of the signal used for Fourier transform is limited by the echoes from the ZnTe and Dember emitter. To improve this one can use thicker ZnTe crystals and emitters. A thicker ZnTe crystal will also be helpful to increase the resolution and sensitivity of the setup. Many other interesting samples can be measured using this setup, for instance fluorescent materials, ferroelectric materials, drugs and many organic materials.

Zusammenfassung und Ausblick

In dieser Arbeit wurden zwei THz-Zeitbereich-Systeme vorgestellt. Das erste diente der Zeitbereich-THz Spektroskopie in Reflexion an wässrigen System. Mit diesem System haben wir flüssiges Wasser sowie Lösungen von HCl und NaCl in Wasser gemessen. Das Debye-Modell und ein erweitertes Modell auf Basis des Debye-Modells und gedämpfter harmonischer Oszillatoren wurden verwendet, um die Messergebnisse von flüssigem Wasser und wässrigen Lösungen zu analysieren. Das zweite System war ein kompaktes Zeitbereich-THz Tieftemperatur System mit parallelen Metallwellenleitern. Mit diesem System untersuchten wir sowohl die Temperaturabhängigkeit eines neu entwickelten Photo-Dember Emitters als auch die Temperaturabhängigkeit einer Absorptionslinie des 1,2-Dicyanobenzol unterhalb 1 THz.

In Kapitel 2 wurden die experimentellen Grundlagen beschrieben. Die Grundlagen der Zeitbereich-Spektroskopie im THz-Bereich mittels ultrakurzer Laserpulse wurden vorgestellt. Die Prinzipien der THz-Generation in einem großflächigen mikrostrukturierten photoleitenden Schalter und einem Photo-Dember-Emitter sowie der THz-Detektion unter Verwendung eines elektro-optischen Kristalls wurden dargelegt. Das Prinzip und der Aufbau für die Zeitbereich-Spektroskopie, die in dieser Arbeit (ASOPS) verwendet wurde, wurde beschrieben. Die Grundlagen der Wechselwirkung zwischen elektromagnetischen Wellen und Materie wurde auch in diesem Kapitel erläutert.

In Kapitel 3 präsentierten wir Zeitbereich-THz Reflektions-spektroskopie an wässrigen System. Die Datenanalyse für die in diesem Aufbau erzielten Resultate wurde ebenfalls dargestellt. Das Debye-Modell und das Modell des gedämpften harmonischen Oszillators wurden ausführlich erläutert und für die Analyse der dielektrischen Relaxation von Wasser und Wasser-basierten Lösungen angewendet. Eine lineare Erhöhung der dielektrischen Funktion im

Vergleich mit reinem Wasser mit zunehmender Ionenkonzentration wurde sowohl im Experiment als auch in theoretischen Analysen verifiziert.

In Kapitel 4 präsentierten wir ein kompaktes Tieftemperatur-THz-Spektrometer mit planparallelem Wellenleiter. Die Temperaturabhängigkeit des Systems, einschließlich des Photo-Dember-Emitters, der Kupferplatte und des elektro-optischen Kristalls wurde diskutiert. Mit diesem Aufbau wurde die Absorption von 1,2-Dicyanbenzol bei verschiedenen Temperaturen gemessen. Wir fanden, dass der Absorptions-Peak um 750 GHz von 1,2-Dicyanbenzol eine Blauverschiebung mit zunehmender Temperatur zeigt.

Ausblick

Für die Zeitbereich-THz-Spektroskopie in Reflexion an wässrigen System: die störende thermische Ausdehnung der Kupferhalterung erschwert die Untersuchung der Temperaturabhängigkeit der dielektrischen Relaxation von Flüssigkeiten. Um dieses Problem zu lösen, kann man den Einfallswinkel von 60° der THz-Impulse auf den Silizium-Wafer durch senkrechten Einfall ersetzen oder die Kupferhalterung durch einen Halter mit geringen thermischen Effekten aber guter Wärmeleitfähigkeit austauschen, oder die Ausrichtung bei jeder Temperatur optimieren und jeweils sowohl Referenzsignal als auch das Probensignal aufnehmen, aber diese letzte Möglichkeit dauert viel länger und würde die Messergebnisse unkontrolliert beeinflussen.

Das erweiterte Modell für ionische Lösungen zeigt, dass das Molvolumen von Anionen und Kationen starken Einfluss auf die dielektrische Funktion haben kann, indem es die Konzentration des reinen Wassers verringert; man kann diese Vorhersage durch eine einfach durchzuführen Messungen von NaCl, NaBr und NaI-Lösungen mit der gleichen Konzentration überprüfen. Weitere experimentelle und theoretische Untersuchung werden für ein vollständiges Verständnis der Dynamik ionischer Lösungen benötigt.

Für das Wellenleiter-Spektrometer: die Temperaturabhängigkeit des Foto-Dember-Emitters kann durch die Verwendung eines Setups mit Freistrahlspropagation besser untersucht werden. Das Zeitfenster des Signals für die Fouriertransformation wird durch das Echo des Dember-Emitters beschränkt; um dies zu verbessern kann ein dickerer Emitter verwendet werden. Um die Auflösung und Empfindlichkeit des Setups zu erhöhen, wird auch ein dickerer ZnTe-Kristall benötigt. Viele weitere interessante Proben können unter Verwendung dieser Konfiguration untersucht werden, zum Beispiel fluoreszierende Materialien, ferroelektrische Stoffe, Drogen und viele weitere organische Materialien.

References

- [Afs77] M. N. Afsar and J. B. Hasted, "Measurements of optical-constants of liquid H₂O and D₂O between 6 and 450 cm⁻¹," J. Opt. Soc. Am., **67**, 902 (1977).
- [Agg74] R. L. Aggarwal, B. Lax, H. R. Fetterman et al. "CW generation of tunable narrow-band far-infrared radiation," J. Appl. Phys., **45**(9), 3972 (1974).
- [Agm96] N. Agmon, "Tetrahedral displacement: the molecular mechanism behind the Debye relaxation in water," J. Phys. Chem., **100**, 1072 (1996).
- [Asc05]. R. Ascázubi, C. Shneider, I. Wilke, R. Pino, and P. S. Dutta, "Enhanced terahertz emission from impurity compensated GaSb," Phys. Rev. B, **72**(4), 045328 (2005).
- [Asc06]. R. Ascázubi, I. Wilke, K. J. Kim, and P. Dutta, "Terahertz emission from Ga_{1-x}In_xSb," Phys. Rev. B, **74**(7), 075323 (2006).
- [Aus84] D. H. Auston, K. P. Cheung, and P. R. Smith, "Picosecond photoconducting Hertzian dipoles," Appl. Phys. Lett., **45**, 284 (1984).
- [Bal94] U. Balucani and M. Zoppi, *Dynamics of the liquid state*, Clarendon Press, Oxford (1994).
- [Bar72] F. J. Bartoli and T. A. Litovitz, "Raman scattering: orientational motions in liquids," J. Chem. Phys., **56**, 413 (1972).
- [Bar06] A. Bartels, A. Thoma, C. Janke, T. Dekorsy, A. Dreyhaupt, S. winner, and M. Helm, "High-resolution THz spectrometer with kHz scan rates," Opt. Express, **14** (1), 430 (2006).
- [Bar07] A. Bartels, R. Cerna, C. Kistner, A. Thoma, F. Hudert, C. Janke, and T. Dekorsy, "Ultrafast timedomain spectroscopy based on high-speed asynchronous optical sampling," Rev. Sci. Instrum., **78**, 035107 (2007).
- [Ber89] Y. Berozashvili, S. Machavariani, A. Natsvlishvili, and A. Chirakadze, "Dispersion of the linear electro-optic coefficients and the non-

- linear susceptibility in GaP,” *J. Phys. D: Appl. Phys.*, **22**, 682, (1989).
- [Bot04] A. Botti, F. Bruni, S. Imberti, and M. A. Ricci, “Ions in water: The microscopic structure of a concentrated HCl solution,” *J. Chem. Phys.*, **121**, 7840 (2004).
- [Brü96] E. Bründermann, A. M. Linhart, and H. P. Röser, “Miniaturization of p-Ge lasers: Progress toward continuous wave operation,” *Appl. Phys. Lett.*, **68**(10), 1359 (1996).
- [Cao04] H. Cao, R. A. Linke, and A. Nahata, “Broadband generation of terahertz radiation in a waveguide,” *Opt. Lett.*, **29**, 1751 (2004).
- [Cha70] T. Y. Chang, T. J. Bridges, and E. G. Buihardt, “CW submillimeter laser action in optically pumped methyl fluoride methyl alcohol, and vinyl chloride gases,” *Appl. Phys. Lett.*, **17**, 249 (1970).
- [Cle02] D. Clery, “Brainstorming their way to an imaging revolution,” *Science*, **297**, 761(2002).
- [Col04] S. Coleman and D. Grischkowsky, “Parallel plate THz transmitter,” *Appl. Phys. Lett.*, **84**, 654 (2004).
- [Dek93] T. Dekorsy, T. Pfeifer, W. Kiitt, and H. Kurz, “Subpicosecond carrier transport in GaAs surface-space-charge fields,” *Phys. Rev. B.*, **47**, 3842 (1993).
- [Dek96] T. Dekorsy, H. Auer, H. J. Bakker, H. G. Roskos, and H. Kurz, “THz electromagnetic emission by coherent infrared-active phonons,” *Phys. Rev. B*, **53**(7), 4005 (1996).
- [Dem31] H. Dember, “Ueber eine photoelektronische Kraft in Kupferoxydul-Kristallen,” *Z. Phys.*, **32**, 554 (1931)
- [Dod95] T. Dodo, M. Sugawa, E. Nonaka, and H. Honda, “Absorption of far-infrared radiation by alkali halide aqueous solutions,” *J. Chem. Phys.*, **102**, 6208 (1995).
- [Dre05] A. Dreyhaupt, S. Winnerl, T. Dekorsy, and M. Helm, “High-intensity terahertz radiation from a microstructured large-area photoconductor,” *Appl. Phys. Lett.*, **86**, 121114 (2005).

- [Ext89] M. V. Exter, C. Fattinger, and D. Grischkowsky, "Terahertz time-domain spectroscopy of water vapor," *Opt. Lett.*, **14**, 1128 (1989).
- [Fai94] J. Faist, F. Capasso, D. L. Sivco, C. Sirtori, A. L. Hutchinson, A. Y. Cho, "Quantum cascade laser," *Science*, **264**, 553, (1994).
- [Fox01] Mark Fox, *Optical properties of solid*, Oxford, New York (2001).
- [Fre91] M. A. Frerking, "The submillimeter mission heterodyne instrument," *Proceeding of the 2nd internat. Symposium on space Terahertz Tech.*, 17, Ann Arbor, MI, March (1991).
- [Gal00] G. Gallot, S. P. Jamison, R. W. McGowan, and D. Grischkowsky, "Terahertz waveguides," *J. Opt. Soc. Am. B.*, **17**, 851 (2000).
- [Geb10] R. Gebis, G. Klatt, C. Janke, T. Dekorsy, and A. Bartels, "High-speed asynchronous optical sampling with sub-50fs time resolution," *Opt. Express*, **18**, 5974 (2010).
- [Gri99] D. J. Griffiths, *Introduction to electrodynamics*, Pearson Education, 1999.
- [Gro1806] de Grotthuss and C. J. T, "Sur la décomposition de l'eau et des corps qu'elle tient en dissolution à l'aide de l'électricité galvanique," *Ann. Chim.*, **58**, 54 (1806).
- [Gu02] P. Gu, M. Tani, S. Kono, K. Sakai, and X. C. Zhang, "Study of terahertz radiation from InAs and InSb," *J. Appl. Phys.*, **91**(9), 5533 (2002).
- [Gup92] S. Gupta, J. Whitaker, and G. Mourou, "Ultrafast carrier dynamics in III-V semiconductors grown by molecular-beam epitaxy at very low substrate temperatures," *IEEE Journal of Quantum Electronics*, **28**, 2464 (1992).
- [Has04]. M. P. Hasselbeck, L. A. Schlie, and D. Stalnaker, "Emission of electromagnetic radiation by coherent vibrational waves in stimulated Raman scattering," *Appl. Phys. Lett.*, **85**(2), 173 (2004).
- [Hey03]. J. N. Heyman, N. Coates, A. Reinhardt, and G. Strasser, "Diffusion and drift in terahertz emission at GaAs surfaces," *Appl. Phys. Lett.*, **83** (26), 5476 (2003).

- [Hey08] M. Heyden, E. Bründermann, U. Heugen, G. Niehues, D. M. Leitner, and M. Havenith, “Long-range influence of carbohydrates on the solvation dynamics of water—answers from terahertz absorption measurements and molecular modeling simulations,” *J. Am. Chem. Soc.*, **130**, 5773 (2008).
- [Hil69] N. E. Hill, W. E. Vaughan, A. H. Price, and M. Davis, *Dielectric properties and molecular behaviour*, Van Nostrand Reinhold Company, (1969).
- [Hil85] R. M. Hill and L. A. Dissado, “Debye and non-Debye relaxation,” *J. Phys. C*, **18**, 3829 (1985).
- [Hir04] H. Hirori, K. Yamashita, M. Nagai, and K. Tanaka, “Attenuated total reflectio spectroscopy in time domain using terahertz coherent pulses,” *Jpn. J. Appl. Phys.*, **43**, 1287 (2004).
- [Hor72] R. A. Horne (Ed.), *Water and aqueous solutions: structure, thermodynamics and transport processes*, Wiley-Interscience. New York, (1972).
- [Hu95] B. B. Hu and M. C. Nuss, “Imaging with terahertz waves,” *Opt. Lett.*, **20**, 16, 1716 (1995).
- [Jam00] S. P. Jamison, R. W. McGowan, and D. Grischkowsky, “Single mode pulses in sapphire fibers,” *Appl. Phys. Lett.*, **76**, 1987 (2000).
- [Jep07] P. U. Jepsen, U. Møller, and H. Merbold, “Investigation of aqueous alcohol and sugar solutions with reflection terahertz time-domain spectroscopy,” *Opt. Express*, **15**, 14717 (2007).
- [Jep10] P. U. Jepsen and H. Merbold, “Terahertz reflection spectroscopy of aqueous NaCl and LiCl solutions,” *J. Infrared. Milli Terahz Waves*, **31**, 430 (2010).
- [Joh02] M. B. Johnston, D. M. Whittaker, A. Corchia, A. G. Davies, and E. H. Linfield, “Simulation of terahertz generation at semiconductor surfaces,” *Phys. Rev. B.*, **65**, 165301 (2002).
- [Kin96] J. T. Kindt and C. A. Schmuttenmaer, “Far-infrared dielectric properties of polar liquids probed by femtosecond terahertz pulse spectroscopy,” *J. Phys. Chem.*, **100**, 10373 (1996).

- [Kla09] G. Klatt, R. Gebs, C. Janke, T. Dekorsy, and A. Bartels, “Rapid-scanning terahertz precision spectrometer with more than 6 THz spectral coverage,” *Opt. Express.*, **17** (25), 22847 (2009).
- [Kla10] G. Klatt, F. Hilser, W. Qiao, M. Beck, R. Gebs, A. Bartels, K. Huska, U. Lemmer, G. Bastian, M. B. Johnston, M. Fischer, J. Faist, and T. Dekorsy, “Terahertz emission from lateral photo-Dember currents,” *Opt. Express*, **18** (5), 4939 (2010).
- [Kla11a] G. Klatt, B. Surrer, D. Stephan, O. Schubert, M. Fischer, J. Faist, A. Leitenstorfer, R. Huber, and T. Dekorsy, “Photo-Dember terahertz emitter excited with an Er:fiber laser,” *Appl. Phys. Lett.*, **98**, 021114 (2011).
- [Kla11b] G. Klatt, *Charakterisierung neuartiger terahertz-emitter mittels schneller, präziser terahertz-spektroskopie*, doctoral thesis, Konstanz University (2011) (in German).
- [Kna10] J. R. Knab, A. J. L. Adam, R. Chakkittakandy, and P. C. M. Planken, “Terahertz near-field microspectroscopy,” *Appl. Phys. Lett.*, **97**, 031115 (2010).
- [Koe07] M. Koeberg, C. Wu, D. Kim, and M. Bonn, “THz dielectric relaxation of ionic liquid:water mixtures,” *Chem. Phys. Lett.*, **439**, 60 (2007).
- [Kom82] S. Komiyama, “Far-infrared emission from population-inverted hot-carrier system in p-Ge,” *Phys. Rev. Lett.*, **48**(4), 271 (1982).
- [Lam07] N. Laman and D. Grischkowsky, “Reduced conductivity in terahertz skin-depth layer of metals,” *Appl. Phys. Lett.* **90**(12), 122115 (2007).
- [Lee96] C. Lee, C. Sosa, M. Planas, and J. J. Novoa, “A theoretical study of the ionic dissociation of HF, HCl, and H₂S in water clusters,” *J. Chem. Phys.*, **104**, 7081 (1996).
- [Lee09] Y. S. Lee, *Principles of Terahertz Science and Technology*, Springer Science, New York (2009).
- [Lei99] A. Leitenstorfer, S. Hunsche, J. Shah, M. C. Nuss, and W. H. Knox, “Detectors and sources for ultrabroadband electro-optic sampling: experiment and theory,” *Appl. Phys. Lett.*, **74**, 1516 (1999).

- [Luz96] A. Luzar and D. Chandler, "Effect of environment on hydrogen bond dynamics in liquid water," *Phys. Rev. Lett.*, **76**, 928 (1996).
- [Mar93] N. Marcuvitz, *Waveguide Handbook* (Peter Peregrinus, London, 1993).
- [Mar00] A. G. Markelz, A. Roitberg, and E. J. Heilweil, "Pulsed terahertz spectroscopy of DNA, bovine serum albumin and collagen between 0.1 and 2.0 THz," *Chem. Phys. Lett.*, **320**, 42 (2000).
- [Mcm91] R. W. Mcmillan, C. W. Trussell, R. A. Bohlander, J. C. Butterworth, and R. E. Forsythe, "An experimental 225 GHz pulsed coherent radar," *IEEE Trans MTT*, **39**, 555 (1991).
- [Mel06] J. S. Melinger, N. Laman, S. Sree Harsha, and D. Grischkowsky, "Line narrowing of terahertz vibrational modes for organic thin polycrystalline films within a parallel plate waveguide," *Appl. Phys. Lett.*, **89**, 251110 (2006).
- [Mel09] J. S. Melinger, S. S. Harsha, N. Laman, and D. Grischkowsky, "Guided-wave terahertz spectroscopy of molecular solids," *J. Opt. Soc. Am. B*, **26**, A79 (2009).
- [Men01] R. Mendis and D. Grischkowsky, "Undistorted guided-wave propagation of subpicosecond terahertz pulses," *Opt. Lett.*, **26**, 846 (2001).
- [Mer06] H. P. Merbold, *Terahertz time-domain spectroscopy of aqueous systems in reflection geometry and construction of polarisation-sensitive photoconductive terahertz antennas*, Deplom thesis, Freiburg university, (2006).
- [Mit08] S. Mitchell, "Electromagnetic wave propagation-theory and application to bathymetric lidar simulation", ASEN 6849 Fall 2008.
- [Mor92] G. Moruzzi, F. Strumia, and J. C. Silos Moraes. "Far infrared laser lines and assignments of CH₃OH: a review," *Int. J. Infrared and Millimeter Waves*, **13**, 1269 (1992).
- [Mor08] D. Morin, *Introduction to classical mechanics -with problems and solutions*, Cambridge University Press, (2008)

- [Møl09] U. Møller, D. G. Cooke, K. Tanaka, and P. U. Jepsen, “Terahertz reflection spectroscopy of Debye relaxation in polar liquids,” *J. Opt. Soc. Am. B*, **19**, A113 (2009).
- [Nag06] M. Nagai, H. Yada, T. Arikawa, and K. Tanaka, “Terahertz time-domain attenuated total reflection spectroscopy in water and biological solution,” *Int. J. IRMMW.*, **27**, 505 (2006)
- [Nah96] A. Nahata, D. H. Auston, C. Wu, and T. F. Heinz, “Coherent detection of freely propagating terahertz radiation by electro-optic sampling”, *Appl. Phys. Lett.*, **68**, 150 (1996).
- [Nak04] M. Nakajima, Y. Oda, and T. Suemoto, “Competing terahertz radiation mechanisms in semi-insulating InP at high-density excitation,” *Appl. Phys. Lett.*, **85**(14), 2694 (2004).
- [Neu86] M. Neumann, “Dielectric relaxation in water. Computer simulations with the TIP4P potential,” *J. Chem. Phys.* **85**, 1567 (1986).
- [Nie00] H. Nienhuys, R. A. v. Santen, and H. J. Bakker, “Orientational relaxation of liquid water molecules as an activated process ,” *J. Chem. Phys.*, **112**, 8487 (2000).
- [Och07] R. Ochrombel, *Temperaturabhängige optische, elektrooptische und piezoelektrische untersuchungen ausgewählter azentrischer kristalle* doctoral thesis, Cologne University (2007).
- [Oka84] Y. Okada and Y. Tokumaru, “Precise determination of lattice parameter and thermal expansion coefficient of silicon between 300 and 1500 K,” *J. Appl. Phys.*, **56**, 314 (1984).
- [Pal77] E. D. Palik, “History of far-infrared research. I. The Rubens era,” *J. Opt. Soc. Am.* Vol., **67**(7), 857 (1977).
- [Pet02] R. H. Petrucci, W. S. Harwood, and F. G. Herring, *General chemistry, principles and modern applications*, Prentice-Hall, 8th edn, 441(2002).
- [Qia12] W. Qiao, K. Yang, A. Thoma, and T. Dekorsy, “Dielectric relaxation of HCl and NaCl solutions investigated by Terahertz time-domain spectroscopy, ” *J. Infrared. Milli. Terahz. Waves.*, **33** , 1029 (2012)

- [Que09]. C. T. Que, T. Edamura, M. Nakajima, M. Tani, and M. Hangyo, "Terahertz Radiation from InAs Films on Silicon Substrates Excited by Femtosecond Laser Pulses," *Jpn. J. Appl. Phys.*, **48**(1), 010211 (2009).
- [Røn97] C. Rønne, L. Thrane, P. Åstrand, A. Wallqvist, K. V. Mikkelsen, and S. R. Keiding, "Investigation of the temperature dependence of dielectric relaxation in liquid water by THz reflection spectroscopy and molecular dynamics simulation," *J. Chem. Phys.*, **107**, 5319 (1997).
- [Røn99] C. Rønne, P. Åstrand, and S. R. Keiding, "THz-Spectroscopy of H₂O(l) and D₂O(l)," *Phys. Rev. Letters.*, **82**, 2888 (1999).
- [Røn00] C. Rønne, *Intermolecular liquid dynamics studied by THz-spectroscopy*, doctoral thesis, AARHUS University Denmark (2000).
- [Røn02] C. Rønne and S. R. Keiding, "Low frequency spectroscopy of liquid water using THz-time domain spectroscopy," *J. Mol. Liq.*, **101**, 199 (2002).
- [Sch01] M. Schall, M. Walther, and P. U. Jepsen, "Fundamental and second-order phonon processes in CdTe and ZnTe," *Phys. Rev. B.*, **64**, 094301 (2001).
- [Sch09] D. A. Schmidt, Ö. Birer, S. Funkner, and M. Havenith. "Rattling in the cage: ions as probes of sub-picosecond water network dynamics," *J. Am. Chem. Soc.*, **131**, 18512 (2009).
- [Sli66] T. R. Sliker and J. M. Jost, "Linear electro-optic effect and refractive indices of cubic ZnTe," *Phys. Rev.*, **56**, 130 (1966).
- [Spe91] D. E. Spence, P. N. Kean, and W. Sibbett, "60-fsec pulse generation from a self-mode-locked Ti:sapphire laser," *Opt. Lett.*, **16** (1), 42 (1991).
- [Sta99] F. W. Starr, J. K. Nielsen, and H. E. Stanley, "Fast and slow dynamics of hydrogen bonds in liquid water," *Phys. Rev. Lett.*, **82**, 2294 (1999).
- [Sut99] D. H. Sutter, G. Steinmeyer, L. Gallmann, N. Matuschek, F. Morier-Genoud, U. Keller, V. Scheuer, G. Angelow, and T. Tschudi "Semiconductor saturable-absorber mirror assisted Kerr-lens mode-locked Ti:sapphire laser producing pulses in the two-cycle regime," *Opt. Lett.*, **24** (9), 631 (1999).

- [Swa07] J. M. J. Swanson, C. M. Maupin, H. N. Chen, M. K. Petersen, J. C. Xu, Y. J. Wu, and G. A. Voth, "Proton solvation and transport in aqueous and biomolecular systems: insights from computer simulations," *J. Phys. Chem. B*, **111**, 4300 (2007).
- [Tan97] M. Tani, S. Matsuura, K. Sakai, and S. Nakashima, "Emission characteristics of photoconductive antennas based on low-temperature-grown GaAs and semi-insulating GaAs," *Appl. Opt.*, **36**, 30, 7853 (1997).
- [Tho10] A. Thoma, "Apertureless Scanning Terahertz Near Field Microscopy," doctoral thesis, Konstanz University Germany (2010).
- [Tie09] K. J. Tielrooij, R. L. A. Timmer, H. J. Bakker, and M. Bonn, "Structure dynamics of the proton in liquid water probed with terahertz time-domain spectroscopy," *Phys. Rev. Lett.*, **102**, 198303 (2009).
- [Tie10a] K. J. Tielrooij, N. Garcia-Araez, M. Bonn, and H. J. Bakker, "Cooperativity in ion hydration," *Science*, **328**, 1006 (2010).
- [Tie10b] K. J. Tielrooij, *Molecular motions of water, the effect of charged and hydrophobic solutes*, doctoral thesis, FOM-Institute for Atomic and Molecular physics (AMOLF) in Amsterdam Netherlands, (2010).
- [Tri75] R. Triolo and A. H. Narten, "Diffraction pattern and structure of aqueous hydrochloric acid solutions at 20°C," *J. Chem. Phys.*, **63**, 3624 (1975).
- [Urb05] A. Urbanowicz, R. Adomavicius, and A. Krotkus, "Terahertz emission from photoexcited surfaces of Ge crystals," *Physica B*, **367**(1-4), 152 (2005).
- [Val05] N. C. J. van der Valk, P. C. M. Planken, A. N. Buijserd, and H. J. Bakker, "Influence of pump wavelength and crystal length on the phase matching of optical rectification," *J. Opt. Soc. Am. B.*, **22**, 1714 (2005).
- [Wan04] K. Wang and D. M. Mittleman, "Metal wires for terahertz wave guiding," *Nature*, **432**, 376 (2004).
- [Win97] C. Winnewisser, P. U. Jepsen, M. Schall, V. Schyja, and H. Helm, "Electrooptic detection of THz radiation in LiTaO₃, LiNbO₃ and ZnTe," *Appl. Phys. Lett.*, **70**, 3069 (1997).

- [Wu95] Q. Wu and X. C. Zhang, "Free-space electro-optic sampling of terahertz beams," *Appl. Phys. Lett.*, **67**, 3523 (1995)
- [Wu96] Q. Wu and X. C. Zhang, "Design and characterization of traveling-wave electrooptic terahertz sensors," *IEEE J. Select. Top. Quantum. Electron.*, **2**, 693 (1996).
- [Yad08] H. Yada, M. Nagai, and K. Tanaka, "Origin of the fast relaxation component of water and heavy water revealed by terahertz time-domain attenuated total reflection spectroscopy," *Chem. Phys. Lett.*, **464**, 166 (2008).
- [Yad09] H. Yada, M. Nagai, and K. Tanaka, "The intermolecular stretching vibration mode in water isotopes investigated with broadband terahertz time-domain spectroscopy," *Chem. Phys Lett.*, **473**, 279 (2009).
- [Yan73] K. H. Yang, J. R. Morris, P. L. Richards, et al. "Phase-matched far-infrared generation by optical mixing of dye laser beams," *Appl. Phys. Lett.*, **23**(12), 669 (1973).
- [Yu01] Y. M. Yu, S. Nam, K. S. Lee, Y. D. Choi, and B. O, "Photoluminescence characteristics of ZnTe epilayers," *J. Appl. Phys.*, **90**, 807 (2001).
- [Zha04] J. Zhang and D. Grischkowsky, "Waveguide THz time-domain spectroscopy of nm water layers," *Opt. Lett.*, **29**, 1617 (2004).

List of publications

Parts of this thesis have been published in journal articles or presented at a conference.

Publications in refereed journals:

W. Qiao, D. Stephan, M. Hasselbeck, Q. Liang, and T. Dekorsy, *Low-temperature THz time domain waveguide spectrometer with butt-coupled emitter and detector crystal*, Opt. Express. **20** (18), 19769–19777 (2012).

W. Qiao, K. Yang, A. Thoma, and T. Dekorsy, *Dielectric relaxation of HCl and NaCl solutions investigated by Terahertz time-domain spectroscopy*. Journal of Infrared, Millimeter and Terahertz Waves, **33**(10), 1029-1038 (2012).

G. Klatt, F. Hilser, W. Qiao, M. Beck, R. Gebbs, A. Bartels, K. Huska, U. Lemmer, G. Bastian, M.B. Johnston, M. Fischer, J. Faist, and T. Dekorsy, *Terahertz emission from lateral photo-Dember currents*. Opt. Express. **18** (5), 4939--4947 (2010).

Conference contributions:

W. Qiao, D. Stephan, M. Hasselbeck, Q. Liang, and T. Dekorsy, *A compact, low-temperature THz time domain waveguide spectrometer*, 2012 3rd EOS Topical Meeting on Terahertz Science & Technology (TST 2012), Kaiserstejnsky Palace, Prague, Czech Republic, 17 June 2012 - 20 June 2012 Poster, (2012).

W. Qiao, A. Thoma and T. Dekorsy, *Temperature Controllable Terahertz Time-Domain Reflection Spectroscopy of Aqueous Systems*, 2011 Conference on Lasers and Electro-Optics Europe & 12th European Quantum Electronics Conference, Munich (Germany), 22-26 May 2011. CLEO/Europe-EQEC Conference Poster, (2011).

W. Qiao, A. Thoma and T. Dekorsy, *Terahertz Time-Domain Spectroscopy of Aqueous Systems in Reflection Geometry*, 2010 THz Radiation: Generation, Detection and Applications, Bad Honnef (Germany), 18-21 April 2010. Poster, (2010).

G. Klatt, F. Hilser, W. Qiao, M. Beck, R. Gebbs, A. Bartels, K. Huska, U. Lemmer, G. Bastian, M.B. Johnston, M. Fischer, J. Faist and T. Dekorsy, *Terahertz Radiation from Multiplexed Photo-Dember Currents*, International Conference on Ultrafast Phenomena (UP), Snowmass Village, CO, July 18, (2010).

A. Thoma, M. Beck, W. Qiao, G. Klatt, R. Gebbs, A. Bartls, M. Nagel, and T. Dekorsy, *2-dimensional Mapping of Frequency Response of a Single THz Split-Ring Resonator Probed by High Speed Asynchronous Optical Sampling*, 2009 Conference on Lasers and Electro-Optics Europe & the European Quantum Electronics Conference, Munich (Germany), 14-19 June 2009. CLEO/Europe-EQEC Conference Digest (2009).

Acknowledgments

These four years of study at the University of Konstanz will be a great treasure for my whole life. Besides enriching my knowledge of physics, I have learned a lot in many aspects, the rigorous academic attitude, and the efficient academic performance; moreover, I have received a lot of encouragement and friendship from people around me which will benefit me for the rest of my life.

First of all, I would like to express my sincere appreciation to my advisor, Prof. Dr. Thomas Dekorsy, for his advice, support, and guidance throughout the whole duration of my doctoral research. His encouragement and help made the completion of this work possible. I admire him for his meticulous and rigorous scholarship, which will stimulate me on my further way to scientific research.

In particular I would like to thank Arne Thoma for his guidance to THz in my early doctoral research. I appreciate his help on my first TDS setup and many useful discussions. I would also like to thank Dr. Kejian Yang for his encouragement and helpful advice during my whole doctoral study. I would also like to thank Daniel R. Stephan for his previous work on the waveguide setup. I would also like to thank Qijun Liang , Xianbin Zhang and Daniel Skorka for carefully spellchecking my work.

I would also like to show my gratitude to Prof. Dr. Jure Demsar for valuable advice and suggestions as member of my dissertation committee.

My colleagues from the A.G. Dekorsy supported me in my work. I would like to thank them for all their help, support, and valuable hints. They are Raphael Gebbs, Gregor Klatt, Florian Hilser, Matthias Beck, Hanjo Schaefer, Helena Barros, Mike Hasselbeck, Johanna Flock, Martin Schubert, Oliver Ristow, Mike Hettich, Dirk Heinecke, Marcel Indlekofer, Chuan He, Robert Fleischhaker and Axel Bruchhausen. The good cooperation between them

and me made this a pleasant working environment and the extracurricular arrangements made our lives colourful.

I would also like to thank Ute Henzen for her help with the official questions and for the organization of drinks, thank Stefan Eggert and Christian Beschle for a lot of technical support, and Matthias Hagner for the help with sample preparations in the Nanolab.

Especially, I would like to thank my grandparents, my parents, my brother and sister for their love and encouragement, without which I wouldn't have been able to make it this far.